DECEMBER 2025 Ph.D. in Electrical and Electronics Engineering THURA ALI KHALAF

REPUBLIC OF TÜRKİYE

GAZİANTEP UNIVERSITY

GRADUATE SCHOOL OF NATURAL & APPLIED SCIENCES

ADVANCED ANTENNA SOLUTIONS FOR MILIMETER WAVE 5G APPLICATIONS

Ph.D. THESIS

IN

ELECTRICAL AND ELECTRONICS ENGINEERING

BY

THURA ALI KHALAF AL-MOHAMMEDAWI

DECEMBER 2025

ADVANCED ANTENNA SOLUTIONS FOR MILIMETER WAVE 5G APPLICATIONS

Ph.D. Thesis

in

Electrical and Electronics Engineering

Gaziantep University

Supervisor

Prof. Dr. Gölge ÖGÜCÜ YETKİN

by

Thura Ali Khalaf AL-MOHAMMEDAWI

December 2025

I hereby declare that all information in this document has been obtained and presented in accordance with academic rules and ethical conduct. I also declare that, as required by these rules and conduct, I have fully cited and referenced all material and results that are not original to this work.

Thura Ali Khalaf AL-MOHAMMEDAWI

ABSTRACT

ADVANCED ANTENNA SOLUTIONS FOR MILIMETER WAVE 5G APPLICATIONS

AL-MOHAMMEDAWI, Thura Ali Khalaf
Ph.D. in Electrical and Electronics Eng.
Supervisor: Prof. Dr. Gölge ÖGÜCÜ YETKİN
December 2025
93 pages

This thesis presents the design and simulation of phased array antennas operating at 28 GHz for 5G wireless communication using CST Microwave Studio. The goal is to achieve high-gain, directional arrays with wide beam-steering and stable performance. Two single-element antennas, a slotted patch and a parasitic patch, were first designed and analyzed. Both showed good radiation characteristics, with the slotted element achieving a slightly higher gain of 8.4 dBi. These were then configured into two phased arrays: a 1×10 slotted array and a 1×8 parasitic array. The parasitic array achieved a wider steering range of −58° to +58°, a peak gain of 15.2 dBi, and a side-lobe level (SLL) of −14.9 dB, while the slotted array attained a higher gain of 18.5 dBi, SLL of −13.4 dB, and a steering range of −44° to +44°. The slotted array also maintained a more stable gain between 18.5 and 14.8 dBi, meeting the 5G requirement of at least 12 dBi, whereas the parasitic array's gain dropped to 9.6 dBi at some angles. Therefore, the slotted array was optimized using ten tapering techniques, with the exponential taper effectively reducing side lobes to −21.7 dB while maintaining about 18 dBi gain. A prototype was fabricated and measured, showing satisfactory agreement with simulation results despite minor fabrication variations. The CST results were further validated with HFSS, confirming consistency between both simulation platforms.

Keywords: 5G, Millimeter-wave, 28-GHz, Microstrip patch, Phased array antenna

ÖZET

MILIMETRE DALGA 5G UYGULAMALARI IÇIN GELIŞMIŞ ANTEN ÇÖZÜMLERI

AL-MOHAMMEDAWI, Thura Ali Khalaf
Doktora Tezi, Elektrik-Elektronik Müh. Bölümü
Tez Yöneticisi: Dr. Gölge ÖGÜCÜ YETKİN
Aralık 2025
93 sayfa

Bu tez, 28 GHz'de çalışan 5G kablosuz haberleşme için faz dizili antenlerin tasarımını ve benzetimini CST Microwave Studio kullanarak sunmaktadır. Çalışmada, yüksek kazançlı, yönlü, geniş huzme yönlendirme yeteneğine sahip ve kararlı performans gösteren diziler hedeflenmiştir. İlk olarak yarıklı yama ve parazitik yama olmak üzere iki tek-elemanlı anten tasarlanmış ve analiz edilmiştir; her iki anten de iyi ışıma karakteristiği sergilemiş, yarıklı anten 8,4 dBi ile biraz daha yüksek kazanç sağlamıştır. Bu elemanlar daha sonra 1×10 yarıklı dizi ve 1×8 parazitik dizi olmak üzere iki faz dizisine dönüştürülmüştür. Parazitik dizi −58° ila +58° arasında daha geniş yönlendirme aralığı, 15,2 dBi tepe kazanç ve −14,9 dB yan lop seviyesi (SLL) elde ederken; yarıklı dizi 18,5 dBi ile daha yüksek kazanç, −13,4 dB SLL ve −44° ila +44° yönlendirme aralığına ulaşmıştır. Ayrıca yarıklı dizi 18,5 ile 14,8 dBi arasında daha kararlı kazanç sergileyerek en az 12 dBi gereksinimi olan 5G şartlarını sağlarken, parazitik dizinin kazancı bazı açılarda 9,6 dBi'ye düşmüştür. Bu nedenle yarıklı dizi on farklı daraltma tekniği kullanılarak optimize edilmiş ve üstel daraltma yöntemi yaklaşık 18 dBi kazancı korurken yan lopları −21,7 dB'e düşürmüştür. Üretilen prototipin ölçüm sonuçları, küçük üretim farklılıklarına rağmen simülasyon sonuçlarıyla uyum göstermiş; ayrıca CST sonuçları HFSS ile doğrulanarak her iki platform arasında tutarlılık sağlanmıştır.

Anahtar Kelimeler: 5G, Milimetre dalga, 28 GHz, Mikroşerit yama, Faz dizili anten

'' This thesis is dedicated to my mother, whose unwavering love, sacrifices, and encouragement have guided me through every step of my journey. I owe everything I have achieved to you (Hayfaa Alanssari)''

ACKNOWLEDGEMENTS

I would like to thank my supervisor, Prof. Dr. Gölge Ögücü Yetkin, for her invaluable guidance and support throughout this study. I am sincerely grateful for her continuous encouragement and motivation.

I would also like to thank Prof. Dr. Muharrem Karaaslan for his valuable assistance during the experimental part of this research, conducted in the laboratory of İskenderun Technical University.

Additionally, I would like to express my deepest love and gratitude to my mother for her unwavering support and heartfelt best wishes. I am also grateful to my sisters for their constant support and encouragement.

TABLE OF CONTENTS

LIST OF TABLES

Page

LIST OF FIGURES

Page

LIST OF SYMBOLS

GHz	Gigahertz
MHz	Megahertz
dBi	decibel relative to isotropic
dB	decibel
mm	millimetre
W	Width of the patch
L	Length of the patch
c	speed of light
$\mathbf{f_r}$	resonant frequency
ε_r	dielectric constant
ε_{reff}	effective dielectric constant
ΔL	extension length
h	height of the substrate
$\mathbf{W_g}$	Width of the ground
$\mathbf{L_g}$	Length of the ground
λ	wavelength
N	Number of the antenna elements
d	distance
k	wave number
$\Delta\varphi$	phase difference
U	radiation intensity
$\mathbf{P_{rad}}$	radiated power
η_{rad}	radiation efficiency
Γ	reflection magnitude
$\mathbf{W_f}$	width of the feedline

LIST OFABBREVIATIONS

mmWave	Millimeter-wave
PCB	Printed Circuit Board
SLL	Side lobe level
FCC	Federal Communications Commission
CST	Computer Simulation Technology
HFSS	High-Frequency Structure Simulator
5G	Fifth Generation
VSWR	Voltage Standing Wave Ratio
D	Directivity
G	Gain
RG	Realized Gain
AF	Array Factor
FR-4	Flame Retardant
tan δ	tangent loss
FDTD	Finite-Difference Time-Domain
FEM	Finite Element Method

CHAPTER 1
OVERVIEW AND PREVIOUS STUDIES

1.1 Introduction

The evolution of wireless communication technologies is accelerating the need for better data throughput, lower delays, and more efficient spectrum utilization, prompting a shift toward higher frequency bands. Millimeter-wave (mmWave) bands have emerged as a prominent solution to these requirements. However, these mmWave signals typically suffer from high path loss, limited penetration through physical obstructions, and susceptibility to signal blockage from environmental factors. These challenges necessitate the development of advanced antenna systems capable of producing highly directional radiation patterns with elevated gain to ensure robust communication links.

Among the various mmWave bands, the 28 GHz band has gained attention as a preferred candidate for short-range wireless deployments due to its relatively lower susceptibility to rain attenuation and favorable propagation characteristics in dense urban environments. The 28 GHz spectrum enables high data transmission due to its wide bandwidth, making it suitable for large-capacity and fast communication links [1-3].

To address the propagation challenges associated with mmWave frequencies, antenna systems with high-gain and beam-steering capabilities are crucial. High gain enhances signal strength to offset significant path loss, while beam steering enables dynamic directionality, ensuring stable communication in both fixed and mobile environments. However, achieving these features is challenging with single-element antennas. Although such antennas offer benefits like simplicity and compactness, their limited gain and lack of directional control render them ineffective for mmWave applications. Consequently, antenna arrays composed of multiple radiating elements arranged in linear, planar, or conformal configurations are employed to improve gain and facilitate electronic beam steering.

Antenna arrays are central to this approach. By arranging multiple radiating elements in strategic geometries, array antennas can achieve narrow beams and improve directivity, which enhances both link quality and spatial coverage. Beam steering in these arrays is typically achieved using phase shifters that introduce controlled delays between elements, allowing real-time adjustment of the beam's direction. This capability is especially critical in dynamic environments, where user movement and obstructions frequently change signal paths. Phased array antennas provide an effective solution, and in recent decades, they have seen significant advancements and widespread application across numerous fields [4–6].

In conclusion, the development of high-gain, beam-steerable antenna arrays operating at 28 GHz is essential to overcoming the limitations of mmWave propagation. These antennas are fundamental building blocks in next-generation wireless networks, offering directional radiation, high efficiency, and dynamic control. This research contributes to the continuous development of efficient millimeter-wave antenna systems by addressing key performance metrics such as gain and scanning range. The outcomes are intended to support the realization of robust and scalable antenna solutions for 5G millimeter wave applications.

1.2 Literature Survey

With ongoing research and technological advancements, antenna array designs continue to evolve to address the challenges associated with mmWave operation, while providing high gain and wide coverage. Numerous antenna array configurations operating at 28 GHz have been proposed and investigated in preparation for 5G systems:

In 2018, Junho Park, et al. [7] introduced a new millimeter-wave hybrid antenna system consisting of a 1 × 4 endfire in package array antenna and a 1 × 16 patch array antenna installed on the display area of the mobile device to steer the antenna beam in the end-fire and broadside directions. At 28 GHz, the far-field results showed that the peak gains of the broadside 16-element array and the end-fire 4-element array are 12.8 dBi and 9.2 dBi. The 4-element phased array achieved scanning coverage at ± 49°.

In 2018, Manoj Stanley, et al. [8] presented a capacitive-coupled patch array antenna. The array elements were organized on the edges of mobile PCB as a group of four sub arrays each consisted of 12 antenna elements. The peak gain for each sub array is 16.5 dBi with 90°coverage in the theta plane. Each sub array offered a beam steering at ± 60° in the phi plane. The results also showed that the array can cover the frequency range from 24 GHz to 28 GHz.

In 2019, Hojoo Lee, et al. [9] proposed a 1 × 8 phased antenna array resonating at 28 GHz. The array consisted of dipole antenna radiators placed on a ground area suited for mobile devices with air-gap slots between a pair of adjoining components. The array antenna achieved a maximum gain of 10.33 dBi, a SLL of 13 dB and a 10-dB bandwidth of 2 GHz. The antenna array obtained a scanning coverage of ± 45°.

In 2020, Sungpeel Kim and Jaehoon Choi [10] introduced a slotted quasi-Yagi antenna array consisting of eight elements arranged in a single row operating at 28 GHz. This antenna array demonstrated a highest gain at 11.16 dBi with ± 48° beam steering coverage. The simulated showed a 10-dB bandwidth of 1.79 GHz and the interelement mutual coupling was less than -25.02 dB at (27.5–28.35 GHz) band.

In 2020, Mustapha El Halaoui, et al. [11] proposed a dual band array of 32 elements for 5G applications. Each element was shaped as flipped-F antenna. The array operated across both the 28 GHz and 38 GHz frequency bands with interelement mutual coupling less than -35 dB. The array achieved gains of 16.52 dB and 15.35 dB at 28.38 GHz and 38.49 GHz, respectively, and supported beam steering over a range of ±45°.

In 2021, Naser Ojaroudi Parchin, et al. [12] proposed a linear phased array antenna consisting of eight T-shaped slots and solo directors placed on the edge of mobile PCB. The proposed array exhibited a peak gain of 12.5 dB, a reflection coefficient bandwidth more than 1 GHz, and interelement mutual coupling of -15 dB at 28 GHz. This array was capable of steering the main beam from 0° to 70°.

In 2022, Naser Ojaroudiparchin, et al. [13] introduced a phased array antenna consisting of 10 slotted-loop elements which are placed on the edge of handset PCB. The array achieved peak gain of more than 13 dB with scanning coverage of ± 70°.

The simulated performance demonstrated that the antenna supports the 27–29 GHz range with a reflection coefficient below –10 dB.

In 2023, Ahmed S.I. Amar, et al. [14] presented a linear array of 8 dipoles printed on the top of the mobile substrate. This array demonstrated a wide operation band from 25 to 36 GHz with mutual coupling of -16 dB over that frequency band. The simulation results exhibited a peak gain of 12.5 dBi with scanning coverage of 80°.

In 2024, Kakumanu Naga Raju and Arunachalam Kavitha [15] proposed a 1×6 linear phased-array antenna operating at 28 GHz, utilizing metamaterial-integrated patch elements. The array demonstrates isolation levels below −16.25 dB between adjacent elements. A maximum gain of 12.55 dBi and an efficiency exceeding 79% were achieved across the operational band. Furthermore, the array can scan its main lobe up to ±43.5° by adjusting the phase excitation among the antenna elements.

1.3 Problem Statement

To address the mmWave issues, phased array antennas have become a promising solution due to their capability to electronically steer beams, improve signal directionality, and enhance overall system gain. Nonetheless, designing phased array antennas introduces a new set of difficulties. These include managing the spacing between antenna elements to avoid side lobes, minimizing mutual coupling effects, achieving precise beam steering, and ensuring functionality at high frequencies with minimal losses.

This research seeks to solve the problem of how to effectively design phased array antennas that operate at 28 GHz and meet the performance requirements for 5G mm-wave systems. The focus is on creating an antenna structures that are not only compact and high-gain but also capable of wide-angle beam steering and suitable for integration into modern mobile communication applications.

1.4 Research Aims

This research primarily aims to design and develop a high-efficiency phased array antenna operating at 28 GHz, specifically suited for 5G millimeter-wave applications. To achieve this goal, the following specific objectives are outlined:

1. To design and analyze single antenna elements with optimal radiation performance at 28 GHz.
2. To design compact and efficient antennas array by arranging multiple antenna elements, ensuring suitable element spacing, high gain, low side lobes and minimal mutual coupling between elements.
3. To implement beam steering capabilities through phase shifting technique, enabling directional radiation for enhanced signal coverage and reduced interference.
4. To minimize side lobe levels by applying amplitude tapering techniques across the array elements, improving radiation pattern quality.
5. To evaluate and optimize the antenna array's performance using simulation tool, analyzing parameters such as return loss, bandwidth, radiation pattern, gain, side lobe levels, and beam scanning range.
6. To compare the proposed design performance through simulation results with existing state-of-the-art phased array antennas for 28 GHz applications.
7. To verify the simulation results of the proposed designs using simulation tools such as CST and HFSS.

1.5 Scope of the Project

This project focuses on the design, simulation, and performance evaluation of a phased array antennas resonating at 28 GHz, one of the main frequency bands supporting 5G mm-wave communication. The scope encompasses the design and implementation of high-gain, beam-focused antenna systems that can support electronic beam steering to ensure reliable connectivity and wide angular coverage in complex and dynamic environments.

The work begins with the design and optimization of single patch antenna elements that meet the required performance criteria at 28 GHz, such as return loss, bandwidth, gain, and radiation pattern. Once the single elements are validated, linear arrays are constructed using multiple elements, with careful attention to element spacing, array configuration, side lobe levels, and mutual coupling effects. To minimize sidelobe levels, amplitude tapering techniques will be applied to the proposed phased array antennas.

The proposed arrays are designed using electromagnetic design software such as CST Microwave Studio. To ensure the accuracy and reliability of the simulated antenna performance, the results obtained from CST Microwave Studio were cross-verified using ANSYS HFSS, allowing for a comparative analysis between the two electromagnetic solvers. Among the simulated designs, the one demonstrating the most favorable performance was selected for fabrication. The selected antenna prototype was fabricated and subsequently tested to evaluate its return loss and confirm that it operates at the intended frequency, ensuring consistency with the simulated performance.

1.6 Methodology

The methodology adopted in this thesis involves a structured approach to the design, simulation, evaluation, and validation of antenna arrays optimized for 28 GHz millimeter-wave (mmWave) 5G applications. The following key phases were followed throughout the project:

1. Literature review and requirement analysis

   A comprehensive literature review was conducted to understand current trends, design challenges, and performance requirements associated with mmWave antennas, particularly at 28 GHz. Key parameters such as gain, steering range, and coverage were identified as primary performance indicators. This phase also helped define the design objectives and establish the selection criteria for antenna configurations

2. Specification Definition

   This stage involves establishing the performance requirements based on 5G mm-wave standards. The target frequency of operation is set at 28 GHz, falling within the FCC-allocated spectrum for 5G services (27.5-28.35) GHz [16].

3. Antenna design and configuration

   Two antenna structures were proposed and modeled, including single-element and multi-element microstrip patch array antennas arranged in linear geometry. The arrays are configured to support electronic phase control across individual elements. Initial design dimensions were calculated based on standard electromagnetic equations suitable for operation at 28 GHz. Substrate materials and design constraints, such as size and dielectric properties were also considered.

4. Simulation

The proposed designs were simulated using two simulation programs: CST and ANSYS HFSS. These platforms were used to analyze key performance metrics, including return loss (S11), gain, beam directionality, side lobe levels, and beam steering capability.

5. Verification of results

To ensure accuracy and consistency, simulation results obtained from CST were cross-verified using HFSS. This comparison helped validate the simulated performance, identify discrepancies, and confirm the reliability of the chosen design under different solvers.

6. Fabrication and testing

The antenna design that exhibited the best performance in simulation was selected for fabrication. The prototype was realized using standard PCB manufacturing techniques, and return loss was measured using a network analyzer to verify the antenna's operation at the target frequency.

1.7 Thesis Outline

Chapter 1 focuses on presenting the foundational concepts relevant to the research. It covers the study's introduction, a review of related literature, the problem statement, research objectives, the scope of the thesis, and the methodology employed. Chapter 2 details the theoretical foundation and design procedures of the single patch and array antennas. Chapter 3 presents the design, simulation, and analysis of single antenna elements using electromagnetic solvers such as CST and HFSS. Performance metrics like return loss, gain, and radiation pattern are analyzed and compared across platforms to validate the results. Chapter 4 includes the design, simulation, and performance evaluation of linear phased-array antennas developed from the optimized single-element configurations. The array's characteristics, such as beam-steering capability, gain, side-lobe levels, and mutual coupling, are analyzed across simulation platforms to validate the array behavior. In addition, this chapter also discusses the experimental testing procedure, focusing on verifying the operating frequency and return loss through practical measurements. Finally, chapter 5 provides a conclusion to the thesis by reviewing the key findings and offering recommendations for future research.

CHAPTER 2
ANTENNA DESIGN THEORY

2.1 Millimeter-Wave Spectrum and 5G Frequency Bands

The millimeter-wave (mmWave) region within the spectrum of electromagnetic waves extends across 30–300 GHz, equivalent to wavelengths in the 10–1 mm range. The integration of mmWave frequency bands into the 5G New Radio (NR) standard, specifically within Frequency Range 2 (FR2), has become a major focus of both academic and industrial efforts. This is due to mmWave's large available bandwidth, which enables ultra-high throughput and low latency, key requirements of next-generation communication systems. While the mmWave band formally begins at 30 GHz, 5G NR specifications extend coverage as low as 24 GHz to take advantage of frequencies that still offer wide bandwidth and low latency performance, as illustrated in Figure 2.1 [17], [18].

Unlike the congested sub-6 GHz bands of Frequency Range 1 (FR1), mmWave frequencies remain relatively underutilized, offering abundant bandwidth to meet the growing demands for high data rates and network capacity. Historically, these bands were considered unsuitable for wireless communication due to their unfavorable propagation characteristics. However, recent technological advancements have significantly mitigated these challenges, making mmWave a viable option for 5G deployment [19], [20].

Although the International Telecommunication Union (ITU) had initially designated sub-6 GHz frequencies for 5G during its 2015 World Radio Communication Conference, it was not until mid-2018 that consensus emerged regarding the mmWave bands suitable for 5G backhaul and access links. These higher frequencies offer not only vast bandwidth but also regulatory advantages, as some mmWave bands are unlicensed or lightly licensed, reducing deployment costs for operators. Although millimeter-wave signals experience greater atmospheric attenuation than sub-6 GHz frequencies, this characteristic allows for denser frequency reuse and helps reduce interference, particularly in urban environments. Standards organizations like the Federal Communications Commission (FCC) and the European Telecommunications Standards Institute (ETSI) have identified several key frequency ranges as potential candidates for 5G mmWave deployment, including frequencies ranging from 24.25 up to 27.5 GHz, 26.5 up to 29.5 GHz, 27.5 up to 28.35 GHz, 37 up to 40 GHz, and 40.5 up to 43.5 GHz [21].

To align with the scope of this thesis, the antenna design is primarily focused on the 28 GHz high-frequency band. This band has emerged as one of the most attractive candidates for next-generation 5G systems due to its unique combination of technical and practical advantages. First and foremost, it offers up to 1.3 GHz of total bandwidth, including a single contiguous channel as wide as 850 MHz. This abundance of underutilized spectrum enables extremely high data rates and the low latency required by modern 5G applications. Compared to higher mmWave bands, the 28 GHz band also exhibits lower propagation and penetration losses, enabling more reliable coverage over short distances in dense urban environments. Furthermore, this frequency benefits from widespread global regulatory harmonization. Early deployments in markets such as the United States, South Korea, Japan, and China have prioritized the 28 GHz band, accelerating the development of compatible antennas and network infrastructure. In addition, the band supports efficient antenna array integration, enabling high-gain, beam-steerable antennas essential for overcoming the significant free-space path loss typical of mmWave communications. These characteristics make the 28 GHz band not just a viable option, but a strategic choice for building high-performance, future-proof 5G networks [22–27].

Central to achieving 5G performance targets is the antenna, a critical component that must now function beyond the limitations of conventional fixed-pattern designs used in earlier generations. To meet these advanced performance demands, the use of antenna arrays is essential, as they offer the capability to form narrow beams, enhance gain, and enable dynamic beam steering. In mmWave 5G systems, antennas must support beam-steering mechanisms to ensure efficient signal targeting and reduced interference. Additionally, maintaining low insertion losses is essential to maximize coverage while minimizing transmit power. The following section explores the antenna design principles and techniques that make such performance achievable in modern 5G systems. This sets the foundation for understanding the antenna array technologies required to leverage mmWave potential in practical 5G applications.

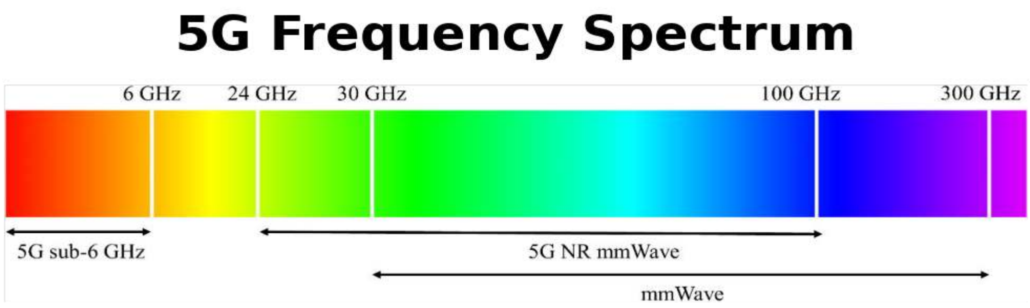

Figure 2.1 5G frequency allocations across the electromagnetic spectrum.

2.2 Patch and Array Antennas: Fundamentals and Design

2.2.1 Microstrip Patch Antenna

A typical microstrip antenna, as shown in Figure 2.2, consists of four main components: a dielectric substrate, a radiating patch, a ground plane, and a feedline. In this structure, the patch is patterned onto the substrate and serves as the primary radiating element. Electromagnetic energy radiates from the edges of the patch, passes through the dielectric material, reflects off the ground plane, and then propagates into free space. Various dielectric materials can be used, with relative permittivity values typically ranging from 2.2 to 12. Conductive materials such as copper are predominantly used for fabricating the patch, regardless of its shape. In practical applications, the patch is most commonly designed in square, circular, or rectangular shapes. Among these, the rectangular configuration is widely used due to its availability and typically offers higher gain than other geometric configurations [28-30].

The performance of a microstrip patch antenna heavily depends on its geometrical parameters, such as patch width, length, and the effective dielectric constant. These dimensions are typically calculated based on the operating frequency, substrate height, and dielectric constant, ensuring that the antenna resonates at the desired frequency [31]. The most widely used formulas for rectangular patch design are derived using transmission line model, which help predict resonant behavior and radiation efficiency. Details of the calculation process are discussed in the following [32],

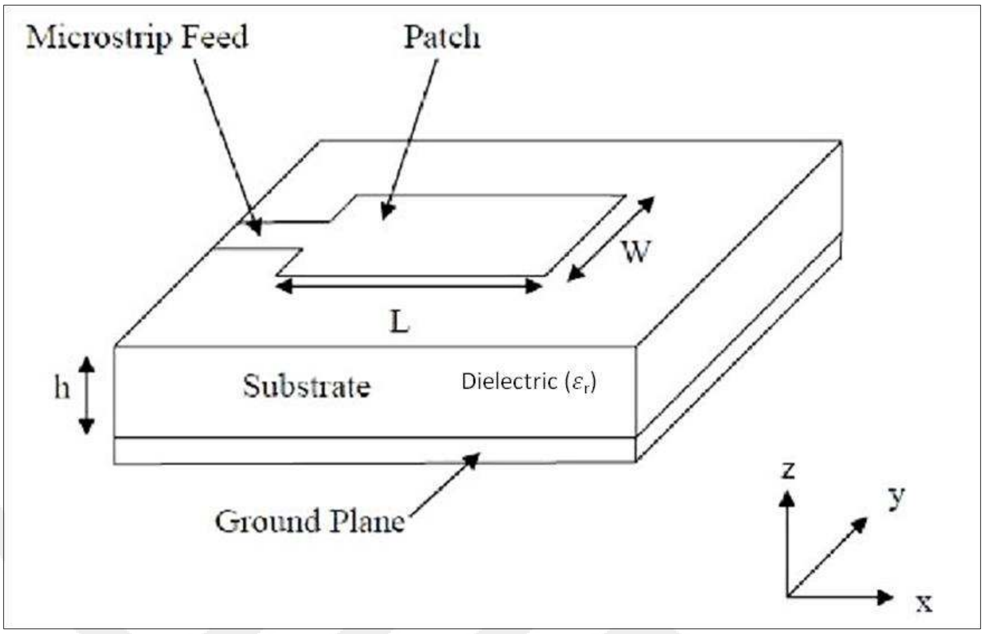

Figure 2.2 Microstrip-fed patch antenna.

The width of the patch can be determined using the following equation,

$$W = \frac{c}{2f_r} \times \sqrt{\left(\frac{2}{\varepsilon_r + 1}\right)} \tag{2.1}$$

Here, c represents the light speed in free space, f_r is the antenna's resonant frequency, and ε_r denotes the substrate's dielectric constant or relative dielectric permittivity.

The patch's length is obtained from the equation below,

$$L = \frac{c}{2f_r\sqrt{\varepsilon_{reff}}} - 2\Delta L \tag{2.2}$$

where, the effective dielectric constant ($\varepsilon_{\mathrm{reff}}$) can be computed using the following expression:

$$\varepsilon_{reff} = \frac{\varepsilon_r + 1}{2} + \frac{\varepsilon_r - 1}{2}\left[1 + \frac{12h}{W}\right]^{-\frac{1}{2}} \tag{2.3}$$

ΔL represents the length extension caused by fringing effects and can be calculated as follows:

$$\Delta L = 0.412h \times \frac{\left(\varepsilon_{reff} + 0.3\right)\left(\frac{W}{h} + 0.264\right)}{\left(\varepsilon_{reff} - 0.258\right)\left(\frac{W}{h} + 0.8\right)} \tag{2.4}$$

here, h signifies the substrate's thickness.

The substrate and ground plane dimensions can be calculated using the following equations [33], [34]:

$$W_g = 6h + W \tag{2.5}$$

$$L_g = 6h + L \tag{2.6}$$

These represent the minimum required dimensions for both the substrate and the ground plane. In most microstrip patch antenna designs, the ground plane is made to match the size of the substrate. This configuration brings multiple benefits. The substrate serves to guide and contain the electromagnetic fields, and a ground plane of equal dimensions ensures that these fields remain confined, promoting efficient radiation. Moreover, matching dimensions help maintain a continuous return path for the currents within the patch, which enhances the antenna's operational effectiveness.

The thickness (or height) of the substrate can be approximated using the following formula [35]:

$$h \geq 0.06\left(\frac{\lambda_{air}}{\sqrt{\varepsilon_r}}\right) \tag{2.7}$$

In contrast to other antenna design parameters that can be independently selected, the substrate thickness is typically constrained by the manufacturer's available stock. Designers must choose from standardized thicknesses provided by the fabrication facility rather than specifying custom values. The selection is influenced by factors such as the complexity of the printed circuit board (PCB), the mechanical strength required, and the desired electrical performance. Thinner substrates are often preferred in applications where space and weight are critical, such as in handheld or portable devices. However, a thicker substrate can enhance surface wave excitation and undesired feed radiation, potentially reducing the antenna's bandwidth and overall performance.

Once the patch and substrate dimensions are determined, careful design of the feedline becomes essential to ensure efficient power transfer and minimal reflection losses. The feedline is responsible for exciting the antenna, either through direct electrical contact or indirect electromagnetic coupling. Microstrip patch antenna feeding methods are typically divided into two primary types: contacting and non-contacting techniques. In contact-based feeding, RF power is supplied directly to the patch via physical connections, including microstrip line, coaxial, inset, or notch feeds. Of these methods, microstrip line feeding is particularly popular because of its straightforward design and easy integration into planar circuits. In contrast, non-contacting methods such as gap and proximity coupling achieve power transfer through electromagnetic field coupling without a physical electrical connection joining the patch and the feedline. The selected feeding method significantly influences the comprehensive performance of the antenna, including bandwidth, return loss, and radiation efficiency. Therefore, selecting an appropriate feed method depends on the specific application requirements and desired performance characteristics [36].

Beyond geometric considerations, microstrip patch antennas offer several advantages over other microwave antenna types, making them a key technology in modern wireless communication systems. Their compact size, lightweight structure, affordability, and ease of fabrication make them ideal for space-constrained or portable devices. These antennas are also compatible with conformal mounting and are easily integrated with printed circuit boards. Although a single patch may have limited gain and bandwidth, these limitations can be effectively addressed by arranging multiple elements in an array. Microstrip patch arrays also allow for design flexibility through various feeding techniques and geometrical configurations, enabling tailored radiation patterns and performance for specific applications [37].

2.2.2 Antenna Arrays and Beam Steering Technique

An antenna array is composed of several radiating elements organized in a particular geometric layout to achieve a targeted directional radiation pattern. A single antenna element typically offers limited directivity and low gain. While these properties can be improved by physically enlarging the element, resulting in narrower beams and higher gain, such an approach often leads to bulky designs impractical for many applications. Antenna arrays provide an effective alternative by increasing the overall size without enlarging individual elements [32], [38].

To maintain design simplicity and uniformity, identical elements are often used within an array. These elements may take various forms, such as microstrip patches, dipoles, aperture antennas, or horn antennas, depending on the required performance and application. The total radiated field of an array is obtained by vectorially summing the contributions from each element, considering both magnitude and phase. This is commonly calculated under the assumption of negligible mutual coupling, meaning that each element's current distribution is unaffected by the presence of others. In practice, this assumption may not always hold, even when all elements are driven with the same amplitude and phase [32].

The resulting radiation pattern is determined by the constructive and destructive interference of the individual element fields. Constructive interference enhances radiation in the intended direction, while destructive interference suppresses it in undesired directions. This pattern can be controlled by adjusting several parameters: the array geometry (linear, planar, circular, etc.), the element radiation characteristics, the spacing between elements, and the excitation amplitude and phase applied to each element [32], [38].

A linear array, where elements are arranged along a straight line, is one of the simplest and most widely used configurations. It is valued for its ease of design, implementation, and beam steering capability. Linear arrays can be classified as either uniform or non-uniform. In a uniform linear array, the elements are identical, equally spaced, and excited with the same amplitude, but with a progressive phase shift between adjacent elements. This configuration produces narrow beamwidths and high directivity. In contrast, non-uniform linear arrays vary in element spacing and excitation amplitude and phase [32], [39], [40].

A practical and widely adopted implementation of this principle is the Phased Array Antenna (PAA), where multiple radiating elements are arranged in a defined geometry and fed with signals having precisely controlled phase shifts. This control enables electronic beam steering within the desired range, producing constructive interference toward the target direction and destructive interference elsewhere, which allows rapid and precise beam positioning without mechanical movement, a critical advantage for systems with strict space and weight constraints [38], [39].

As shown in Figure 2.3, a basic PAA configuration consists of N equally spaced elements separated by a constant distance *d*. Each element is excited with identical amplitude, while a progressive phase shift is applied between successive elements. The element spacing produces phase difference (via path-length difference) in the emitted wavefront, and for observation in the *x–z* plane (*ϕ=0,* so *cos(ϕ)=1*), it becomes [41]:

$$\Delta\varphi = kd\sin(\theta) \tag{2.8}$$

where θ is the beam steering (or boresight) angle, $k=2\pi/\lambda$ represents the wave number, *d* denotes the spacing between elements, and λ is the operating wavelength.

The Array Factor (AF), which characterizes the directional properties of the array, for elements arranged along the x-axis with uniform amplitude excitation and spacing, can be expressed as [32]:

$$AF(\theta) = \sum_{n=0}^{N-1} e^{jn\psi}, \tag{2.9}$$

where $\psi=\Delta\varphi+\beta$ is the cumulative phase shift between elements, and β indicates the progressive phase applied to the feeds.

Beam steering is achieved by modifying the progressive phase shift between elements. To obtain a maximum in a specific direction θ_0, the phase term ψ is set to zero [39]:

$$kd\sin(\theta_0) + \beta = 0 \tag{2.10}$$

which yields:

$$\beta = -kd\sin(\theta_0) \tag{2.11}$$

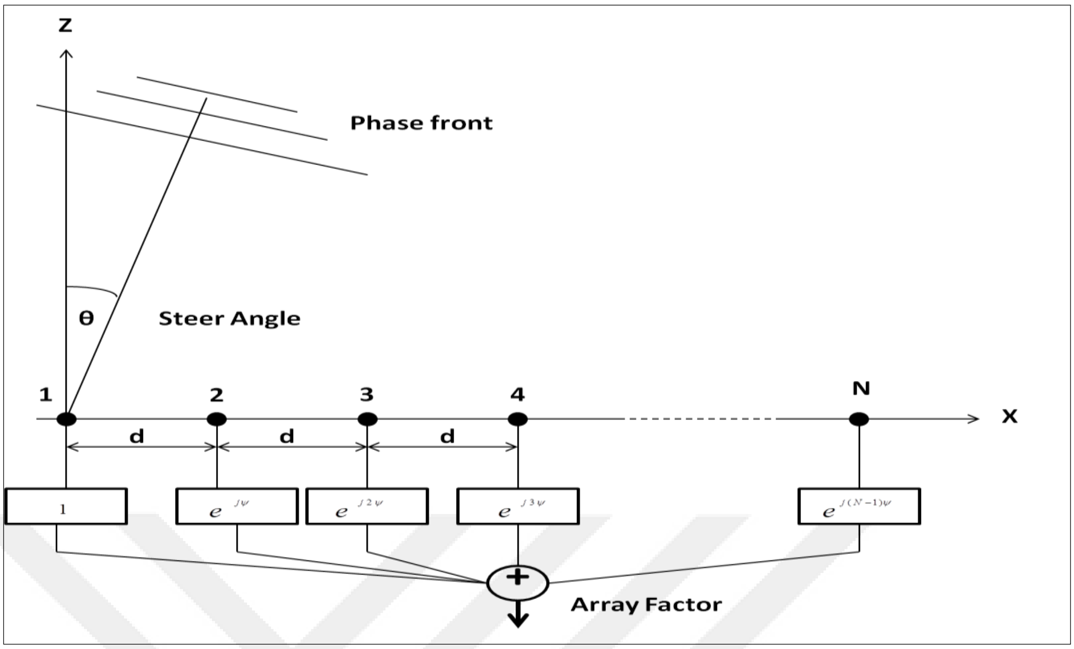

Figure 2.3 Linear phased array configuration.

2.3 Antenna Performance Metrics

This section presents antenna parameters that will be referenced in the thesis, several of which help assess phased array antenna performance. Each is defined briefly below.

2.3.1 Radiation Distribution

An antenna’s radiation pattern depicts how it distributes energy in space, highlighting important features such as directional gain, field level, and radiated energy. Such patterns are usually measured in the far field zone, where the pattern’s shape becomes independent of distance and the magnetic (H) and electric (E) fields maintain orthogonality with each other as well as with the wave’s travel direction. Radiation patterns can be displayed in 2D or 3D formats and are often normalized to their maximum value for clarity. A typical pattern, shown in Figure 2.4, consists of several lobes: the main lobe, representing maximum radiation; minor lobes, which include all other lobes; side lobes, the largest of the minor lobes and generally undesirable; and back lobes, which extend opposite to the main lobe [32].

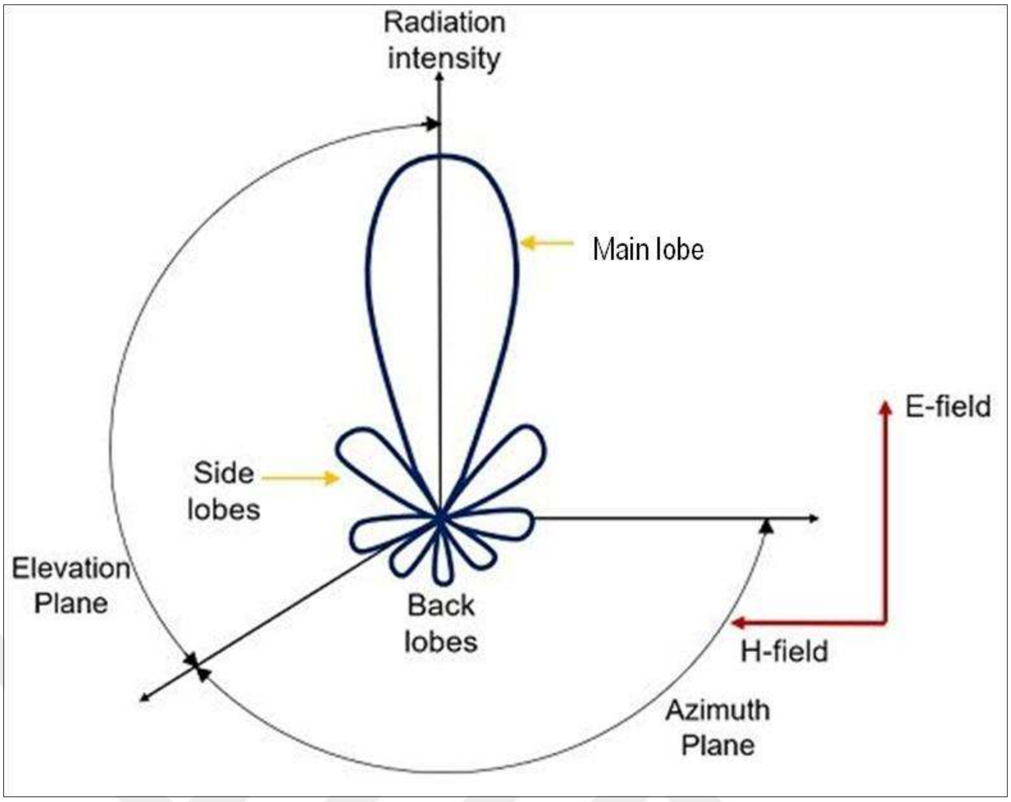

Figure 2.4 Antenna field distribution.

2.3.2 Beamwidth

Beamwidth, a key feature of an antenna's beam pattern, represents the angular width of the main lobe. It is often characterized by the half-power beamwidth (HPBW), indicating the angles where the emitted power decreases to 50% of its maximum (-3 dB), and the first-null beamwidth (FNBW), quantified as the angle subtended between the first null points in the radiation pattern, as depicted in Figure 2.5 [32].

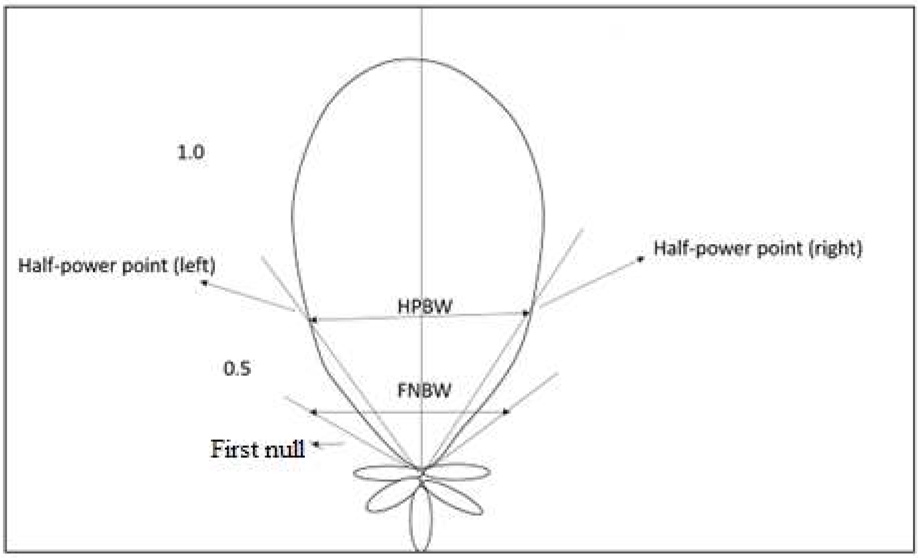

Figure 2.5 Beamwidth of the antenna.

2.3.3 Radiation Directivity of the Antenna

An antenna's directivity measures the extent to which the antenna's radiated power is focused in a specific direction relative to the average power emitted over the entire radiation sphere. It indicates how effectively the antenna concentrates energy into its main lobe. A higher directivity value signifies a stronger and more focused main lobe accompanied by minimal minor lobes, whereas a lower value suggests the opposite. Directivity is a dimensionless quantity and can be mathematically expressed as [32], [42]:

$$D = \frac{U}{U_0} = \frac{4\pi U}{P_{rad}} \tag{2.12}$$

where U denotes the intensity of radiation along a specific direction, U_o represents is the mean radiation intensity, and P_{rad} corresponds to the total power radiated.

2.3.4 Antenna Gain and Realized Gain

The antenna's gain indicates the proportion of power radiated in a specific orientation to that radiated by a reference antenna. It can be referenced to either a dipole antenna or an isotropic antenna, the latter radiating power omnidirectionally. When evaluated against an isotropic radiator, antenna gain is denoted in dBi, whereas comparison with a dipole antenna uses dBd. This parameter characterizes the strength of the transmitted or received signal in a particular direction. It is important to note that gain does not account for losses due to impedance mismatches or reflections. The mathematical expression for antenna gain is given by [32], [42]:

$$G = \frac{4\pi U(\theta,\phi)}{P_{in}} \tag{2.13}$$

where $U(\theta, \phi)$ indicates the intensity of the emitted power in a given orientation, and P_{in} denotes the total incident power.

Unlike antenna gain, realized gain accounts for reflection and impedance mismatch losses. As defined by the IEEE standard, realized gain is obtained by reducing the antenna gain by the mismatch factor, making it a more realistic indicator of the antenna's performance under practical operating conditions [43].

2.3.5 Frequency Bandwidth

This parameter defines the span of frequencies within which the antenna satisfies the required design specifications or standards. By definition, the antenna should maintain acceptable performance within a frequency range centered around its design frequency. The exact range is determined by the antenna's intended application. Bandwidth is typically evaluated using metrics such as voltage standing wave ratio (VSWR) or return loss [32], [43].

2.3.6 Efficiency

Radiation efficiency describes how effectively an antenna transforms the accepted input power into electromagnetic energy radiated into free space. It is described as the proportion of the emitted power (P_{rad}) to the overall power delivered to the antenna (P_{in}), expressed as [32], [44]:

$$\eta_{rad} = \frac{P_{rad}}{P_{in}} \tag{2.14}$$

with $0 \leq \eta_{rad} \leq 1$. This parameter excludes losses from impedance mismatches and instead focuses on resistive and dielectric losses, which cause the radiated power to be less than the power accepted by the antenna.

The total antenna efficiency accounts for both radiation efficiency and mismatch effects, and is expressed as [32], [44]:

$$\eta_{total} = \eta_{ref} \times \eta_{rad} \tag{2.15}$$

where η_{ref} denotes the reflection efficiency and η_{rad} represents the radiation efficiency. Total efficiency therefore incorporates losses from impedance mismatches as well as conduction and dielectric losses at the antenna's input terminals.

2.3.7 Voltage Standing Wave Ratio

This parameter, known as the standing wave ratio or VSWR, indicates how well a transmission line is matched to an antenna by comparing the maximum and minimum voltages in the resulting wave pattern. When an impedance mismatch occurs, part of the transmitted energy is dissipated in the antenna, while the remainder is reflected back toward the source. As the magnitude of the reflection (Γ) increases, so does the ratio between the maximum and minimum voltages. The VSWR value can range from 1 to infinity, with a value of 1 indicating a perfectly matched load. The relationship between VSWR, the reflection coefficient, and voltage ratios is given by [45]:

$$VSWR = \frac{V_{\max}}{V_{\min}} = \frac{1+\Gamma}{1-\Gamma} \tag{2.16}$$

2.3.8 Reflection Loss

Return loss, also referred to as reflection loss, measures the proportion of power reflected by an antenna relative to the power supplied to it**.** It is commonly represented in decibels (dB) using a logarithmic scale. A low return loss indicates poor antenna performance, as it signifies that less power is effectively transmitted into the antenna. Mathematically, return loss is defined as [46], [47]:

$$RL[dB] = -10\log\frac{P_{ref}}{P_{in}} = -20\log(|\Gamma_{in}|) \tag{2.17}$$

where P_{ref} represents the power reflected back, P_{in} corresponds to the incoming power, and Γ_{in} indicates the reflection coefficient at the input of the transmission line.

CHAPTER 3
SINGLE ELEMENT DESIGN

3.1 Introduction

Microstrip patch antennas are widely employed as radiating elements in phased array systems for various wireless applications because of the several benefits they offer compared to other antenna configurations. They are particularly attractive due to their compact dimensions, cost-effective fabrication, lightweight structure, and low-profile design. Nevertheless, such antennas also have certain limitations, particularly their low gain. Over the years, various approaches have been explored to address these drawbacks; for instance, arranging them in an array can enhance their gain, making them highly suitable as effective radiating components, particularly in phased-array systems [48]. In this chapter, two individual patch radiators resonating at 28 GHz are modeled and presented. The first design employs a microstrip line (edge-fed) configuration, while the second compares the performance of inset-fed and gap-coupled feeding techniques. Since the dielectric substrate has a significant influence on the antenna's overall behavior, two different substrates with distinct dielectric constants and thicknesses, namely RT/Duroid 5880 and FR-4, are considered. The antenna models are simulated using CST Studio Suite, and their performance is compared with results obtained from HFSS.

3.2 Antenna Design Configurations

In Figure 3.1, the overall design process is illustrated through a flow chart. The procedure begins with the creation of an antenna element, intended to resonate at 28 GHz using fundamental design equations. The proposed structure is then simulated in CST Studio to evaluate its performance and verify whether it satisfies the required specifications. To enhance its efficiency, optimization of the antenna is carried out within CST. Finally, the simulation results obtained from CST are validated by comparing them with those generated using HFSS.

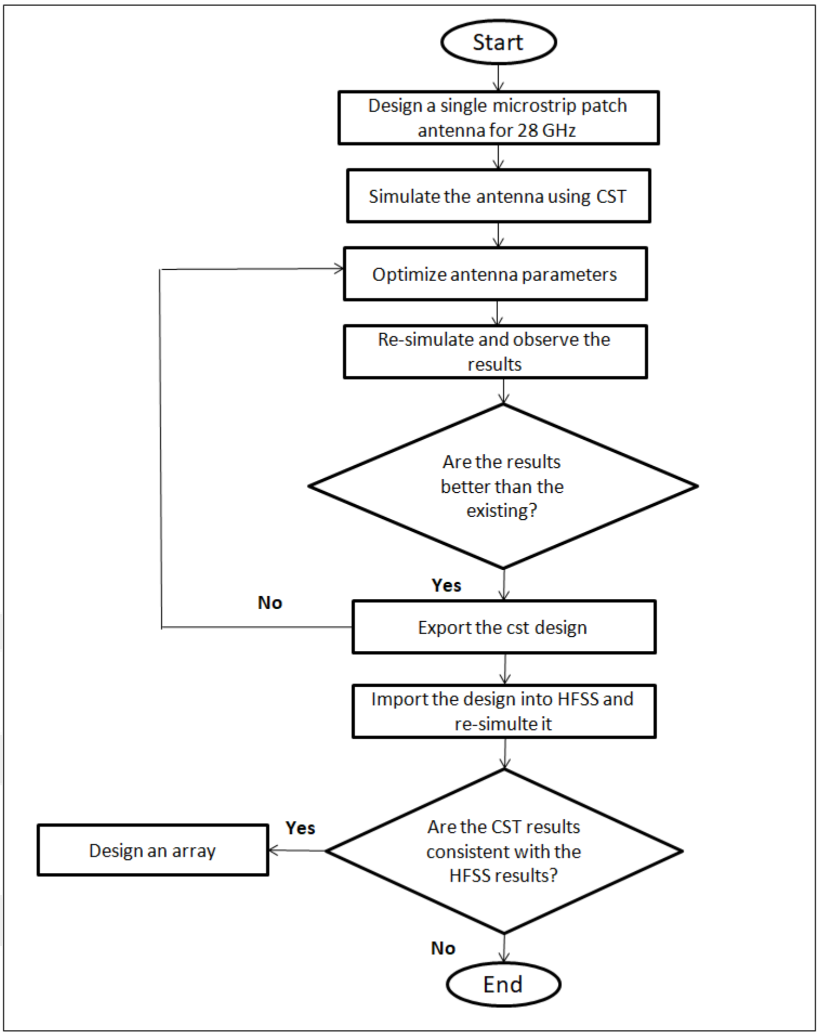

Figure 3.1 Part 1: workflow of the research study.

3.2.1 First Design: Dual-Slot Patch Antenna

To realize a phased array antenna for 5G wireless applications, the initial step involves designing a single patch antenna element. The implementation process of the patch antenna entails specifying key parameters, including the dielectric substrate, its relative permittivity (εr), thickness (h), and the desired resonant frequency (28 GHz). Based on these values, the physical dimensions of the antenna, including the patch length and width, can be calculated. In the millimeter-wave frequency range, selecting a suitable substrate is often challenging because many materials exhibit significant conductor losses. For this reason, substrates with a low loss tangent are particularly desirable for high-frequency applications. Achieving high gain is especially critical at these frequencies, as signals in the millimeter-wave band experience greater free-space path loss than signals at lower frequency bands. Therefore, minimizing dielectric and conductor losses through an appropriate substrate selection becomes essential for maintaining efficiency and enhancing the antenna gain. Rogers RT5880, with its extremely low loss factor (0.0009) and a relative permittivity of 2.2, is commonly employed for this application, as it ensures minimal signal degradation and supports high-gain performance, making it well-suited for 5G antenna designs [49], [50].

At high frequencies, the width of the feedline is commonly determined using the standard microstrip line impedance equation, which ensures proper matching with a 50 Ω source. For this design, the feedline width can be obtained from the following formula [32]:

$$Z_0 = \frac{120\pi}{\sqrt{\varepsilon_{reff}}\left[\frac{W_f}{h} + 1.393 + 0.667\ \ln\left(\frac{W_f}{h} + 1.444\right)\right]}, \frac{W_f}{h} \geq 1 \tag{3.1}$$

where, Z_0 denotes the characteristic impedance and W_f represents the width of the feedline. This calculation is critical for minimizing reflection losses and ensuring efficient power transfer.

Figure 3.2 depicts the configuration of the individual antenna element. The patch incorporates double U-shaped slots, which are introduced to realize resonance at the target frequency while enhancing radiation performance. The substrate has dimensions $ws \times ls$ mm^2 with a height of 0.51 *mm*, while the radiating patch measures $wp \times lp$ mm^2 and the microstrip feedline measures $wf \times lf$ mm^2. Both the feedline and the radiating patch are placed on the same substrate layer. In this design, copper is employed as the conducting material for the radiating element, transmission line, and antenna ground plane, with a thickness of 0.035 mm. Table 3.1 presents the optimized parameters of the slotted patch antenna. Figure 3.3 exhibits the sequential development of the slotted antenna element.

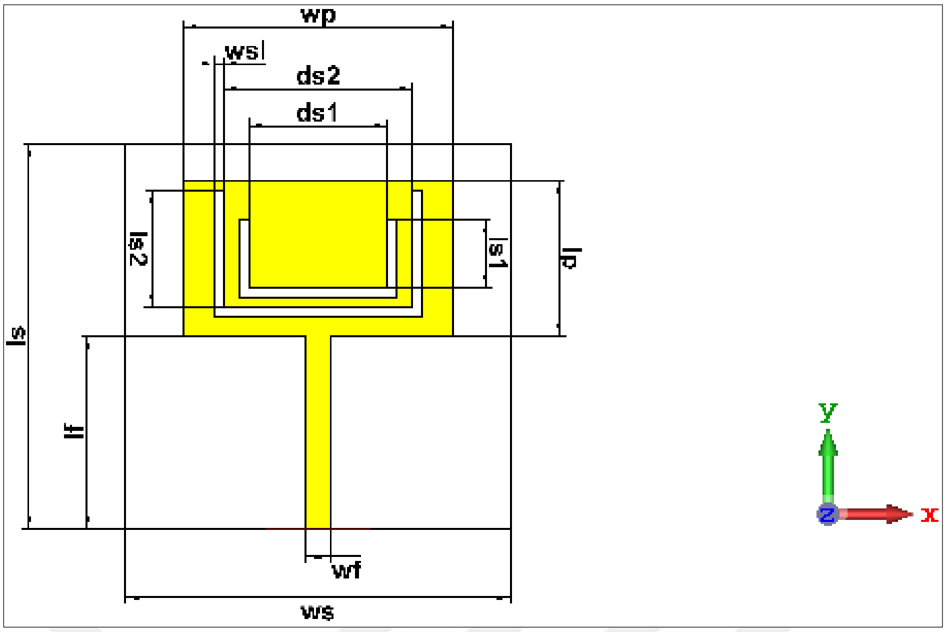

Figure 3.2 Geometry of the slotted patch antenna.

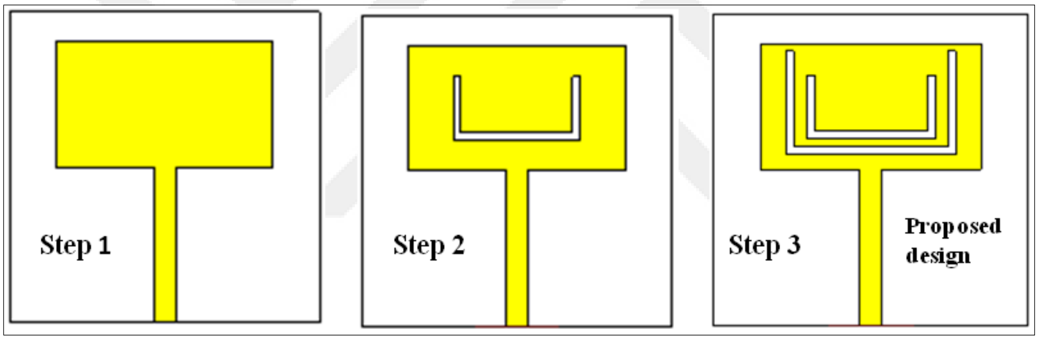

Figure 3.3 Stepwise development process of the slotted antenna element.

Table 3.1 List of optimized parameters for the slotted patch antenna

Parameter	Symbol	Dimension (mm)
Substrate length	ls	10
Substrate width	ws	10
Patch length	lp	4.05
Patch width	wp	7
First slot distance	ds1	3.6
Second slot distance	ds2	4.9
First slot length	ls1	1.78
Second slot length	ls2	3.05
Slot width	wsl	0.25
Feedline width	wf	0.7
Feedline length	lf	5

3.2.2 Second Design: Parasitic Antenna Element

This section presents the excitation of the rectangular patch antenna element using two different feeding techniques, which are compared. The technique demonstrating superior performance, based on gain and return loss, is then adopted for the patch antenna with parasitic element excitation. The ground plane and patch layers are realized in copper, with the ground plane having dimensions of 11.2 × 8.75 × 0.035 mm^3 (width × length × thickness). The structure is supported on an FR-4 substrate measuring 11.2 × 8.75 × 0.699 mm^3, exhibiting a relative permittivity of 4.3 and a tan δ of 0.025. FR-4 is selected as the substrate layer because it is a low-cost material that offers robust mechanical and electrical properties, is widely available, and is compatible with standard PCB fabrication processes. These characteristics make it suitable for achieving the required element spacing in antenna arrays while keeping production cost-effective [13].

Figure 3.4(a) illustrates the inset-fed patch, where the radiating element is directly connected to the feed line on the same plane, with a notch (l_s) forming the inset. The depth of this notch is determined to ensure impedance compatibility between the feedline and the patch, enabling effective power transfer and reducing reflections. For a rectangular microstrip patch, the input impedance at a distance l_s from the radiating edge is expressed as [32]:

$$R_{in}(l_s) = R_{edge}\cos^2\left(\frac{\pi l_s}{L}\right) \tag{3.2}$$

where R_{edge} is the input impedance at the patch edge and L is the patch length. The inset depth is selected such that R_{in} = R_0, where R_0 is the feed line characteristic impedance:

$$R_0 = R_{edge}\cos^2\left(\frac{\pi l_s}{L}\right) \tag{3.3}$$

Solving for l_s yields:

$$l_s = \frac{L}{\pi}\cos^{-1}\left(\sqrt{\frac{R_0}{\mathrm{R}_{edge}}}\right) \tag{3.4}$$

Figure 3.4(b) shows the gap-coupled feed configuration, where the radiating element is isolated from the feed line and excitation occurs through a narrow gap. At 28 GHz, this gap typically ranges from 0.1 to 0.3 mm. Smaller values are preferred due to the rapid variation of patch impedance at high frequencies, with an initial estimate of 1–5% of the patch length often serving as a practical guideline. The gap size plays a critical role in controlling coupling strength, impedance matching, and overall antenna performance [51]. The optimized design parameters of the single-element antenna for both feeding methods are summarized in Table 3.2. Based on simulation outcomes, the gap-coupled feed demonstrated superior performance compared to the inset-fed configuration. The detailed results will be presented in the next section. Therefore, the gap-coupled method was selected for the construction of the single patch antenna with parasitic element excitation.

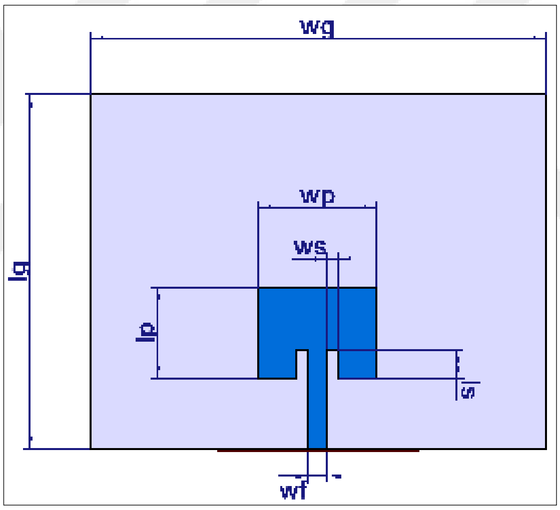

a) Inset-fed

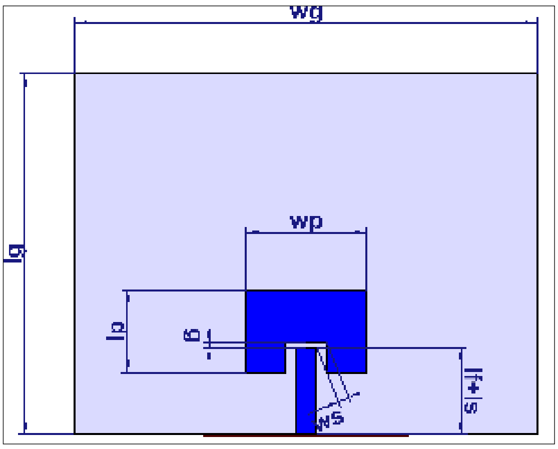

b) Gap-coupled fed

Figure 3.4 Microstrip patch antenna with two feeding methods.

Table 3.2 Optimized key parameters of the rectangular patch element for both feeding methods

Parameter	Symbol	Dimension (mm)
Patch Length	lp	2.28 (in inset feed) and 2 (in coupled feed)
Patch Width	wp	2.9
Substrate or ground Length	lg	8.75
Substrate or ground Width	wg	11.2
Transmission line Width	wf	0.5
Transmission line Length	lf	1.731
Slot length of the patch	ls	0.715
Slot Width of the patch	ws	0.25
Gap between feedline and the patch	g	0.1

For the phased array design, a rectangular microstrip patch with a parasitic element excited through a gap-coupled feed was selected. The configuration illustrated in Figure 3.4(b) was adopted as the basis for incorporating the parasitic element, while the layout of the top layer is exhibited in Figure 3.5. The upper layer of the single antenna element is composed of two rectangular radiating structures: a microstrip patch and a parasitic patch, separated by a distance *dp*. The inclusion of the parasitic element enables resonance at 28 GHz while simultaneously enhancing the antenna's gain. The antenna maintains the same dimensions as listed in Table 3.2, with the extra parameters required for the parasitic configuration summarized in Table 3.3.

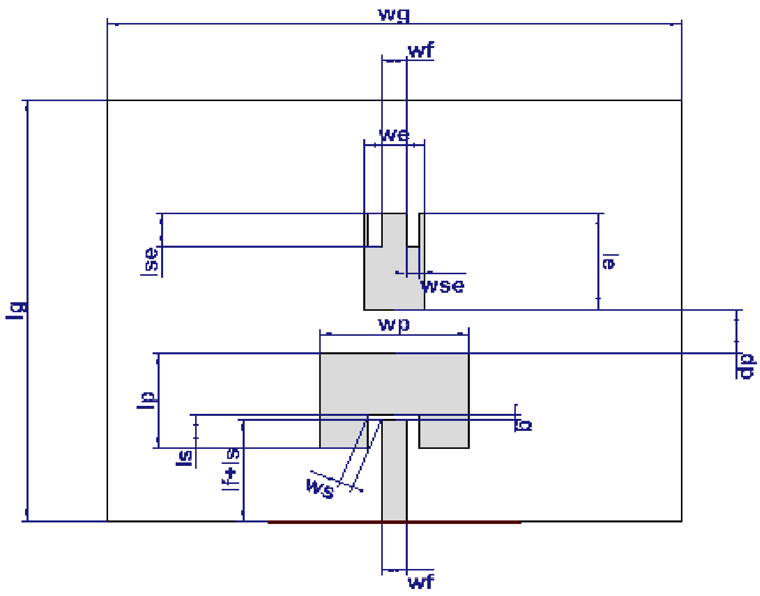

Figure 3.5 Microstrip patch with parasitic element antenna.

Table 3.3 Additional parameters of the rectangular patch radiator with parasitic element

Parameter	Symbol	Dimension (mm)
Length of the slot in the patch	ls	0.715
Width of the slot in the patch	ws	0.25
Length of the parasitic patch	le	2
Width of the parasitic patch	we	1.2
Slot length of the parasitic patch	lse	0.715
Slot width of the parasitic patch	wse	0.25
Distance between patches	dp	0.9
Gap	g	0.1

3.3 Simulation Results of the Single-Element Patch Antenna

3.3.1 Slotted Patch Antenna

This section presents the key simulation results (S_{11}, VSWR, gain, radiation characteristics, and overall efficiency) of the slotted patch antenna element. Figure 3.6 illustrates the S_{11} response across each design step. The designed patch attains an S_{11} of −21.6 dB at 28.3 GHz, in contrast to other configurations that exhibit resonance at distinct frequencies. The incorporation of two slots enables the antenna to achieve resonance at the target frequency with minimal loss, providing a −10 dB frequency bandwidth exceeding 2 GHz, thereby encompassing the 5G frequency band (27.5–28.35 GHz) as specified by the FCC [52]. As shown in Figure 3.7, the proposed patch attains a VSWR of 1.2 at 28 GHz, which lies within the acceptable range of $1 \leq \text{VSWR} \leq 2$ [47], indicating high efficiency and confirming that a large portion of the supplied power is successfully radiated.

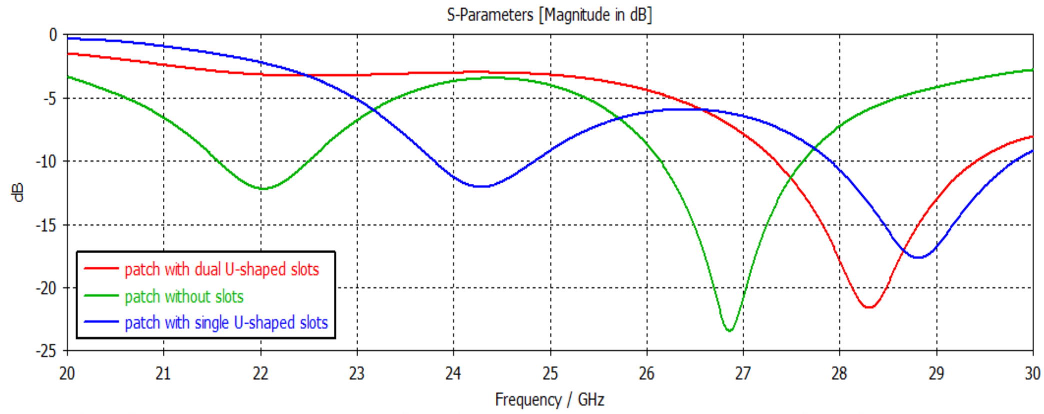

Figure 3.6 Scattering parameters of the slotted radiating patch antenna.

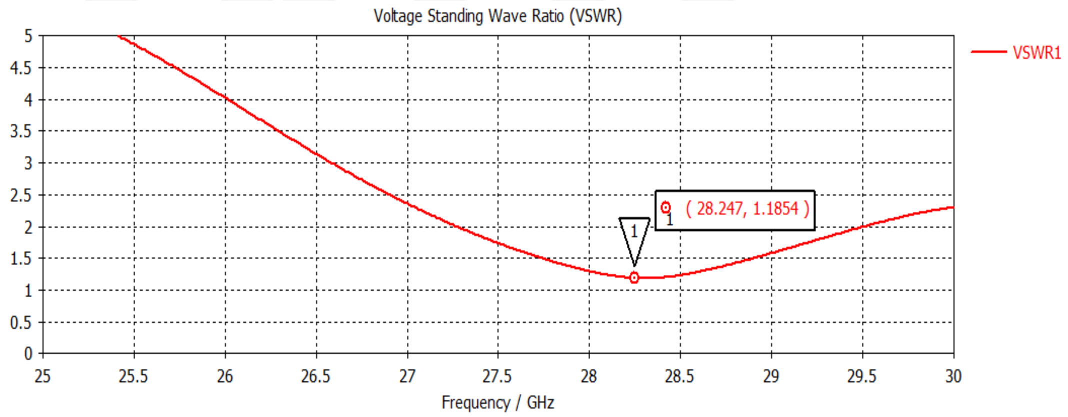

Figure 3.7 VSWR of the slotted radiating patch antenna.

Figure 3.8 depicts the radiated gain of the slotted patch antenna at every design stage across frequency, while Figure 3.9 illustrates the 3D far-field radiation patterns for each stage, highlighting the antenna's radiation behavior. The results effectively show the effect on the antenna gain due to the slots, with the proposed double-slotted patch achieving 8.4 dBi at 28 GHz, compared to 6.5 dBi and 7.9 dBi for the unslotted and single-slotted patches, respectively. The proposed single-element antenna exhibits a directivity of approximately 8.6 dBi and a realized gain of 8.3 dBi. As shown in Figure 3.10, at $\phi = 90°$, the antenna's main beam points at 9°, with a sidelobe level of −15.4 dB and an angular width of 79°. When $\phi = 0°$, the antenna radiates at 0°, achieving a lower sidelobe level of −23.6 dB and a narrower angular width of 69.7. In addition, it attains above 95% radiation efficiency and nearly 94% total efficiency, confirming effective power radiation. At 28 GHz, the patch with no slots achieved about 77% total efficiency, while the patch with one slot reached 87.5%. These results indicate that the inclusion of slots significantly improves antenna efficiency; therefore, the dual-slotted patch antenna was chosen as the one-element patch configuration for antenna array design due to its superior performance.

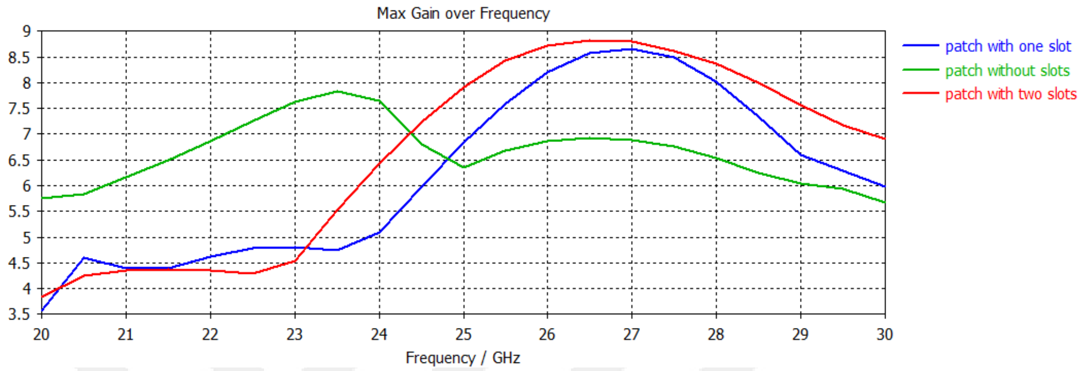

Figure 3.8 Peak gain versus frequency for the slotted radiating patch antenna.

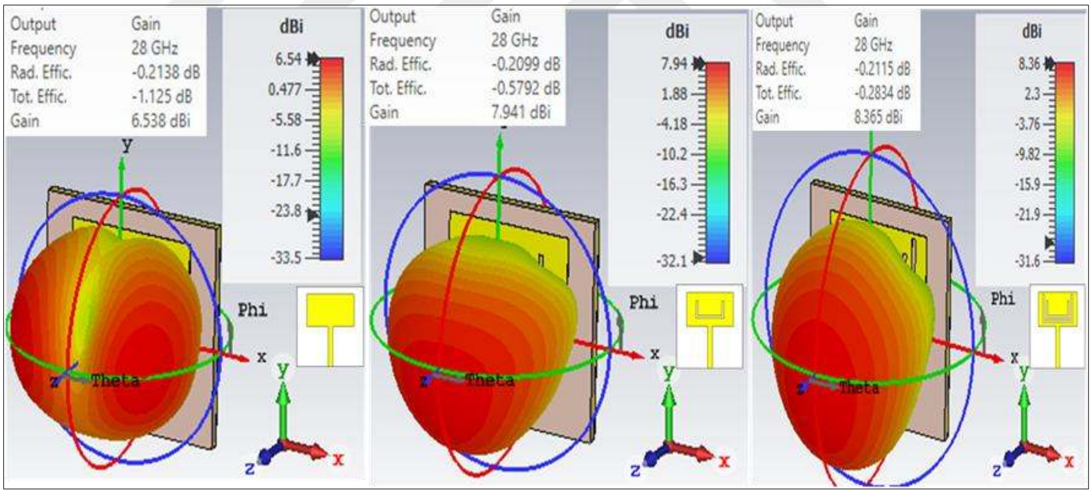

Figure 3.9 3D radiation pattern of the slotted radiating patch antenna.

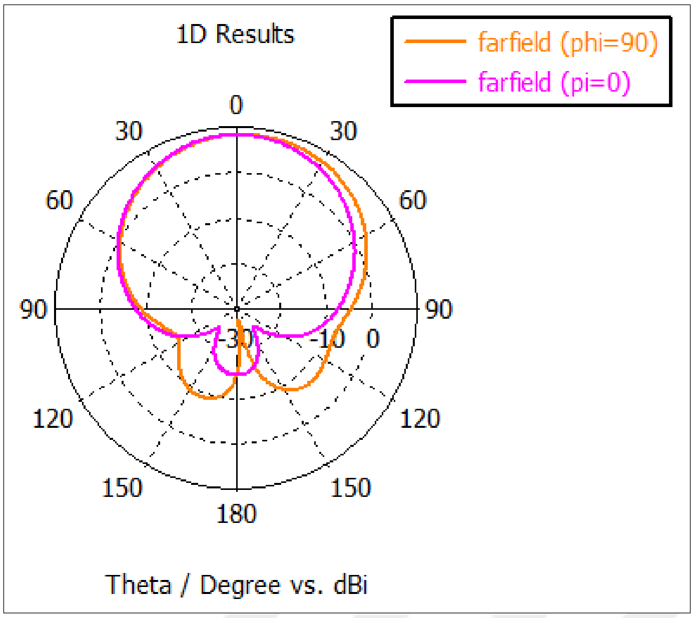

Figure 3.10 Single-plane radiation pattern of the slotted radiating patch antenna.

3.3.2 Parasitic Patch Antenna

In this part, the CST simulation results of the rectangular radiating patch using two feeding techniques are analyzed, showing that the gap-coupled feed outperforms the inset-fed configuration in terms of gain and return loss, and is therefore selected to excite the parasitic patch antenna. Figure 3.11 illustrates the S_{11} parameter for both configurations. The inset-fed patch exhibits an S_{11} of −19 dB, with a −10 dB bandwidth of 2 GHz centered at 28 GHz, while the gap-coupled patch achieves a lower S_{11} of −35 dB and a slightly wider −10 dB bandwidth of 2.3 GHz at the same frequency.

The 3D far-field gain results for both feeding techniques are presented in Figure 3.12. From this figure, it is evident that the gap-coupled radiating patch antenna achieves a gain of 6.7 dBi, while the inset-fed patch attains 5.8 dB. Figure 3.13 compares the maximum gain response of both designs, showing that the gap-coupled feed provides a higher peak gain than the inset-fed configuration. These results confirm that the microstrip patch with a gap-coupled feed outperforms the inset-fed configuration in terms of gain. Therefore, the gap-coupled feed was selected for the construction of the microstrip patch with parasitic elements. Subsequent far-field simulations will show that the addition of the parasitic component further improves the gain of the antenna and overall performance.

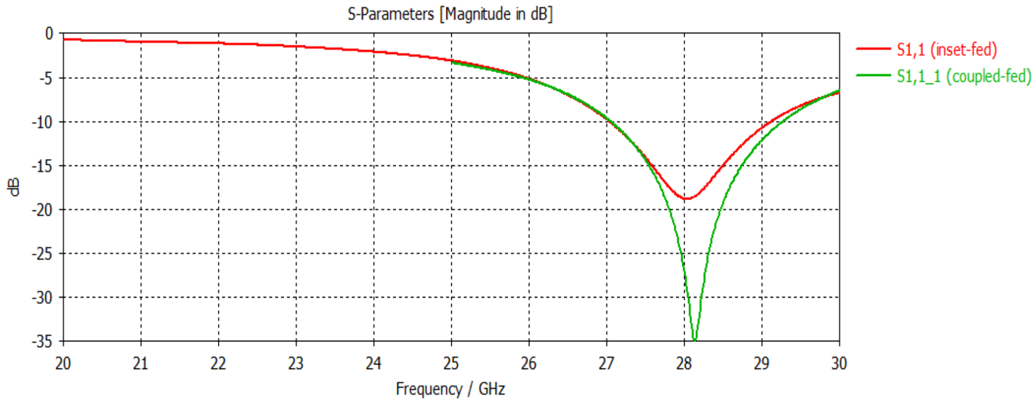

Figure 3.11 Simulated reflection coefficient of the rectangular microstrip patch for two feeding methods.

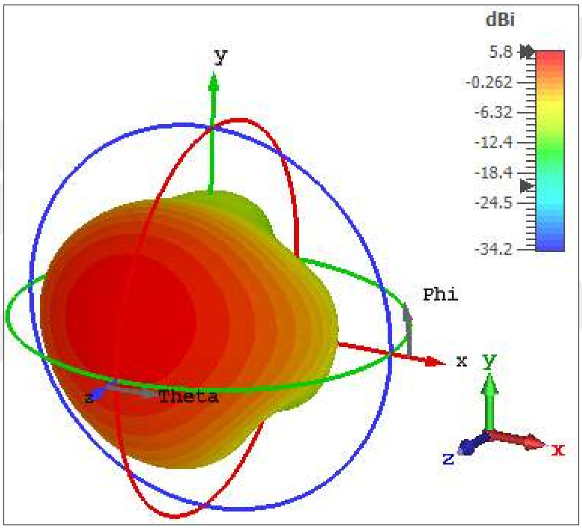

a) Inset-fed

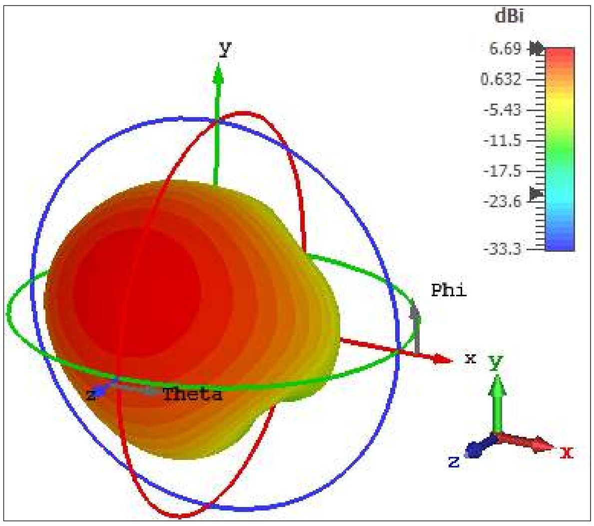

b) Gap coupled-fed

Figure 3.12 3D far-field gain of the microstrip patch for two feeding methods.

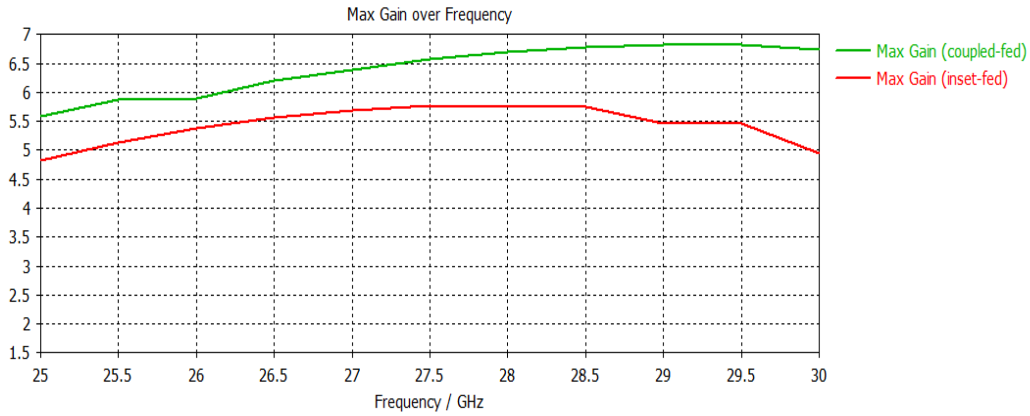

Figure 3.13 Variation of maximum gain with frequency for the microstrip patch antenna using two feeding approaches.

The behavior of the patch antenna featuring a parasitic element was analyzed with respect to S_{11}, operating bandwidth (−10 dB), VSWR, radiation pattern, and gain. The S_{11} response of the proposed patch antenna with a parasitic element design is illustrated in Figure 3.14, where this antenna achieves an S_{11} value of −24 dB at 28 GHz. An S_{11} less than −10 dB is maintained across the 27–29.8 GHz frequency range. The corresponding VSWR response is presented in Figure 3.15, yielding a favorable value of 1.1 at 28 GHz, well within the acceptable range (≤ 2). The effect caused by the parasitic element on the antenna's gain was investigated. Figure 3.16 presents the 3D far-field gain of the proposed parasitic-loaded patch, which achieves 7.7 dBi at 28 GHz. For comparison, the single patch without the parasitic element (Figure 3.12(b)) attains only 6.7 dBi, indicating a 1 dB improvement. This enhancement in gain justifies the use of the parasitic-element configuration as the single-element design for the phased array. Furthermore, the proposed parasitic patch antenna exhibits a 9.5 dBi directivity and a 7.7 dBi realized gain at 28 GHz. As shown in Figure 3.17, at ϕ = 90°, the parasitic patch radiates at 29°, exhibiting a sidelobe level of −14 dB and an angular width of 57°. When ϕ = 0°, the parasitic patch radiates at 0°, with a sidelobe level of −17 dB and an angular width of 76.3°.

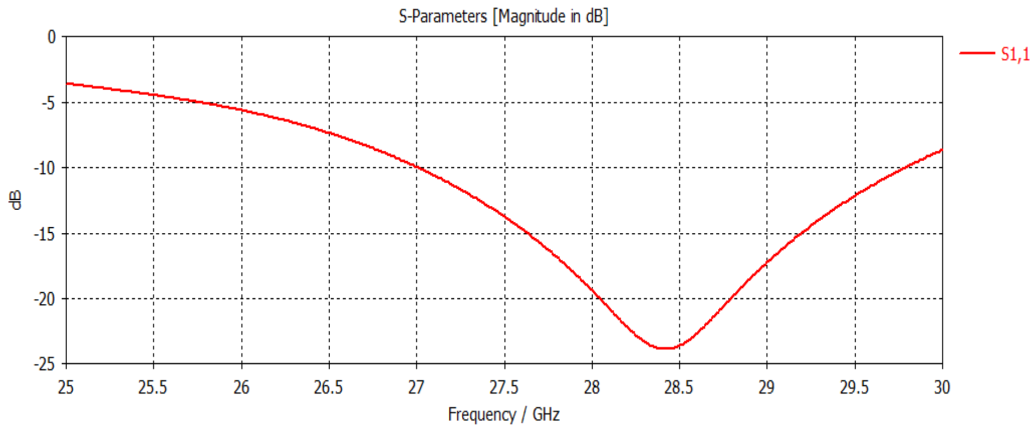

Figure 3.14 S_{11} of the patch antenna with a parasitic element.

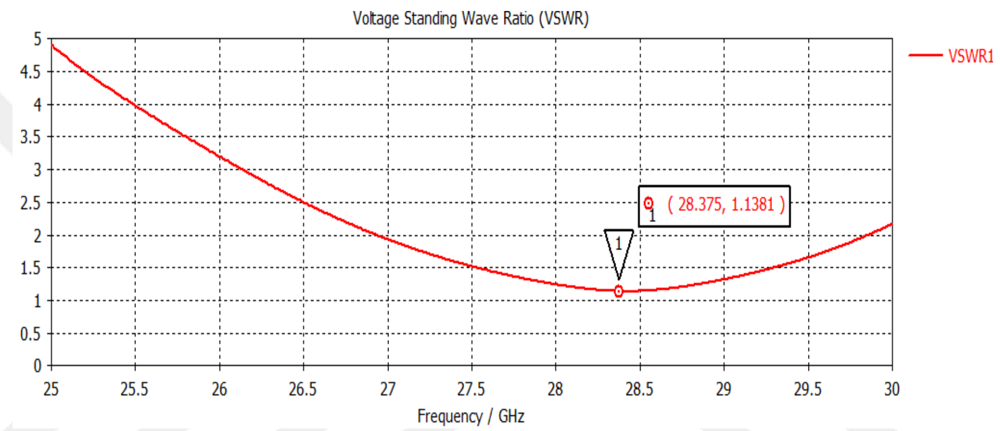

Figure 3.15 VSWR of the patch antenna with a parasitic element.

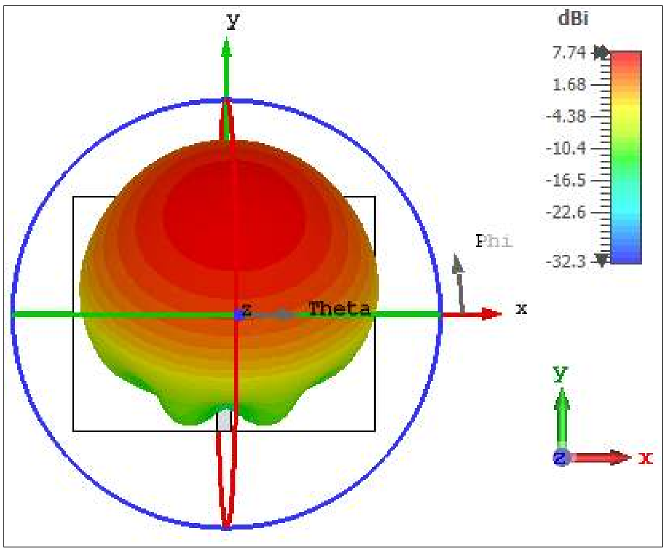

Figure 3.16 3D gain radiation pattern of the patch antenna with a parasitic element.

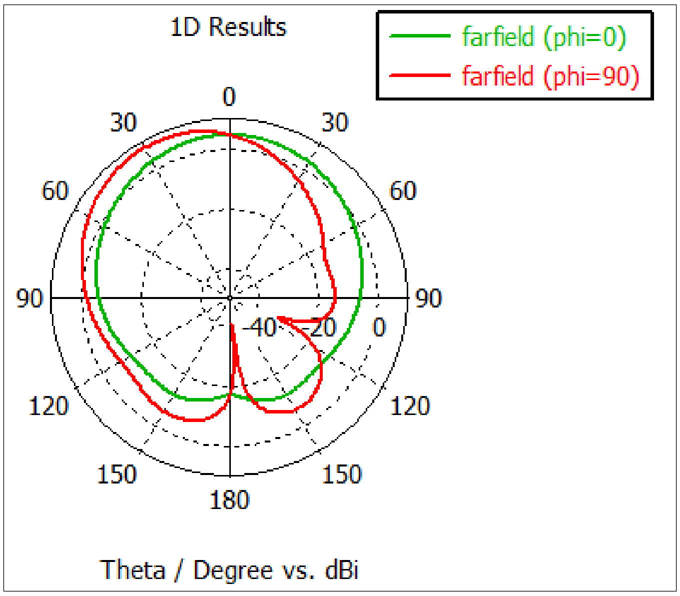

Figure 3.17 Single-plane radiation pattern of the patch antenna with a parasitic element.

3.4 Results Verification

To ensure the reliability of the CST simulation results, verification was performed using ANSYS HFSS, a widely adopted full-wave electromagnetic solver. This section presents the performance evaluation of the proposed antennas, namely the slotted patch and the parasitic patch, which are re-simulated using HFSS. The results obtained from both tools are evaluated based on their return loss (S_{11}), 10-dB frequency bandwidth, VSWR, gain, and radiation pattern. This cross-comparison provides confidence in the accuracy of the CST simulations and validates the proposed antenna designs.

3.4.1 Slotted Patch Antenna

As depicted in Figure 3.18, the slotted patch antenna element obtains an S_{11} of −17.5 dB at 28.6 GHz in HFSS, which is close to the CST result of −21.6 dB at 28.3 GHz, showing a slight frequency shift. The −10 dB bandwidth is 2 GHz, fully encompassing the 5G band (27.5–28.35) GHz. Furthermore, as illustrated in Figure 3.19, the antenna obtains an input VSWR value of 1.3 at 28.5 GHz in HFSS, which is close to the CST-obtained value of 1.2 at 28.3 GHz, confirming the consistency between both simulation tools. The slight differences observed between CST and HFSS are normal and arise from the distinct numerical methods employed by each simulator: CST uses a time-domain solver (FDTD), while HFSS employs a frequency-domain solver (FEM). These methodological differences can cause minor variations in resonant frequencies, gain, and bandwidth.

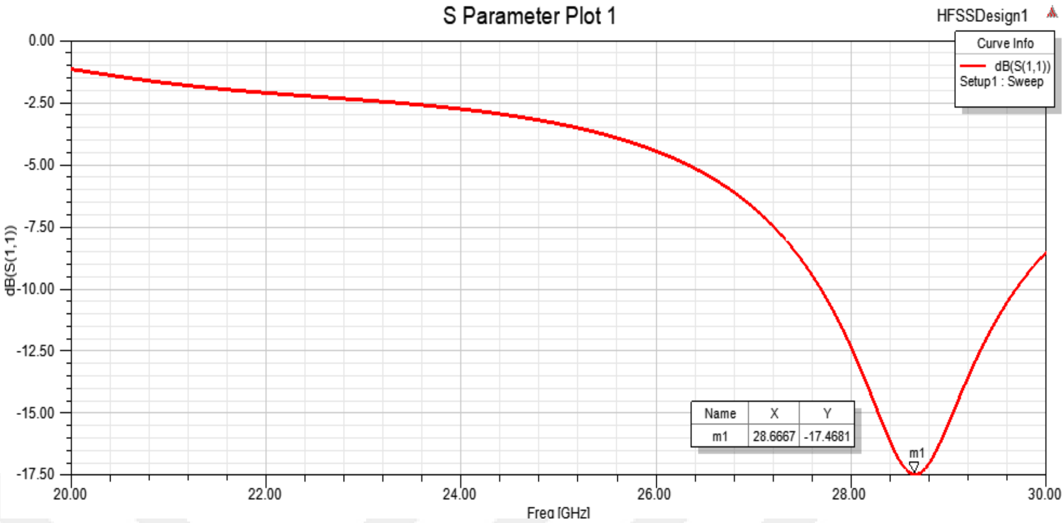

Figure 3.18 S-parameters of the slotted patch antenna element using HFSS.

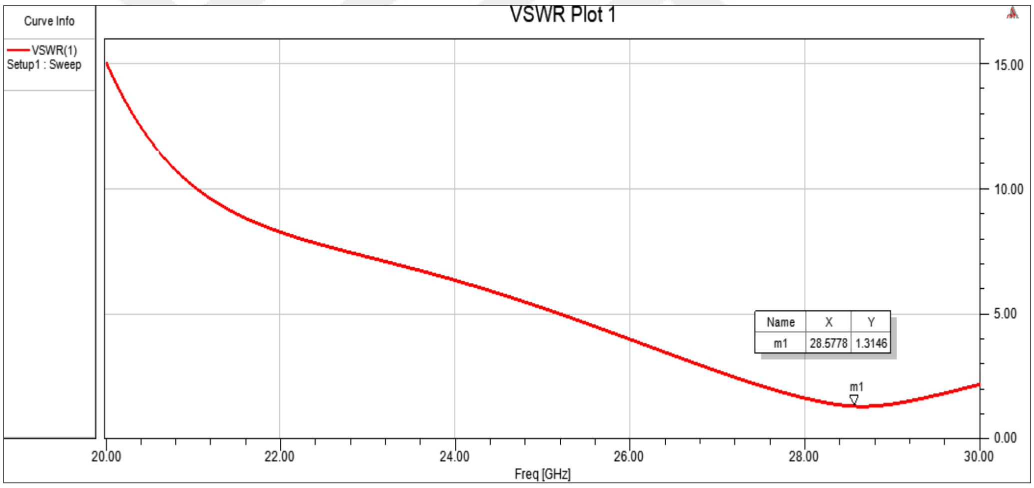

Figure 3.19 VSWR of the slotted patch antenna using HFSS.

In Figure 3.20, the slotted patch antenna achieves a gain of 9 dBi at 28 GHz, which is slightly higher than the CST result of 8.4 dBi. Furthermore, HFSS reports 9 dBi directivity with 8.8 dBi realized gain. These values are marginally greater than those obtained in CST, where the directivity and realized gain were 8.6 dBi and 8.3 dBi, respectively, at 28 GHz. As shown in Figure 3.21, the radiation patterns of the slotted patch obtained in HFSS closely match those achieved in CST. At $\phi = 90°$, the slotted patch achieves an angular width of 71.3°, which is comparable to the CST result of 79°. When $\phi = 0°$, the slotted patch attains an angular width of 65.2°, which is also close to the CST result of 69.7°. Despite these minor differences, the results remain in good agreement with the CST values. Overall, all evaluated parameters (gain, directivity, realized gain, main lobe direction, and angular width) are reasonably close in HFSS compared to CST, and the results are closely match, confirming the reliability of the simulation outcomes.

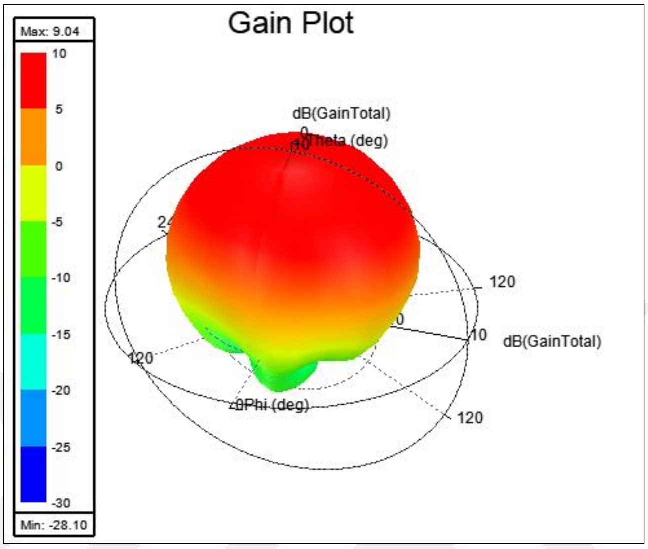

Figure 3.20 3D far-field gain of the slotted antenna element using HFSS.

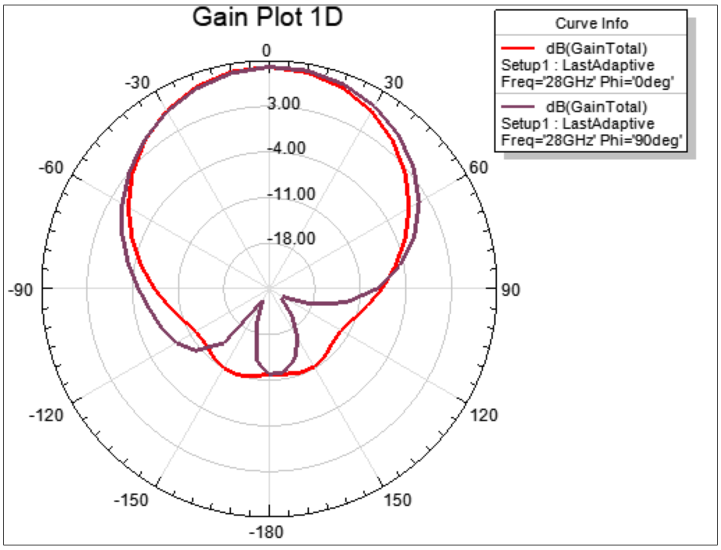

Figure 3.21 1D radiation pattern of the slotted antenna element using HFSS.

3.4.2 Parasitic Patch Antenna

This section presents the CST results of the patch antenna with a parasitic element, including return loss, 10-dB bandwidth, VSWR, radiation pattern, and gain, are compared with those obtained using HFSS. As exhibited in Figure 3.22, the S_{11} response of the parasitic patch is −19 dB at 28.3 GHz, close to the −24 dB obtained in CST at the same frequency. In HFSS, the patch operates over 27–29.5 GHz, showing good agreement with the 27–29.8 GHz range achieved in CST. The VSWR response in Figure 3.23 indicates a value of 2 at 28 GHz, higher than the CST result of 1.1 but still within the acceptable range (≤ 2). Furthermore, Figure 3.24 shows that HFSS reports a gain of 7.9 dBi, slightly higher than the 7.7 dBi achieved in CST. As shown in Figure 3.25, the radiation pattern of the parasitic patch obtained in HFSS closely matches that of CST. In HFSS, the parasitic patch radiates at an angle of 28°, close to the CST result of 29°, with a half-power beamwidth of 53°, comparable to the CST result of 57°. Furthermore, when ϕ = 0°, the parasitic patch radiates at 0°, consistent with the CST result, with an angular width of 94°, which is slightly higher than the CST value of 76.3°. Despite these minor discrepancies, the results demonstrate close agreement between the two simulation tools, confirming the reliability of the patch antenna design with a parasitic component.

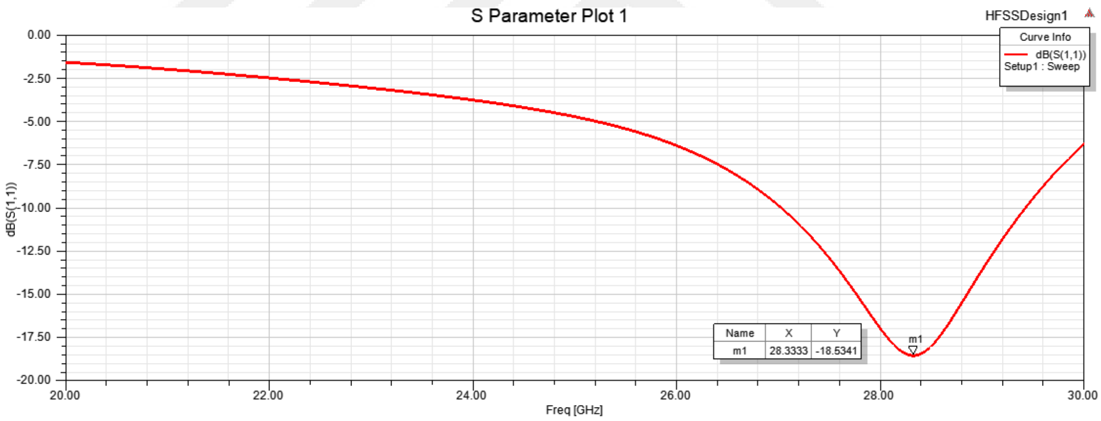

Figure 3.22 S-parameters of the patch antenna with a parasitic element using HFSS.

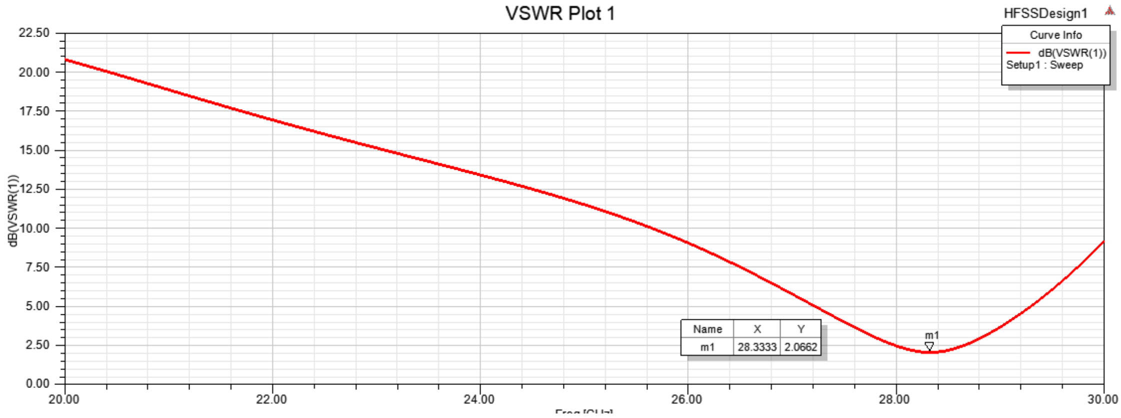

Figure 3.23 VSWR of the patch antenna with a parasitic element using HFSS.

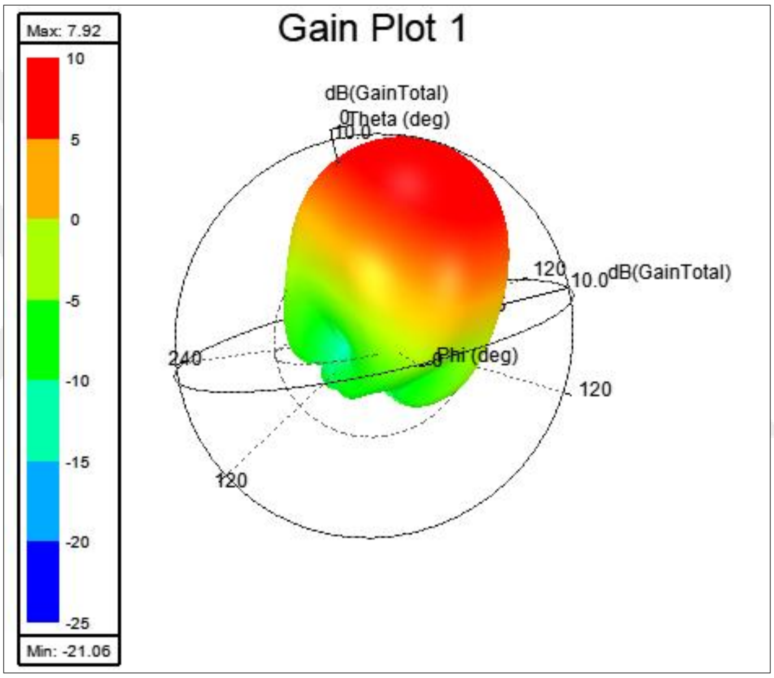

Figure 3.24 3D far-field gain of the patch antenna with a parasitic element using HFSS.

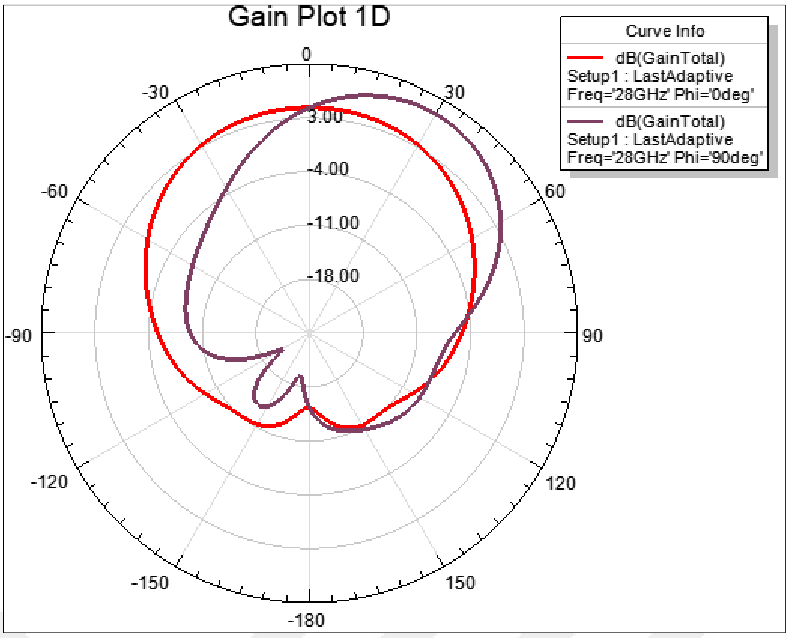

Figure 3.25 Single-plane radiation pattern of the patch antenna with a parasitic element using HFSS.

CHAPTER 4
PHASED ARRAY ANTENNA DESIGN

4.1 Introduction

Millimeter-wave (mmWave) frequencies suffer from considerable path and propagation losses, which pose a significant challenge for reliable wireless communication. To mitigate these losses without additional power consumption or cost, high-gain antenna arrays are commonly employed. However, the narrow radiation beams associated with high gain restrict angular coverage. Phased array antennas overcome this limitation by enabling electronic beam steering toward desired directions. Owing to their combined advantages of high gain and flexible beam steering, phased array antennas have recently gained increasing attention for 5G wireless applications. The main drawback of such arrays, however, is the presence of high sidelobe levels and grating lobes at distinct steering angles, which can severely interfere with communication. Hence, it becomes essential to minimize the peak sidelobe level while maintaining the desired main beam characteristics. Several techniques, such as modifying the number of array elements, adjusting their spacing, and applying tapering functions, have been developed to suppress sidelobe levels, with amplitude tapering being the most widely used and particularly effective for uniform linear arrays. However, increasing the number of elements significantly raises cost, while increasing the inter-element spacing leads to grating lobes. In contrast, applying windowing techniques allows sidelobe reduction with fewer elements, thereby lowering cost and avoiding grating lobes. Nonetheless, different windowing methods involve a trade-off between sidelobe suppression and antenna gain or directivity, making it essential to carefully manage these competing factors in antenna design, depending on the intended application of the antenna [4], [12], [53–59].

In the preceding chapter, two single patch antennas designed to operate at 28 GHz were simulated using CST, and the results were validated through HFSS simulations. This chapter presents a performance comparison between two phased array antennas developed and simulated in CST for 28 GHz 5G applications. A 1 × 10 array based on a slotted patch element is first designed, followed by a 1 × 8 array employing a parasitic patch element. To enable phased-array operation, progressive phase shifts are applied at the excitation ports of both arrays for beam steering. Based on this comparison, the array that exhibits the highest gain and effective beam-steering capability is further optimized for sidelobe suppression using ten different window functions. The resulting trade-offs between sidelobe level reduction and gain are analyzed. The optimized array is subsequently compared with recent designs reported in the literature. Furthermore, the performance of both arrays obtained from CST is cross-verified using HFSS to ensure consistency. Finally, the array achieving the best overall performance is fabricated and experimentally tested to measure its return loss and validate its operation at the target frequency.

4.2 Phased Array Antenna Design Configurations

Figure 4.1 presents a flowchart illustrating the overall design methodology. The process begins with constructing 1 × 10 and 1 × 8 array configurations from single patch elements to enhance the antenna gain, with both arrays designed to operate at 28 GHz. These array antennas are initially modeled and simulated in CST to verify compliance with the key 5G requirement of achieving a minimum gain of 12 dBi [60–62]. Once this criterion is satisfied, beam steering is introduced to improve angular coverage, with the steering mechanism described in detail later in this chapter. Subsequently, a tapering technique is applied to the array that demonstrates the highest gain and effective beam steering performance to further suppress sidelobe levels. The resulting performance is evaluated using ten different window functions. Finally, the CST simulation results are cross-verified with HFSS simulations to ensure consistency and validation of the design accuracy.

4.2.1 First Design: Slotted Array Antenna

The designed array consists of ten doubly U-shaped slotted patch elements, occupying a total size of $w_a \times l_a\ mm^2$. This configuration is derived from the single-element antenna described in Section 3.2.1. The detailed dimensions of the 10-element array are provided in Table 4.1. As shown in Figure 4.2, the elements are uniformly spaced and aligned linearly along the x-axis. The inter-element spacing is

6.80 mm, which corresponds to approximately 0.64λ at 28 GHz (λ ≈ 10.7 mm in free space), placing it within the typical design range of 0.5λ to 0.9λ [52].

4.2.2 Second Design: Parasitic Array Antenna

The designed array comprises eight patch elements arranged in a linear configuration with uniform spacing, as depicted in Figure 4.3. The size of the array is $w \times l\ mm^2$, with the individual patches separated by a spacing of s. The detailed parameters of the array are summarized in Table 4.2.

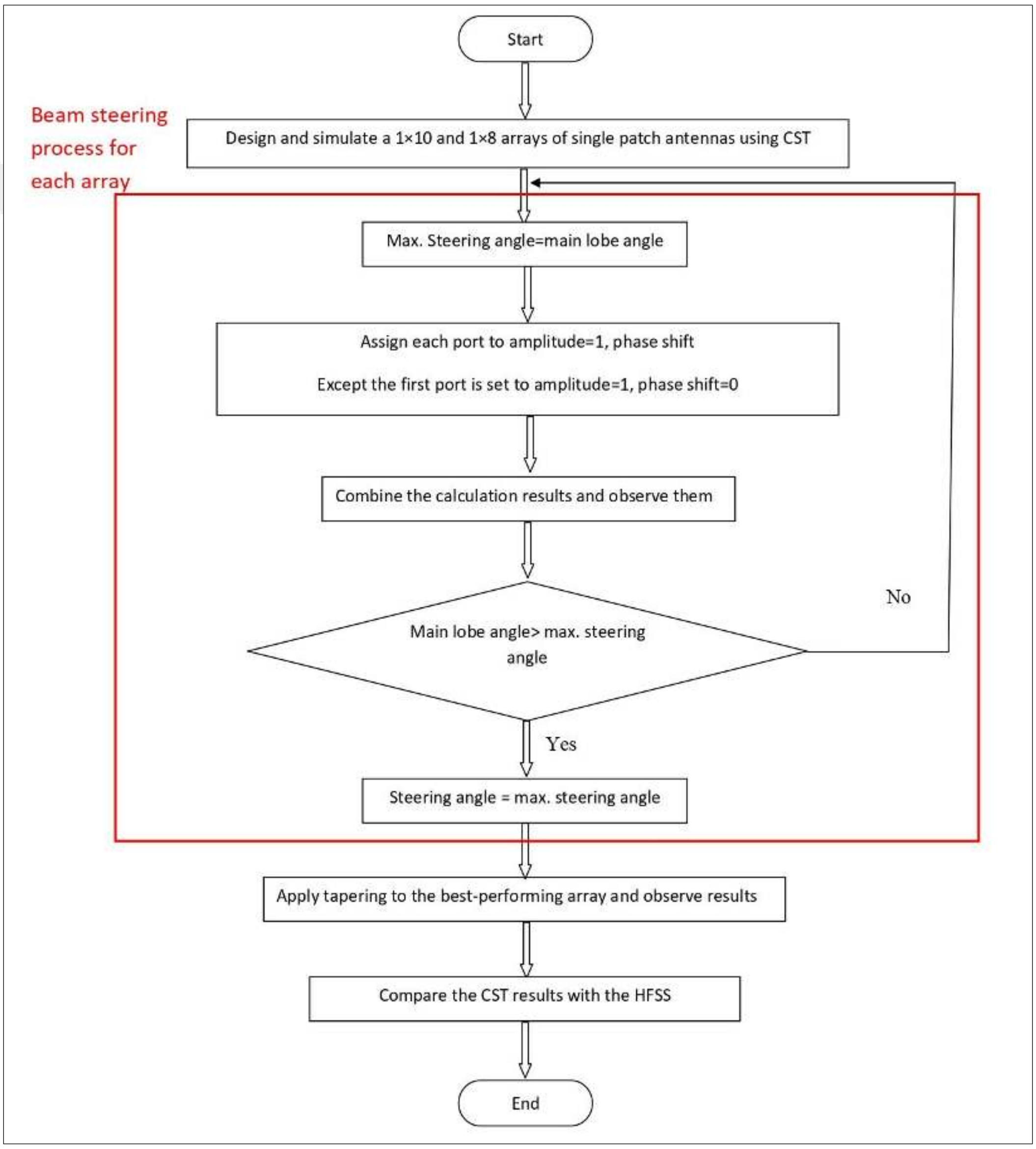

Figure 4.1 Part 2: workflow of the research study.

Table 4.1 Design parameters of the slotted patch array antenna

Parameter	Symbol	Dimension (mm)
Array length	l_a	10
Array width	w_a	77.5
Interelement spacing	d	6.80

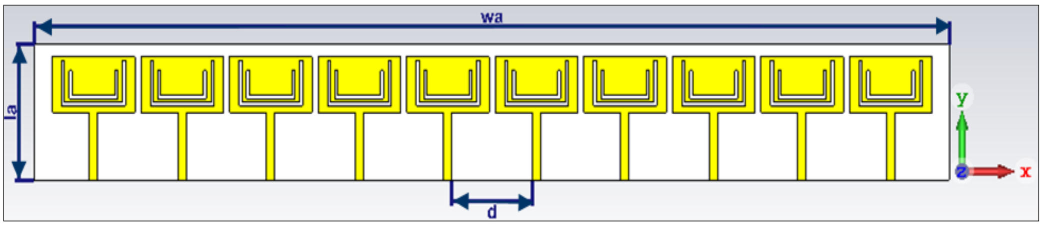

Figure 4.2 Structure of the proposed slotted array antenna.

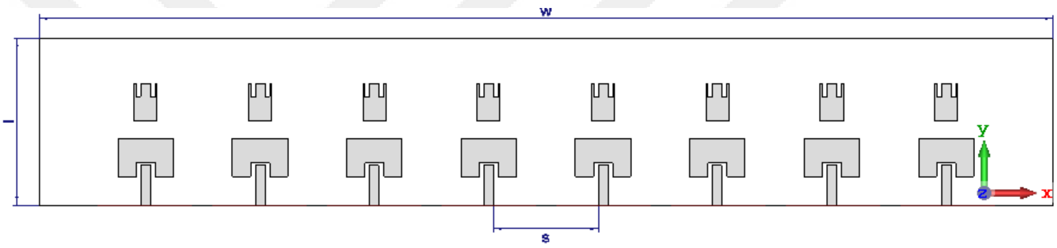

Figure 4.3 Structure of the proposed parasitic array antenna.

Table 4.2 Design parameters of the parasitic patch array antenna

Parameter	Symbol	Dimension (mm)
Array length	l	8.75
Array width	w	53.2
Interelement spacing	s	5.5

4.2.3 Beam Steering Mechanism

As illustrated in Figure 4.1, the proposed linear arrays utilize progressive phase excitation to direct the main beam across the visible region [38]. Before analyzing the beam-steering performance, a progressive phase shift was introduced across all excitation ports, while the first port was maintained at 0°. For an N-element phased array, the phase shift configuration can be expressed as:

$$\beta_n = n.\beta_0 \tag{4.1}$$

where β_n represents the phase shift for the n-th element and β_0 denotes the phase increment. For instance, if β_0 is set to 100°, the corresponding phase shifts for the elements are 0°, 100°, 200°, and so on, up to *(N-1).100°* for the N-th element. During this procedure, the excitation amplitude was maintained constant for all elements. After setting the amplitude and phase excitations, the directional radiation pattern was obtained by superposing the radiation patterns of all individual elements, resulting in a beam steered toward the desired direction.

4.2.4 Windowing-Based Tapering Method for Sidelobe Reduction

In phased array antennas, one of the major performance challenges is the presence of high sidelobe levels, which may contribute to unwanted interaction and reduced communication efficiency. To tackle this issue, amplitude tapering techniques are commonly applied, where the amplitude coefficients of the radiating elements are adjusted according to specific window functions. By reducing the coefficients of end elements relative to the central ones, windowing effectively suppresses sidelobes while preserving the desired main beam shape. However, this approach typically involves a trade-off between sidelobe suppression and antenna gain or directivity. In this work, ten different window functions are investigated and compared, with their mathematical expressions provided in Table 4.3, to evaluate their impact on the sidelobe performance and overall efficiency of the proposed best-performing array.

Table 4.3 Window functions applied to the array elements, with their equations adapted from [57], [58], [63], and [64]

Window Name	Equation	Eq. No.
Hanning	$win(n) = 0.5(1 - cos(2\pi \frac{n}{N-1}));0 \le n \le N-1$	(4.2)
Hamming	$win(n) = 0.54 - 0.46cos(2\pi \frac{n}{N-1});0 \le n \le N-1$	(4.3)
Blackman	$win(n) = 0.42 - 0.5\cos\left(\frac{2\pi n}{N-1}\right) + 0.08\cos\left(\frac{4\pi n}{N-1}\right);;0 \le n \le \frac{N}{2} - 1$	(4.4)
Blackman-Harris	$win(n) = A_0 - A_1\cos\left(\frac{2\pi n}{N}\right) + A_2\cos\left(\frac{4\pi n}{N}\right) - A_3\cos\left(\frac{6\pi n}{N}\right);0 \le n \le \frac{N}{2} - 1$ where A_0=0.35875; A_1=0.48829; A_2=0.14128; A_3=0.01168	(4.5)
Bartlett Window or Triangular	$win(n) = \left\{ \begin{array}{l} \frac{2n-1}{N};1 \le n \le \frac{N}{2} \\ 2 - \frac{(2n-1)}{N};\frac{N}{2}+1 \le n \le N \end{array} \right\}$	(4.6)
Barthann (Modified	$win(n) = 0.62 - 0.48\left|\left(\frac{n}{N-1} - 0.5\right)\right| + 0.38\cos\left(2\pi\left(\frac{n}{N-1} - 0.5\right)\right);0 \le n \le N-1$	(4.7)

Bartlett-Hann)		
Chebyshev	$win(n)=\frac{\psi(n,N)\cos(\pi\sqrt{n^2-A^2})}{\cos\pi\sqrt{-A^2}}$, where $A=\frac{\ln(\eta+\sqrt{\eta^2-1})}{\cos\pi\sqrt{-A^2}}$, $\eta=10^{\frac{-S}{20}}$ where S represents the sidelobe level and ψ determines the sign of the expression	(4.8)
Welch	$win(n)=1-\left(\frac{n-\frac{N}{2}}{\frac{N}{2}}\right)^2$;$0\le n\le N$	(4.9)
Gaussian	$win(n)=\exp\left(-\frac{1}{2}\left(\frac{n-\frac{N}{2}}{\sigma\frac{N}{2}}\right)^2\right)$;$0\le n\le N, \sigma\le 0.5$ The Gaussian function is characterized by a standard deviation of $\sigma\cdot N/2$ samples	(4.10)
Exponential or Poisson	$win(n)=\exp\left(-\left\|n-\frac{N}{2}\right\|\frac{1}{\tau}\right)$, where τ denotes the time constant of the function, defined as N/2	(4.11)

4.3 Simulation Results of the Array Antennas

4.3.1 Slotted Array Antenna

Prior to running the simulations, all array elements were excited with equal amplitudes, while a progressive phase shift was applied according to their respective positions. The resulting fields were then integrated to analyze the steering behavior. Figure 4.4(a) illustrates the scattering parameters of the slotted array across frequency. At 28.2 GHz, the elements displayed minimal reflection values, ranging between −27 dB and −67.5 dB. Specifically, the first and last elements showed |S11| values of about −27 dB, whereas the intermediate elements achieved values within the range of −49.4 dB to −67.5 dB. The observed variations are caused by interelement mutual coupling, which impacts the reflection behavior of the developed array. The simulation outcomes indicate that the presented array achieves a frequency bandwidth of > −10 dB, spanning 26.7 to 29.6 GHz, thereby covering and exceeding the 27.5–28.35 GHz band. Furthermore, at 28.2 GHz, the inter-element mutual coupling remains below −30 dB, as displayed in Figure 4.4(b).

The frequency-dependent maximum gain of the antenna element and the overall array was analyzed, as illustrated in Figure 4.4(c). It can be observed that the proposed array enhances the gain at 28 GHz, ranging from 8.4 to 18.5 dBi. The combined 3D beam pattern of the array, shown in Figure 4.5, was employed to evaluate the radiation performance. The proposed array exhibited a high directivity value of 18.8 dBi and an 18.5 dBi realized gain. At the θ-plane (ϕ = 0°), the main beam was oriented at 0° with a sidelobe level of −13.4 dB and a narrow angular width of 7°, as shown in Figure 4.6. In contrast, at ϕ = 90°, the main beam radiated at 4° with a sidelobe level of −21.1 dB and a much wider angular width of 68.1°. The radiation pattern confirms excellent behavior, demonstrating a radiation efficiency close to 95% along with high antenna efficiency. Importantly, even with the presence of mutual coupling between elements, the overall efficiency remained unaffected.

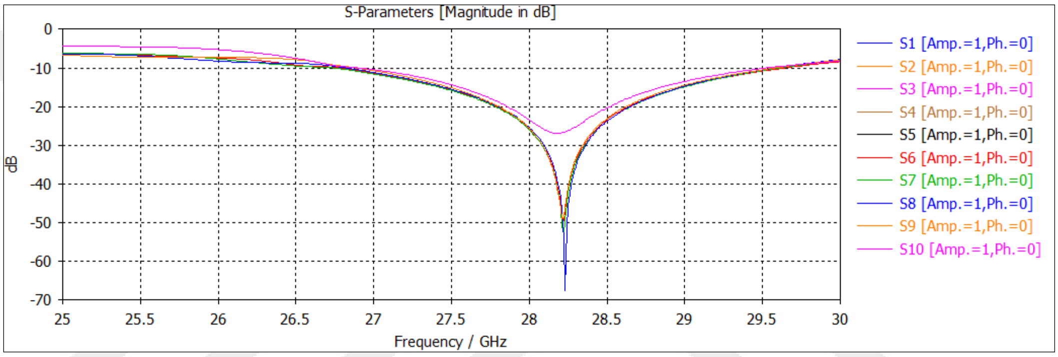

a) S-parameters

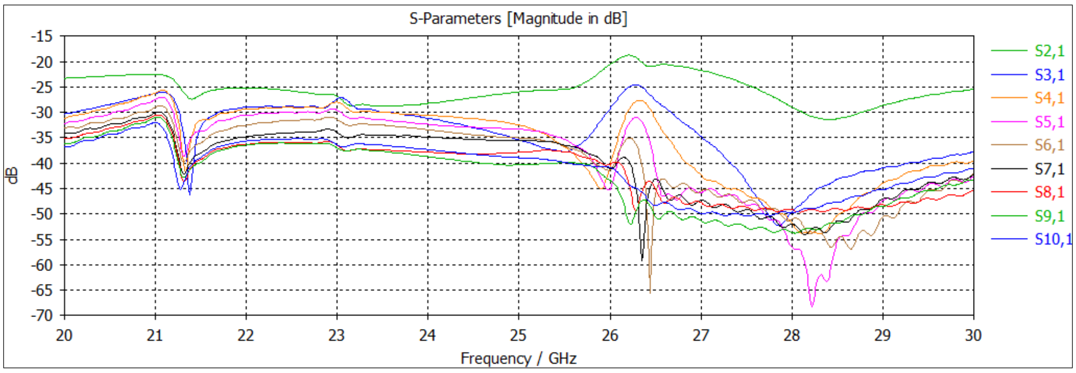

b) Element-to-element isolation

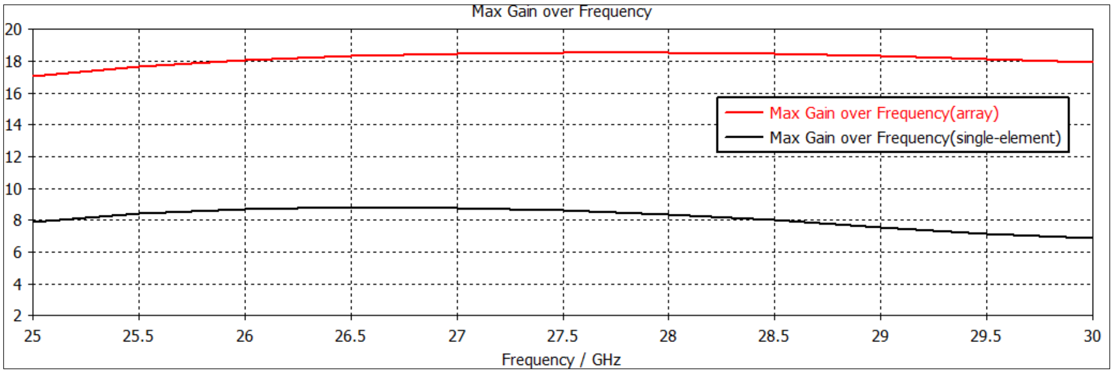

c) Maximum gain

Figure 4.4 1D results of the slotted antenna array.

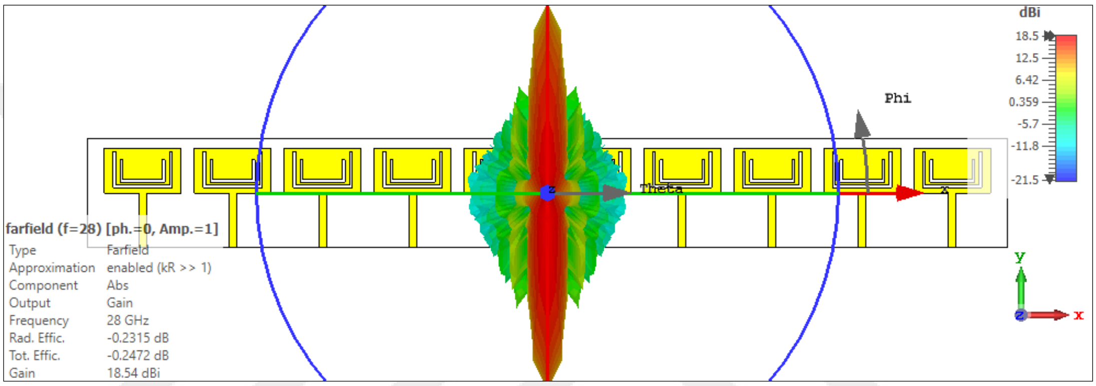

Figure 4.5 3D radiation distribution of the slotted antenna array.

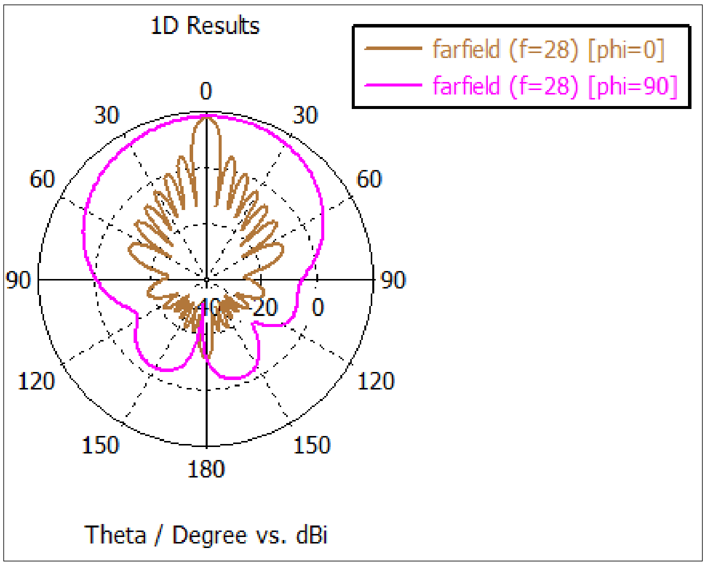

Figure 4.6 1D radiation distribution of the slotted antenna array.

Figure 4.7 presents the 3D beam patterns of the array at various phase angles, with the maximum beam steering obtained at a 180° phase shift. The array was capable of scanning angles in the range from −44° to 44° in the theta plane (ϕ = 0°). Table 4.4 summarizes the steering angles along with four key antenna metrics. These characteristics reached their peak values at broadside direction (main lobe at 0°) on the theta plane (ϕ = 0°), illustrated in Figure 4.5, and gradually decreased as the beam was steered away. This reduction is attributed to the main lobe widening and partially overlapping with side lobes within the visible angular range, as seen in Figure 4.7(a–d). The parameters reached their minimum at a 180° phase shift (Figure 4.7(d)) before starting to rise again.

Despite the decline in far-field radiation metrics during steering, the array continued to achieve its maximum beam scanning direction, attaining a gain of 14.8 dBi in the (θ) plane (ϕ = 0°), as shown in Figure 4.7(d) and Table 4.4. The array sustained satisfactory gain values at 28 GHz, ranging from 14.8 to 18.5 dBi, representing a loss of 3.7 dB. Directivity spanned values between 15.1 and 18.8 dBi, while the realized gain varied between 14.7 and 18.5 dBi, as detailed in Table 4.4. Furthermore, Figure 4.7 and Table 4.4 indicate that the radiation efficiency remained between 94% and 95% across the scanned angles, whereas overall antenna efficiency ranged from 91% to 95%.

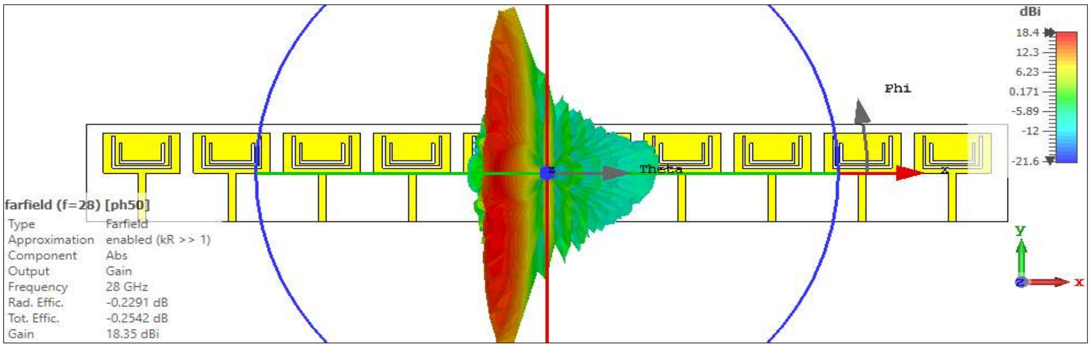

a) $\beta_0 = 50°, \theta_0 = 11°$

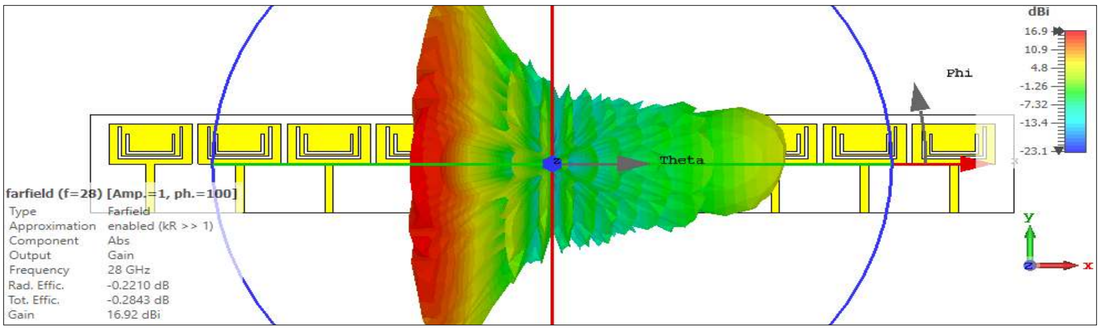

b) $\beta_0 = 100°, \theta_0 = 23°$

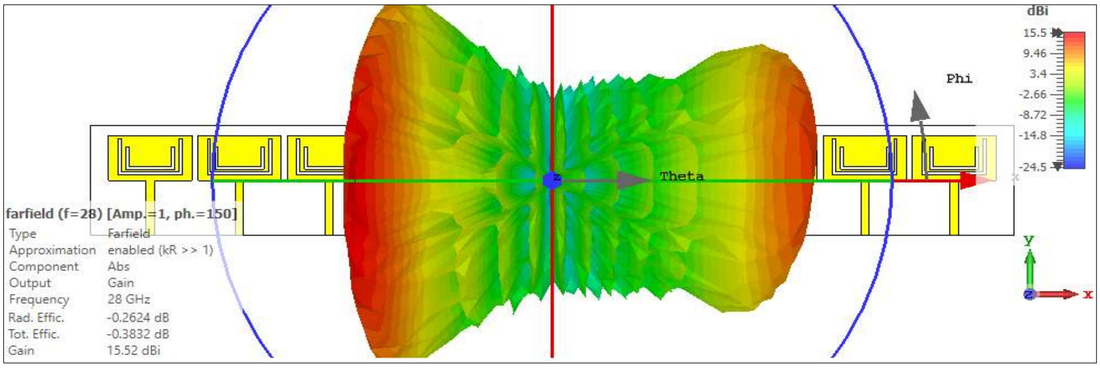

c) $\beta_0 = 150°$, $\theta_0 = 36°$

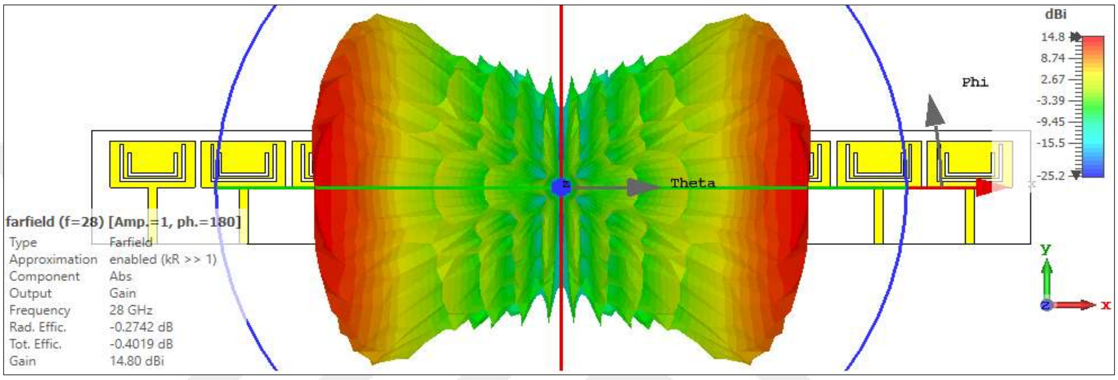

d) $\beta_0 = 180°$, $\theta_0 = 44°$

Figure 4.7 3D beam patterns of the slotted array antenna at 28 GHz for different phase shifts.

Table 4.4 Investigation of beam steering in the slotted array antenna

β_0 (deg)	θ_0 (deg)	G (dBi)	D (dBi)	RG (dBi)	η_{rad}, η_{total} (%)
0	0	18.5	18.8	18.5	95, 95
±50	±11	18.4	18.6	18.3	95, 94
±100	±23	17.3	17.5	17.1	95, 94
±150	±36	15.5	15.8	15.4	94, 92
±180	±44	14.8	15.1	14.7	94, 91

4.3.2 Parasitic Array Antenna

The proposed parasitic array antenna was evaluated in terms of gain, radiation pattern, and S-parameters. As shown in Figure 4.8(a), the S-parameters (S11–S81) indicate a 2.8 GHz bandwidth, covering the 5G frequency range of 27.5–28.35 GHz. Inter-element isolation was examined to assess beam steering feasibility. The array resonates at 28 GHz with mutual coupling below –23.5 dB, confirming its suitability for beam steering. Furthermore, as illustrated in Figure 4.8(b), the parasitic array enhances the antenna performance at 28 GHz by increasing the gain value from 7.8 dBi to 15.2 dBi.

Figure 4.9 presents the 3D far-field radiation pattern, showing a well-focused main beam arising from the combined response of the radiating elements. The presented array achieves a peak radiation at 32° with a gain of 15.2 dBi, an angular beamwidth of 55.6°, and a side-lobe level of –14.9 dB at ϕ = 90°, as illustrated in Figure 4.10. In contrast, at ϕ = 0°, it radiates at 0° with a –13.2 dB side-lobe level and an angular beamwidth of 10.9°.

To extend angular coverage at ϕ = 0°, beam steering was implemented. As depicted in Figure 4.11, a ±180° phase shift allows the main beam to be steered over –58° to +58°. The parasitic array achieves its highest gain at 0° phase shift, as shown in Figure 4.9. During beam steering, its gain ranges from 15.2 dBi to 9.6 dBi, corresponding to a loss of 5.6 dB, which is greater than the 3.7 dB obtained by the slotted array. At the maximum steering angle of 58°, the parasitic array produces a gain of 9.6 dBi, which is below the 12 dBi minimum required for 5G applications. Overall, the comparative analysis of both proposed phased arrays indicates that the parasitic array achieves a wider beam-steering range, whereas the slotted array sustains a higher and more stable gain. This observation underscores the inherent trade-off between beam-steering capability and gain stability in phased array design.

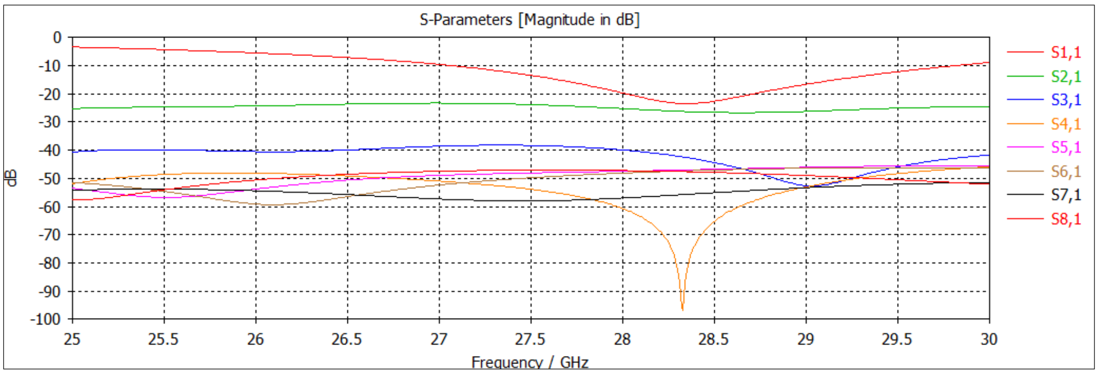

a) S-parameters

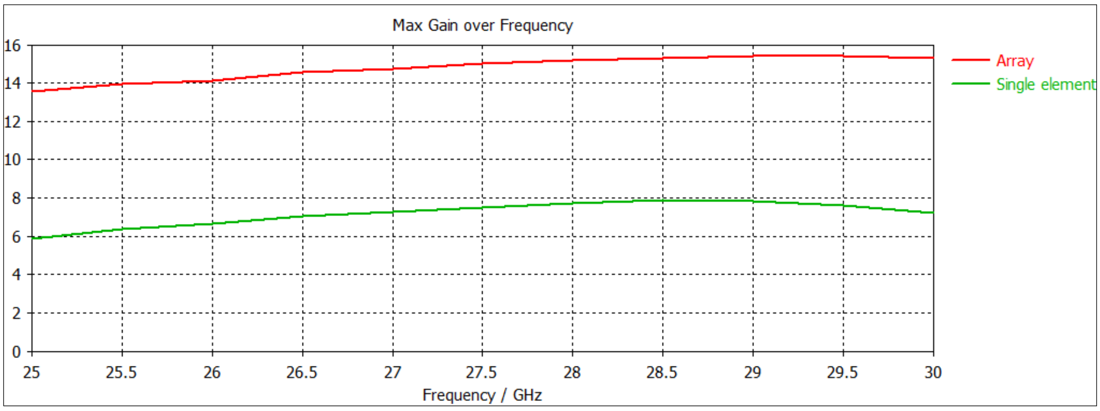

b) Maximum gain verses frequency

Figure 4.8 1D simulation results of the parasitic antenna array.

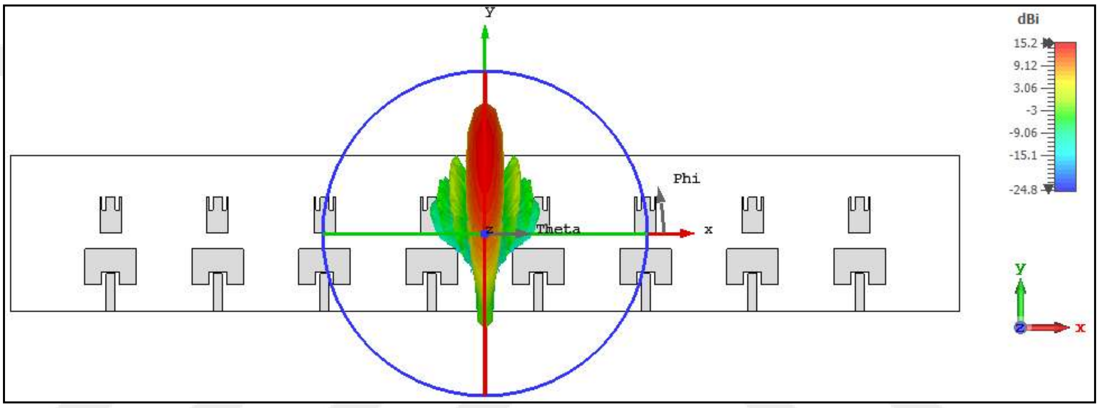

Figure 4.9 3D beam pattern of the parasitic array antenna.

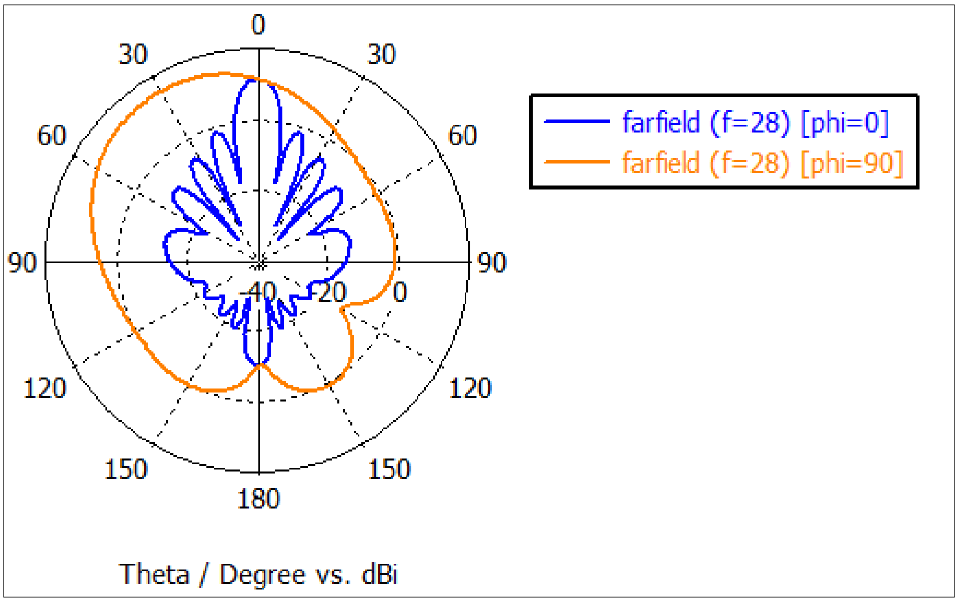

Figure 4.10 1D beam pattern of the parasitic array antenna.

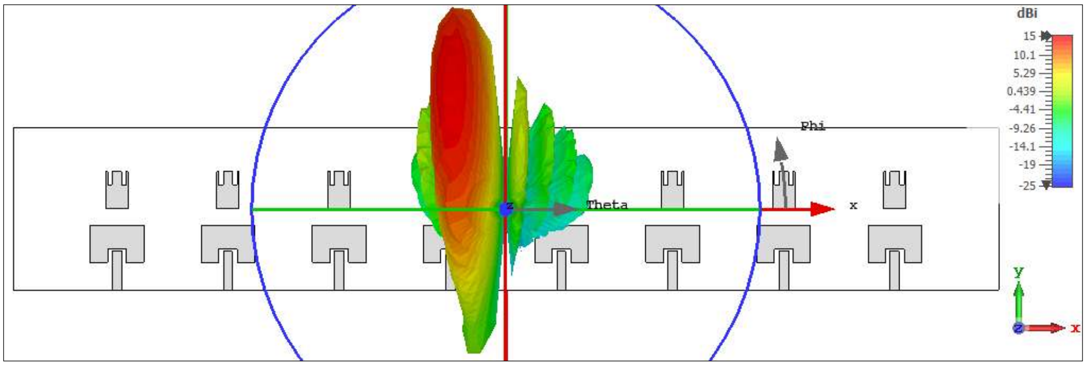

a) $\beta_0 = 45°$, $\theta_0 = 13°$

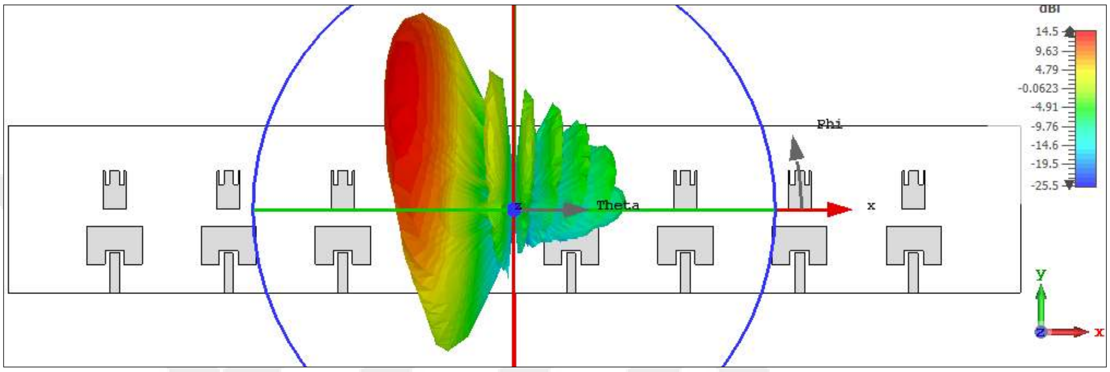

b) $\beta_0 = 90°$, $\theta_0 = 26°$

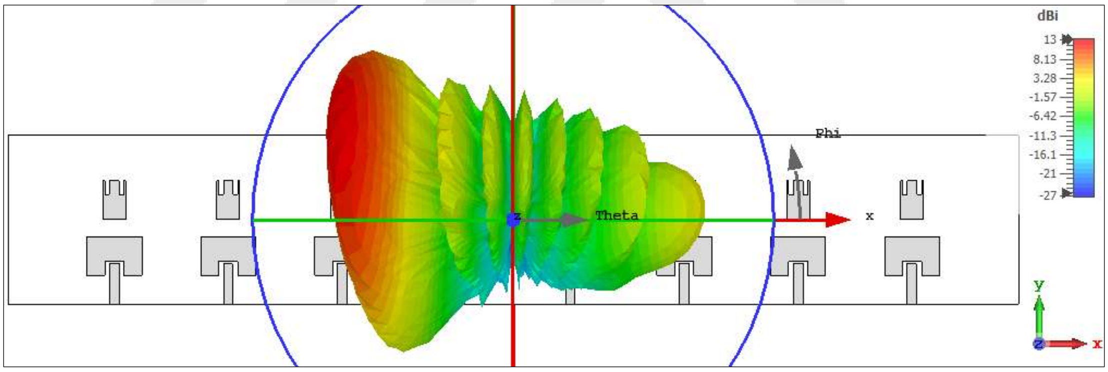

c) $\beta_0 = 140°$, $\theta_0 = 42°$

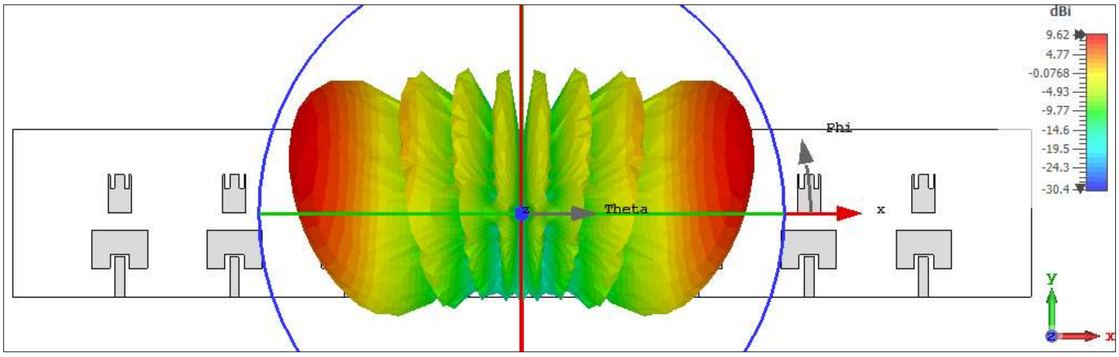

d) $\beta_0 = 180°$, $\theta_0 = 58°$

Figure 4.11 3D beam patterns of the parasitic antenna array at 28 GHz for various phase shifts.

4.3.3 Impact of Windowing-Based Tapering on the Best-Performing Array

After evaluating the performance of both the slotted and parasitic arrays, the slotted array demonstrated a higher gain response and consistently satisfied the gain requirements even under beam steering, making it more suitable for 5G applications. To further enhance the radiation characteristics, particularly by reducing sidelobe levels, amplitude tapering windows were applied.

Ten amplitude tapering techniques were investigated, with the corresponding coefficients summarized in Table 4.5, where only the first five elements are listed since the remaining elements follow a symmetrical distribution. The array's performance under these windows was analyzed at $\phi = 0°$ to evaluate sidelobe suppression and its impact on gain and beamwidth, as illustrated in Figure 4.12(a–j). Among the tested methods, the window demonstrating superior gain was selected for beam-steering applications to ensure both effective sidelobe reduction and adequate gain.

The results show that the Hamming window reduced the SLL to –29.2 dB, with gain decreasing from 18.5 dBi to 16.5 dBi and beamwidth widening from 7° to 11.3°. The Hanning window achieved a similar SLL reduction but caused a slightly larger gain loss of 2.5 dBi and increased the beamwidth to 13°. The Blackman window lowered the gain to 15.3 dBi while achieving an SLL of –29 dB and broadening the beamwidth to 14.8°, whereas the Blackman-Harris window further increased the beamwidth to 17.4°, with a gain of 14.6 dBi and an SLL of –28.9 dB. In comparison, the Bartlett window reduced the SLL to –29.2 dB with gain decreasing to 17 dBi and beamwidth widening to 10°, while the Barthann window reduced the SLL to –15.3 dB but preserved the beamwidth and only slightly lowered the gain from 18.5 dBi to 18 dBi. Thus, the Barthann window provided higher gain than the Bartlett method but at the cost of higher sidelobes. The Chebyshev window produced one of the best trade-offs, achieving an SLL of –29.4 dB with a gain of 17.2 dBi and a beamwidth of 9.8°. Similarly, the Welch window reduced the SLL to –20.6 dB while only slightly decreasing the gain to 17.3 dBi and increasing the beamwidth to 9.5°. The Gaussian window achieved an SLL of –28.2 dB with minimal impact on gain and beamwidth, while the Exponential window provided a gain of 17.7 dBi with an SLL of –21.7 dB and a beamwidth of 8.4°.

Overall, amplitude tapering effectively suppresses sidelobes, although it generally reduces peak gain and broadens the main lobe, highlighting the trade-off between sidelobe reduction and gain depending on the antenna's desired application. Despite this drawback, the array maintains relatively high gain across all methods. When comparing based on gain, the Barthann window achieves the highest gain but provides only limited sidelobe suppression, whereas the Exponential window offers the second-highest gain with moderate sidelobe reduction and minimal impact on beam shape. Conversely, when sidelobe suppression is the main criterion, the Chebyshev window achieves the lowest sidelobe level while maintaining high gain and causing only a slight increase in beamwidth. Thus, both the Exponential and Chebyshev windows are selected for further beam steering investigation.

Table 4.5 Amplitude excitation weighting

Tapering method	**Amp. coef. No. 1**	**Amp. coef. No. 2**	**Amp. coef. No. 3**	**Amp. coef. No. 4**	**Amp. coef. No. 5**
Hanning	0	0.115	0.415	0.75	0.97
Hamming	0.08	0.19	0.46	0.77	0.97
Blackman	0	0.0486	0.26	0.63	0.952
Blackman-harris	0	0	0.15	0.535	0.94
Bartlett	0.1	0.3	0.5	0.7	0.9
Barthann	0.76	0.808	0.856	0.904	0.952
Chebyshev [65]	1	2.086	3.552	4.896	5.707
Welch	0	0.36	0.64	0.84	0.96
Gaussian with σ=0.5	0.1	0.3	0.5	0.7	0.9
Exponential with $\tau = N/2$	0.4	0.4	0.5	0.7	0.8

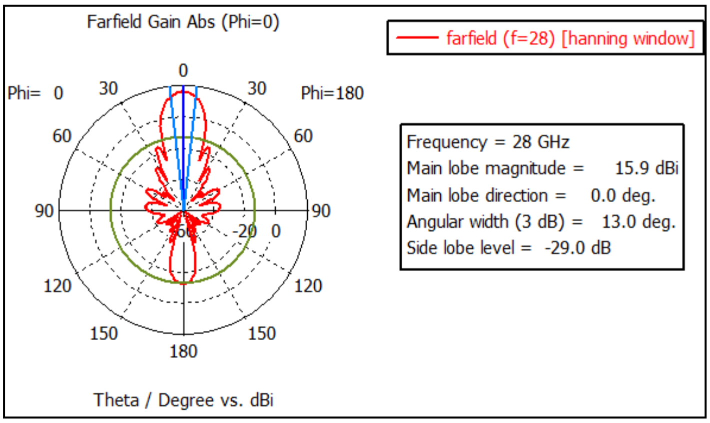

a) Hanning

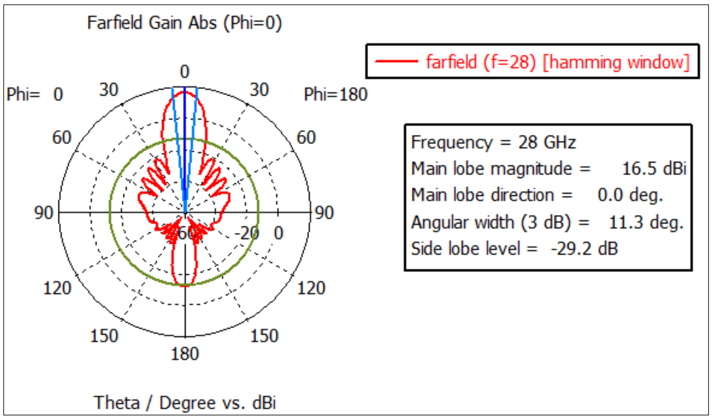

b) Hamming

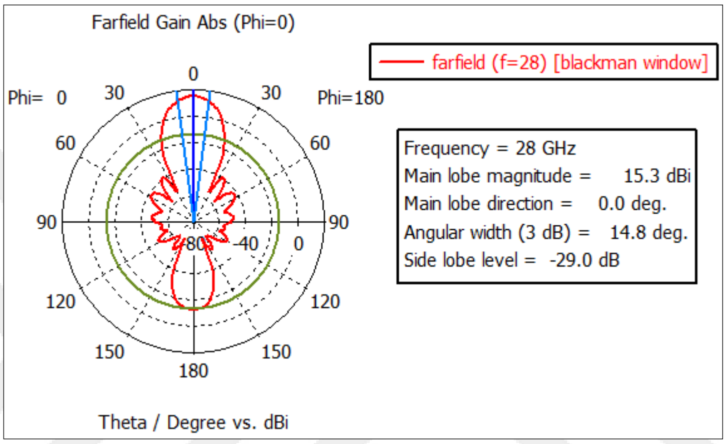

c) Blackman

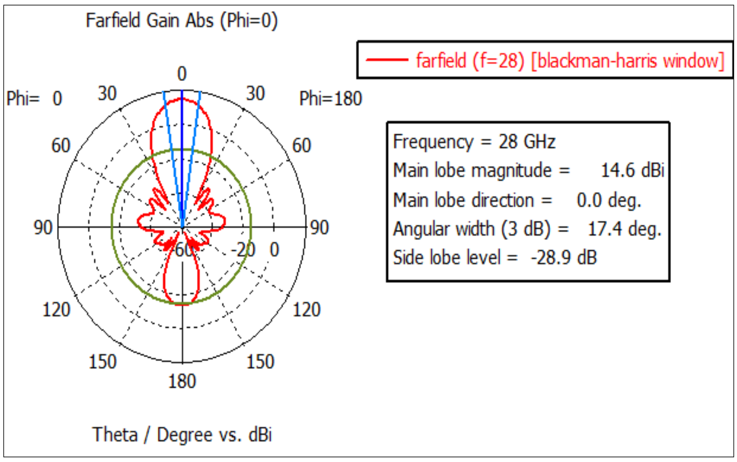

d) Blackman-harris

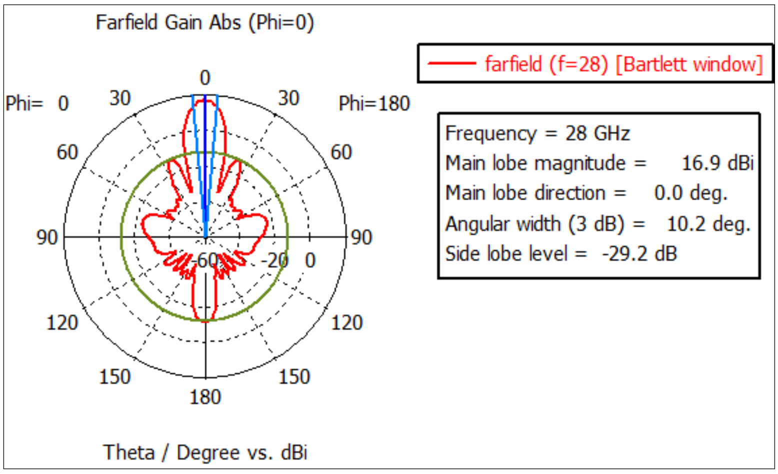

e) Bartlett

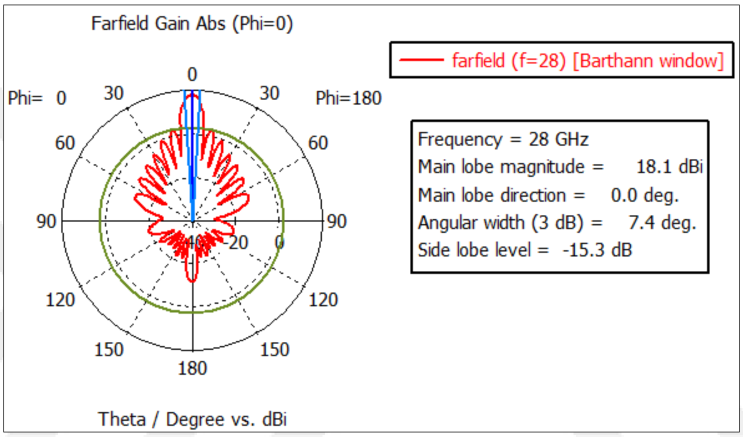

f) Barthann

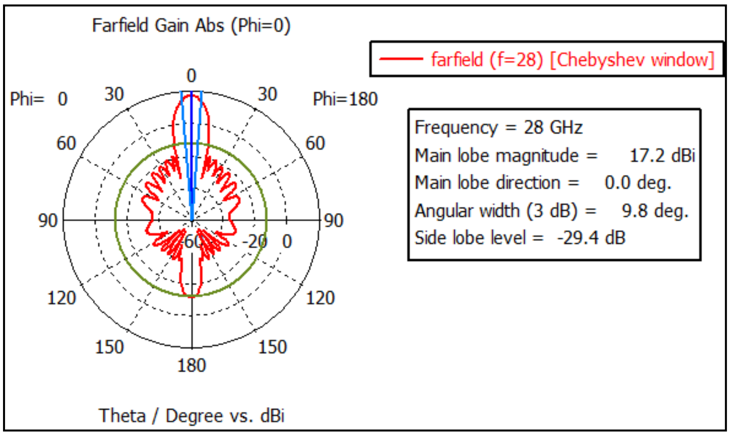

g) Chebyshev

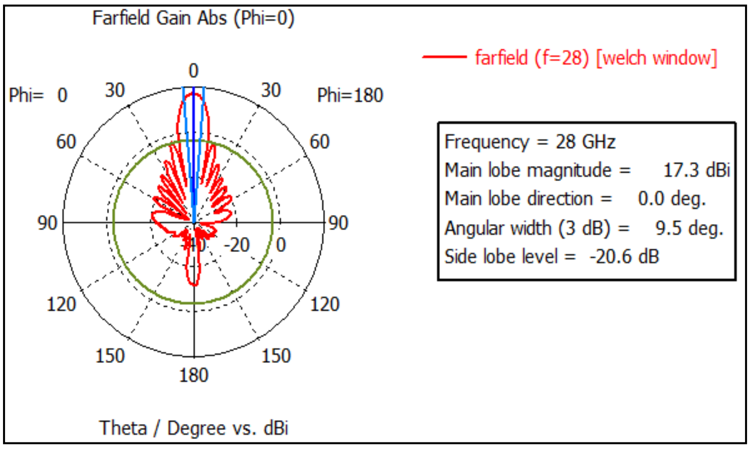

h) Welch

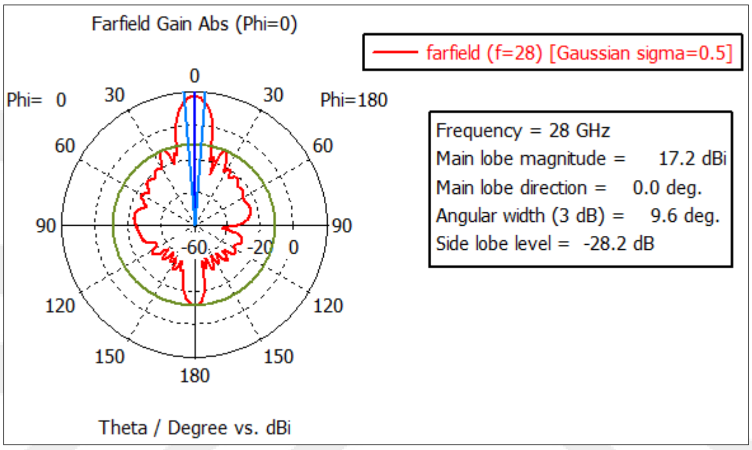

i) Gaussian

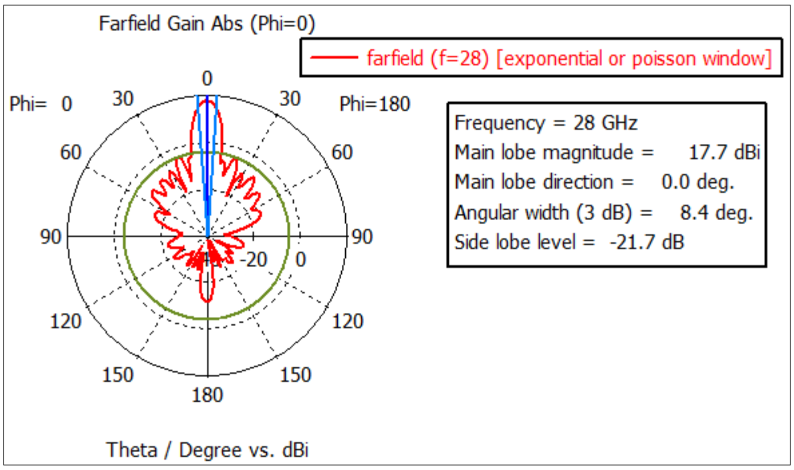

j) Exponential

Figure 4.12 1D beam pattern of the slotted antenna array using tapering windows.

To examine beam-steering performance following side lobe reduction, the Chebyshev and Exponential tapering techniques, selected for their minimal gain drop and low SLL, were analyzed. As shown in Table 4.6, the array employing Chebyshev and Exponential windows exhibits lower SLL levels at 50° and 180° phase shifts compared to the untapered array. Additionally, when evaluating gain during beam steering, the Exponential window achieves slightly higher gain than the Chebyshev window. Although both tapering methods cause some variation in gain, the minimum gain observed with the Chebyshev window still meets the requirements for 5G communication systems. Therefore, either window can be used depending on design priorities: the Exponential window is preferable when maximizing gain is critical, while the Chebyshev window is more suitable when minimizing SLL is the main goal. Furthermore, as illustrated in Figure 4.13, the maximum scanning angle remains unaffected by the tapering methods.

Table 4.6 Beam-steering investigation of the slotted array using the best-performing tapering window

Phase Shift Angle (deg)	Beam Steering Angle(deg)	G(dBi)	SLL (dB)
Without tapering			
±50	±11	18.4	-12.8
±100	±23	17.3	-11.9
±150	±36	15.5	-3
±180	±44	14.8	-10.7
Chebyshev window			
±50	±11	17	-26.8
±100	±23	16.4	-10.5
±150	±36	14.2	-3
±180	±44	13.3	-13.5
Exponential window			
±50	±11	17.6	-20.7
±100	±23	16.9	-11.1
±150	±36	14.8	-3
±180	±44	13.8	-13.9

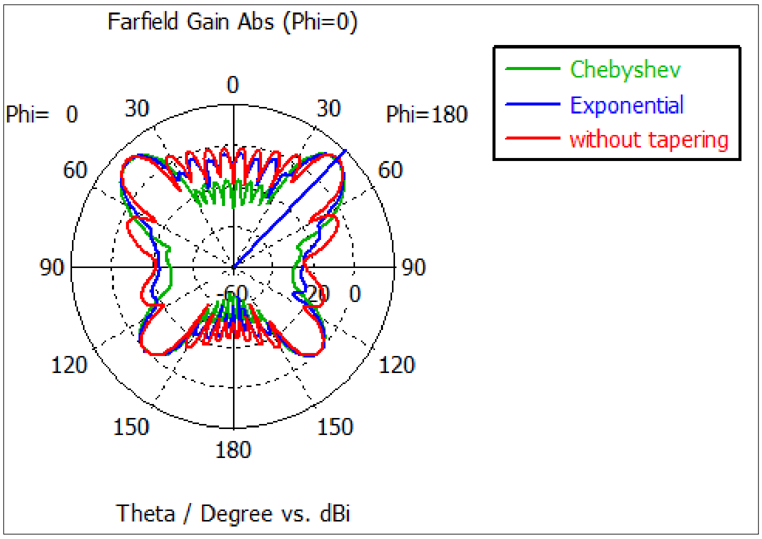

Figure 4.13 Maximum steering angles of the slotted array with and without tapering methods.

4.4 Results Validation

In this section, the simulation results obtained from CST are compared with those from HFSS for both arrays to verify the accuracy and consistency of the modeling approaches.

4.4.1 Slotted Array Antenna

After completing the CST simulation of the slotted array antenna, the design was re-simulated in HFSS to assess the consistency and agreement of the results between the two simulation tools. As shown in Figure 4.14(a), the HFSS simulation achieved a return loss ranging from –26 dB to –39 dB at 28.6 GHz, which is close to the CST results (–27 dB to –67.5 dB at 28.2 GHz). HFSS also provides a –10 dB bandwidth of 2.3 GHz over the frequency range 27.5–29.8 GHz, closely matching the CST result of 2.9 GHz within 26.7–29.6 GHz. Despite these slight variations, the HFSS results confirm that the slotted array still covers the band (27.5–28.35 GHz), consistent with CST. Furthermore, as shown in Figure 4.14(b), the HFSS results demonstrate inter-element isolation below –20 dB, which is comparable to the CST result of isolation below –30 dB. These small discrepancies between CST and HFSS are expected and can be attributed to differences in meshing strategies, solver algorithms, and numerical approximations adopted by each tool.

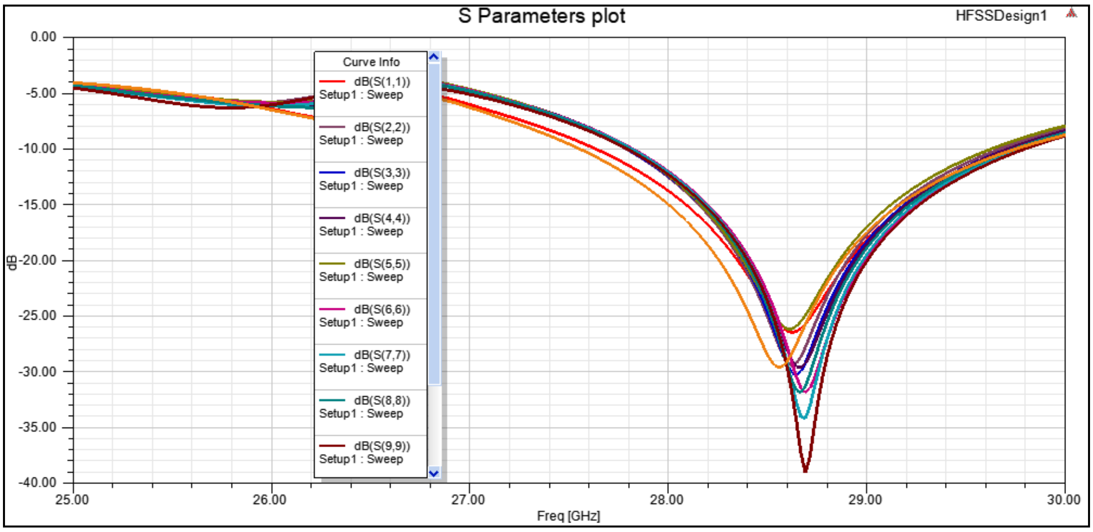

a) S-parameters

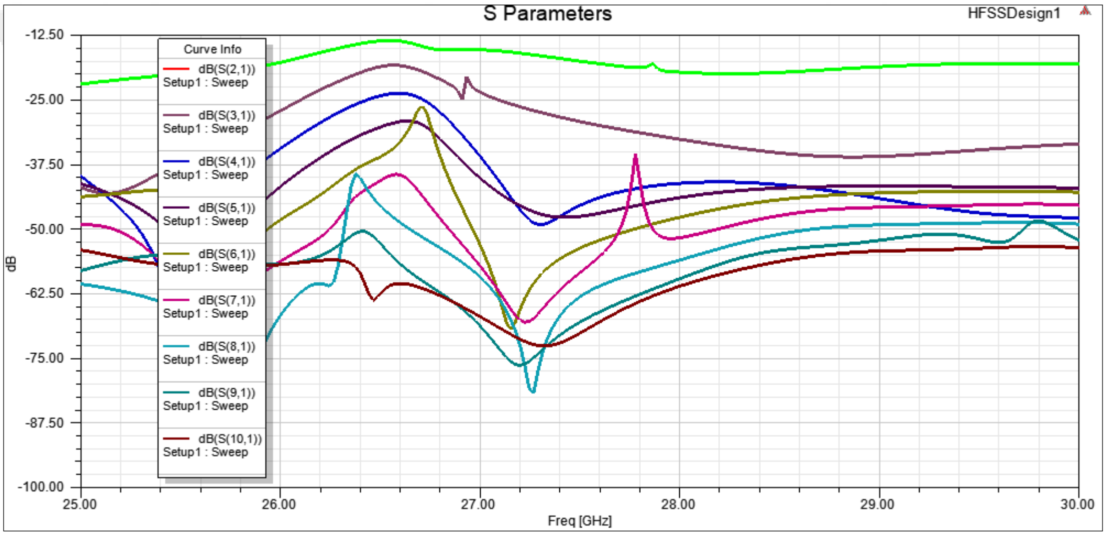

b) Interelement isolation

Figure 4.14 1D results of the slotted array antenna in HFSS.

In HFSS, the slotted array achieved a gain of 18.3 dBi at 28 GHz, as shown in Figure 4.15, which is slightly lower than the CST result of 18.5 dBi. The HFSS simulation also produced an 18.3 dBi directivity value and an 18.2 dBi realized gain value, which are slightly lower than the CST values of 18.8 dBi and 18.5 dBi, respectively. As illustrated in Figure 4.16, at θ (ϕ = 0°), the slotted array radiates at 0°, the same as in CST, with a –13.2 dB side-lobe level, close to the CST value of –13.4 dB, and a beamwidth of 7°, identical to CST. Similarly, at ϕ = 0°, the slotted array radiates at an angle of approximately 4°, the same as in CST, with a beamwidth of 72°, which is slightly larger than the CST result of 68°.

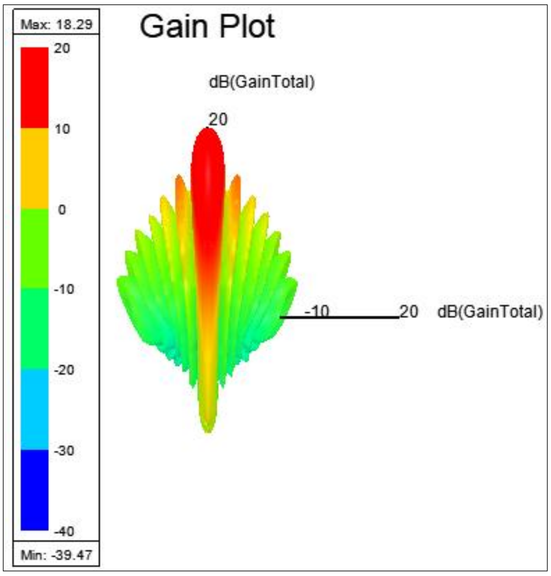

Figure 4.15 HFSS-simulated 3D radiation distribution of the slotted antenna array.

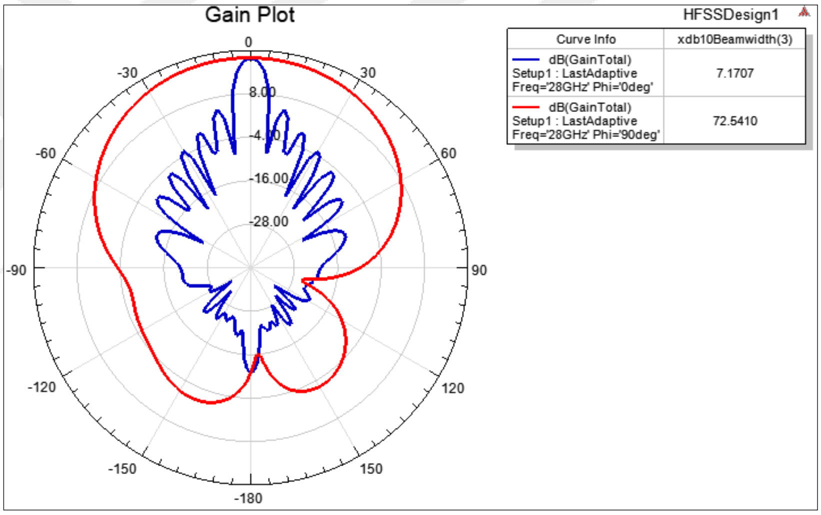

Figure 4.16 HFSS-simulated 1D radiation distribution of the slotted antenna array.

Figure 4.17 presents the HFSS-simulated beam patterns of the array at various phase angles, with the maximum beam steering obtained at a 180° phase shift °, consistent with the CST result. In HFSS, the array was capable of scanning angles from –44° to 44° in the θ direction (ϕ = 0°) with a gain of 14.7 dBi, similar to CST. The proposed array also sustained satisfactory gain values ranging from 14.7 to 18.3 dBi, representing a 3.6 dB loss at 28 GHz, which is very close to the CST result of 14.8–18.5 dBi with a loss of 3.7 dB. The HFSS directivity values varied from 14.8 to 18.3 dBi, which are close to the CST range of 15.1–18.8 dBi, while the realized gain values spanned from 14.2 to 18.2 dBi, comparable to the CST values of 14.7–18.5

dBi. Overall, the beam-steering results in HFSS show strong agreement with those obtained in CST.

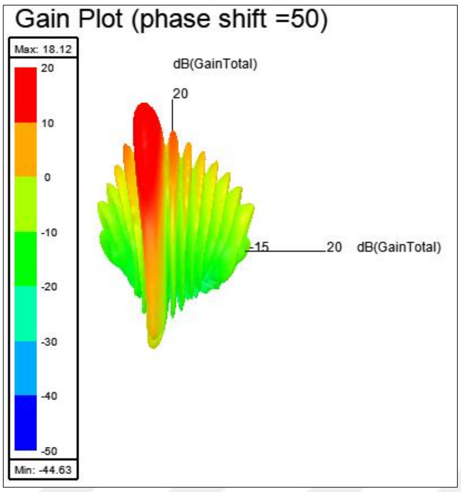

a) $\beta_0 = 50°, \theta_0 = 11°$

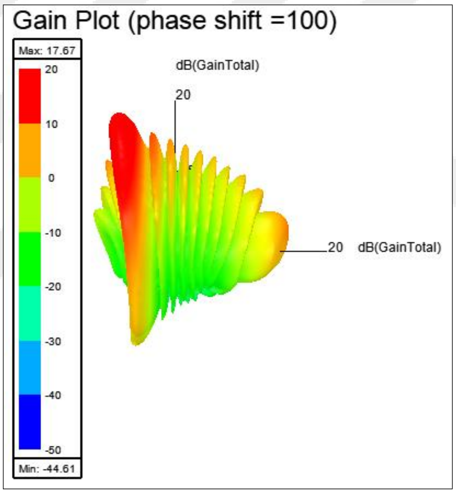

b) $\beta_0 = 100°, \theta_0 = 23°$

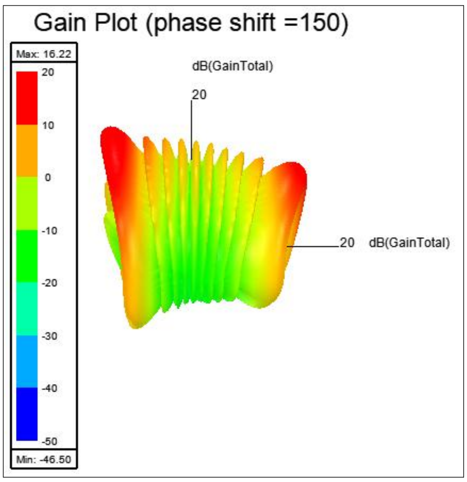

c) $\beta_0 = 150°, \theta_0 = 36°$

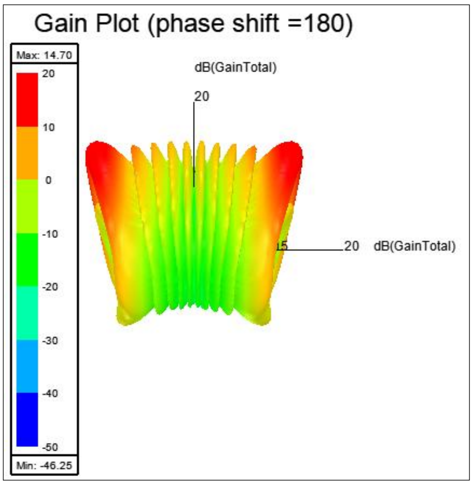

d) $\beta_0 = 180°, \theta_0 = 44°$

Figure 4.17 HFSS-simulated 3D radiation patterns of the slotted array antenna at 28 GHz under different phase shifts.

Since it was established in the previous section (4.3.3) that tapering method was applied to the best-performing array (slotted array), the corresponding amplitude coefficients from Table 4.5 were re-applied in HFSS to facilitate a comparative analysis. The performance was subsequently evaluated in terms of sidelobe suppression and its impact on gain and beamwidth, as illustrated in Figure 4.18(a–j).

The HFSS results show that the Hamming window reduced the SLL to –30.5 dB with a gain of 17.3 dBi and a beamwidth of 8.9°, which is slightly better than the CST results (SLL = –29.2 dB, gain = 16.5 dBi, beamwidth = 11.3°). In contrast, the Hanning window in HFSS produced an SLL of –22.5 dB, higher than the CST value of –29 dB, with a gain of 16.5 dBi (slightly above the CST value of 16 dBi) and a beamwidth of 10.8° (slightly narrower than the CST value of 13°). The Blackman window in HFSS lowered the gain to 16.1 dBi while achieving an SLL of –30.8 dB and broadening the beamwidth to 11.8°, which is better than the CST result that showed a slightly lower gain of 15.3 dBi, an SLL of –29 dB, and a broader beamwidth of 14.8°. Meanwhile, the Blackman–Harris window in HFSS further increased the beamwidth to 14.4°, with a gain of 15.2 dBi and an SLL of –25 dB, whereas CST produced a broader beamwidth of 17.4°, with a slightly lower gain of 14.6 dBi and a lower sidelobe level of –28.9 dB. In HFSS, the Bartlett window reduced the SLL to –23 dB (compared to –29.2 dB in CST), with a gain of 17.5 dBi (higher than the CST value of 17 dBi) and a beamwidth of 8.5° (narrower than the

CST value of 10.2°). The Barthann window in HFSS reduced the SLL to –14.4 dB (slightly higher than the CST value of –15.3 dB) while preserving the beamwidth of 7° (identical to CST) and slightly lowering the gain to 18 dBi (the same as CST). Thus, the Barthann window in HFSS reproduced the CST results almost exactly. The Chebyshev window in HFSS achieved an SLL of –23.4 dB (higher than the CST value of –29.4 dB) with a gain of 17.7 dBi (slightly higher than the CST value of 17.2 dBi) and a beamwidth of 8.3° (slightly narrower than the CST value of 9.8°). Similarly, the Welch window in HFSS reduced the SLL to –17.2 dB (higher than the CST value of –20.6 dB) while only slightly decreasing the gain to 17 dBi (almost the same as CST) and maintaining a beamwidth of 9.6° (identical to CST). The Gaussian window in HFSS achieved an SLL of –23 dB (higher than the CST value of –28.2 dB) with a gain of 17.5 dBi (slightly higher than the CST value of 17.2 dBi) and a beamwidth of 8.5° (slightly narrower than the CST value of 9.6°). Finally, the Exponential window in HFSS provided a gain of 17.9 dBi (almost the same as CST) with an SLL of –18.3 dB (slightly higher than the CST value of –21.7 dB) and a beamwidth of 7.5° (slightly narrower than the CST value of 8.4°). Overall, the Barthann window exhibited the closest agreement between CST and HFSS, whereas the other windows showed slight deviations. These differences can be attributed to variations in the solver algorithms employed by the two platforms. Nevertheless, all tapering methods demonstrated generally good agreement between CST and HFSS, thereby validating the reliability of the comparative analysis.

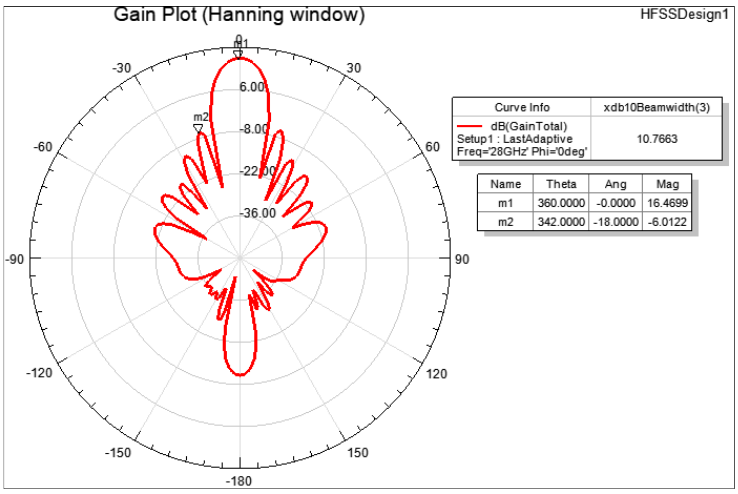

a) Hanning

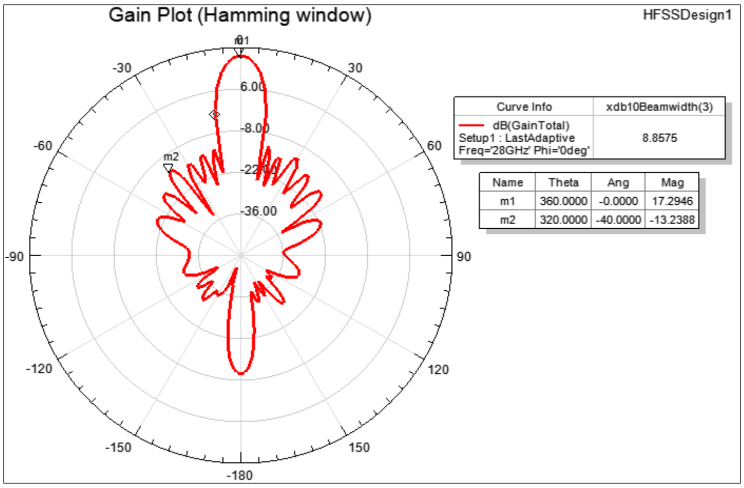

b) Hamming

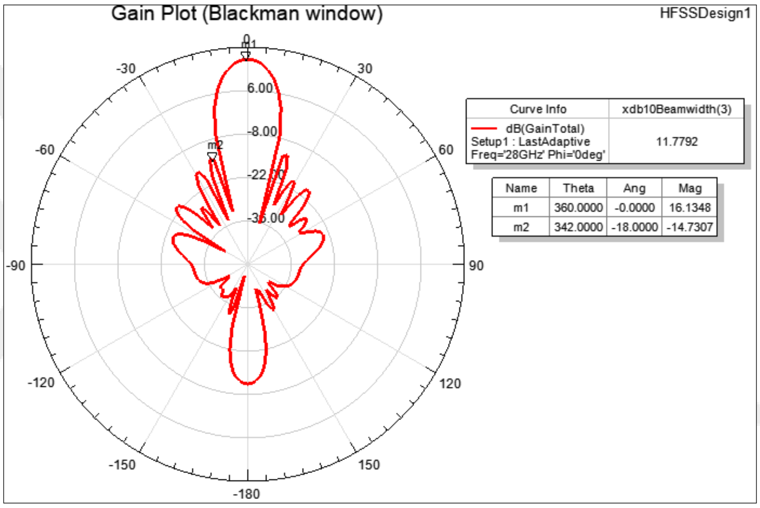

c) Blackman

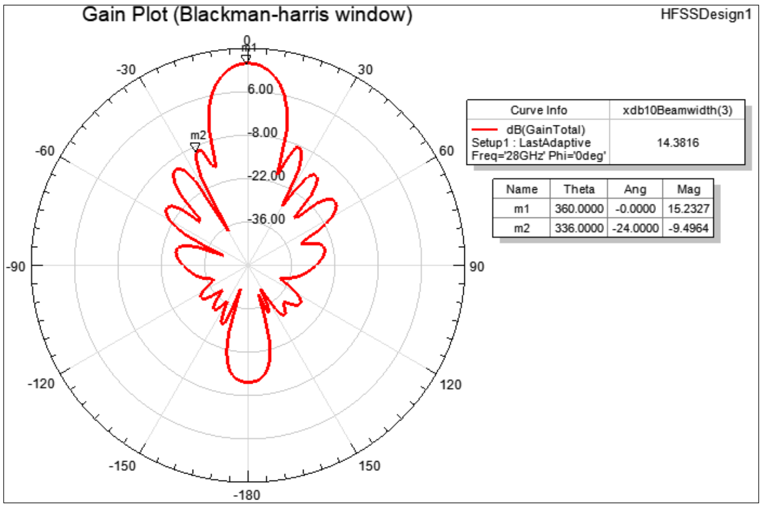

d) Blackman-harris

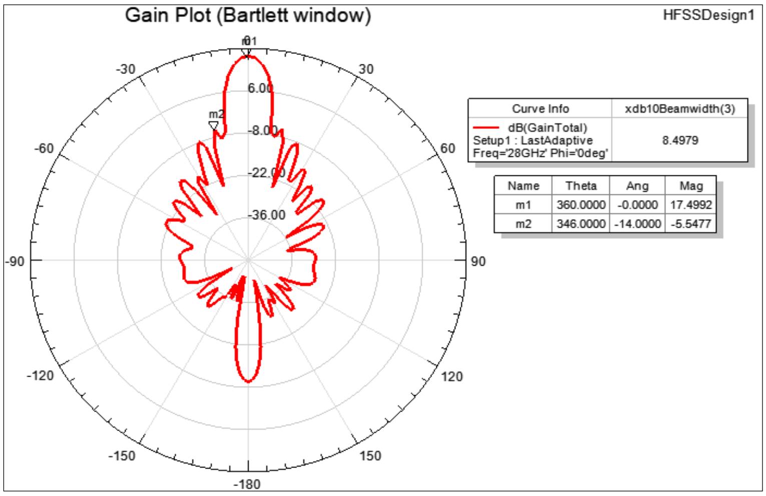

e) Bartlett

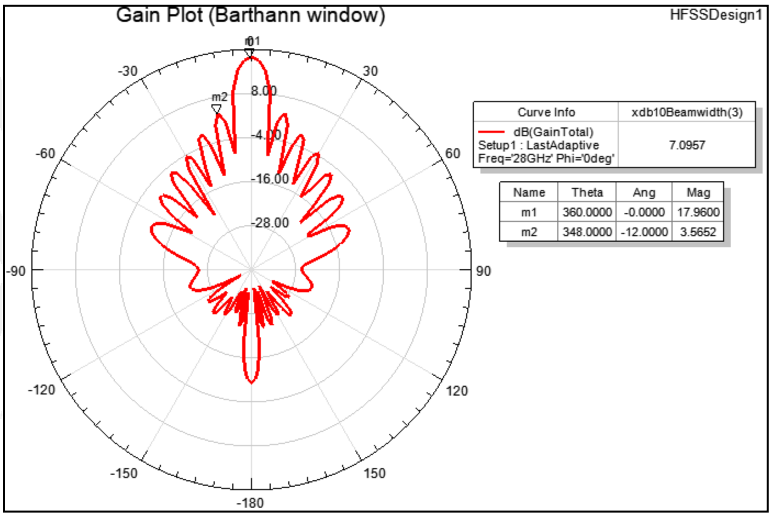

f) Barthann

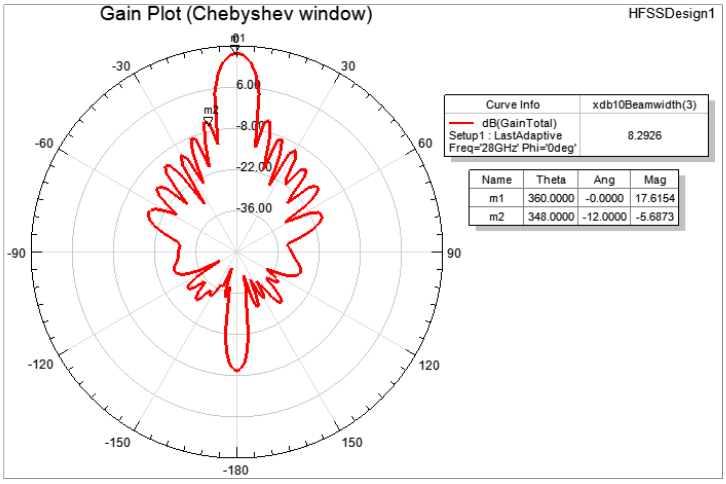

g) Chebyshev

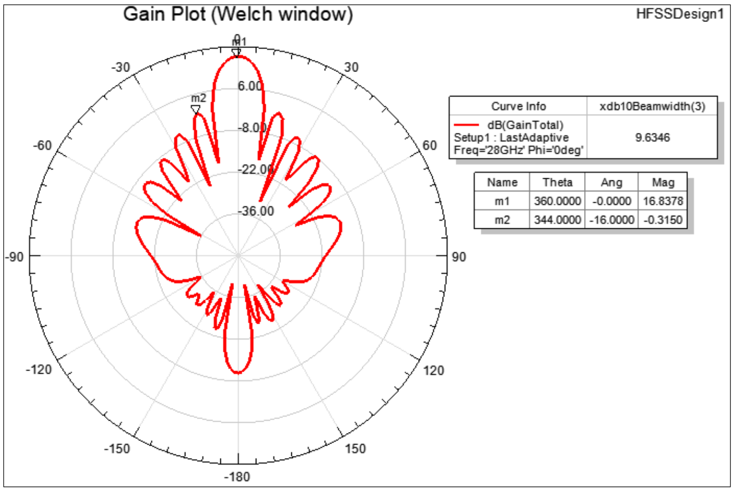

h) Welch

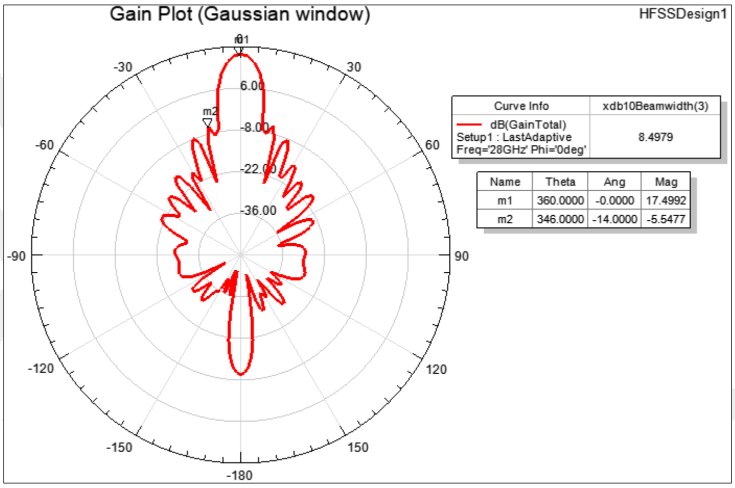

i) Gaussian

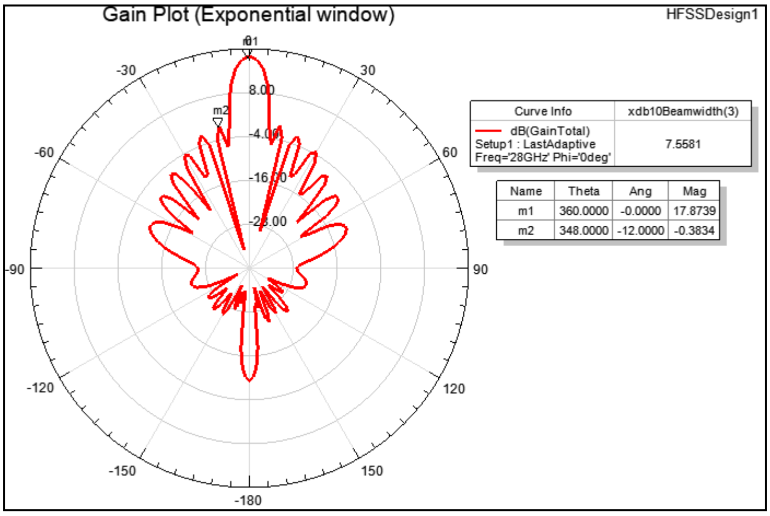

j) Exponential

Figure 4.18 HFSS-simulated 1-D beam pattern of the slotted antenna array using tapering windows.

In CST, the Chebyshev and Exponential windows were selected for beam steering applications, and to ensure a fair comparison, the same cases were also evaluated in HFSS. In HFSS, the slotted array without tapering achieved nearly the same performance as in CST in terms of steering angles, gain, and sidelobe levels (SLL), as summarized in Table 4.7, demonstrating good agreement between the two solvers. With the Chebyshev window, the HFSS array exhibits a slightly higher gain than CST and a slightly lower SLL, except at the phase shift of 50°, where HFSS produces a higher SLL. Similarly, with the Exponential window, the HFSS array achieves marginally higher gain than CST at phase shifts of 150° and 180°, while providing identical gain values at the remaining phase shifts. In this case, the SLL is generally lower in HFSS compared to CST, except again at the 50° phase shift, where HFSS shows a slightly higher value. Although minor variations in gain and SLL are observed between the two tools across the tapering methods, the overall results confirm good consistency. Furthermore, as illustrated in Figure 4.19, the maximum scanning angle in HFSS remains unaffected by tapering, consistent with the CST results.

Table 4.7 Beam-steering investigation of the slotted array using the best-performing tapering window in HFSS

Phase Shift Angle (deg)	**Beam Steering Angle (deg)**	**G (dBi)**	**SLL (dB)**
Without tapering			
±50	±11	17.7	-14
±100	±23	17.1	-12.4
±150	±36	16.2	-4.2
±180	±44	14.7	-10.9
Chebyshev window			
±50	±11	17.4	-20.4
±100	±23	16.9	-13.4
±150	±36	15.9	-4.1
±180	±44	14.5	-18.2
Exponential window			
±50	±11	17.6	-18.6
±100	±23	17.1	-16.7
±150	±36	16.1	-4.1

±180	±44	14.6	-15.3

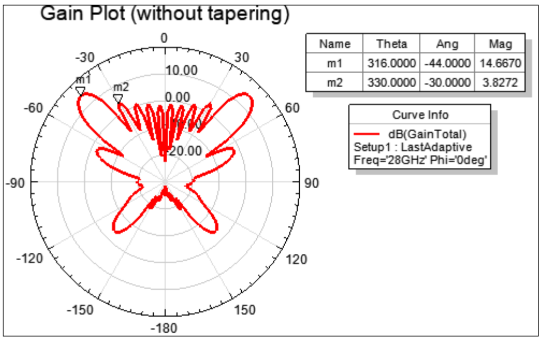

a) Without tapering

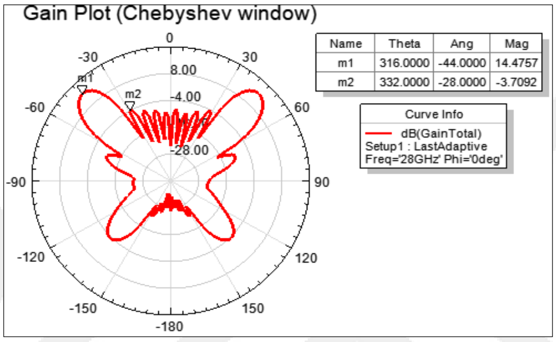

b) Chebyshev window

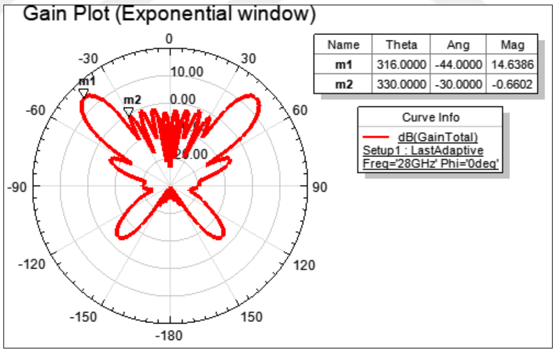

c) Exponential window

Figure 4.19 Maximum steering angles of the slotted array in HFSS with and without tapering methods.

4.4.2 Parasitic Array Antenna

After the CST simulation of the parasitic array antenna in Section 4.3.2, the design was re-simulated in HFSS to confirm the consistency of the results between the two solvers. The HFSS results, shown in Figure 4.20, indicate that the array achieves a 2.8 GHz bandwidth, matching the CST simulation. The resonant frequency occurs at 28 GHz, and the mutual coupling remains below –20.2 dB, closely aligning with the CST value of –23.5 dB.

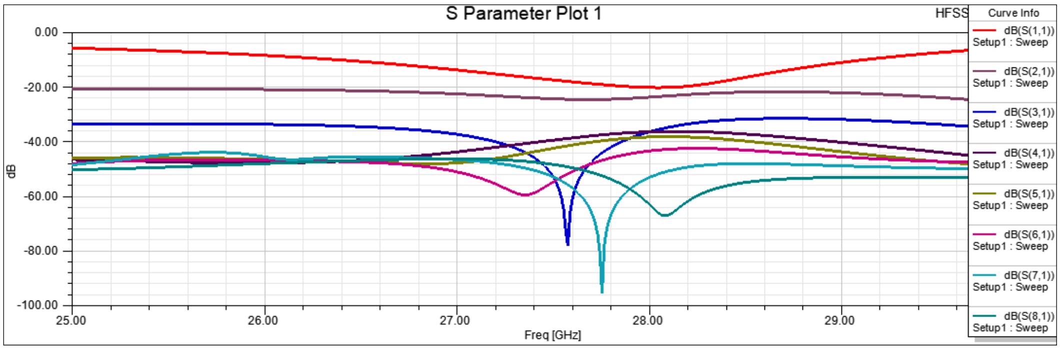

Figure 4.20 S-parameters of the parasitic array antenna in HFSS.

The HFSS-simulated 3D beam pattern of the parasitic array is presented in Figure 4.21. The array exhibits a peak radiation at 32°, identical to the CST result, with a gain of 16.3 dBi, slightly higher than the CST value of 15.3 dBi, and an angular beamwidth of 52.5°, which is close to the CST result of 55.6°, as shown in Figure 4.22 at ϕ = 90°. In contrast, at ϕ = 0°, the array radiates at 0° with SLL of –13.1 dB, matching the CST outcome, and an angular beamwidth of 11.2°, which is nearly equal to the CST value of 10.9°.

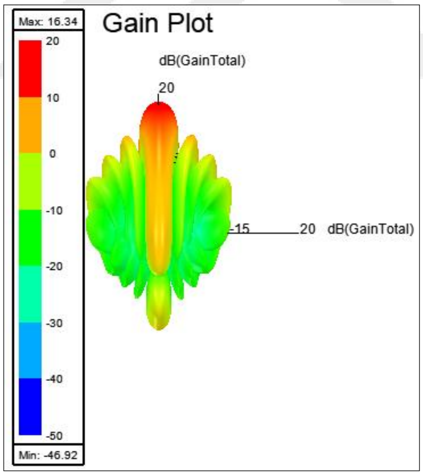

Figure 4.21 3D beam pattern of the parasitic array antenna simulated in HFSS.

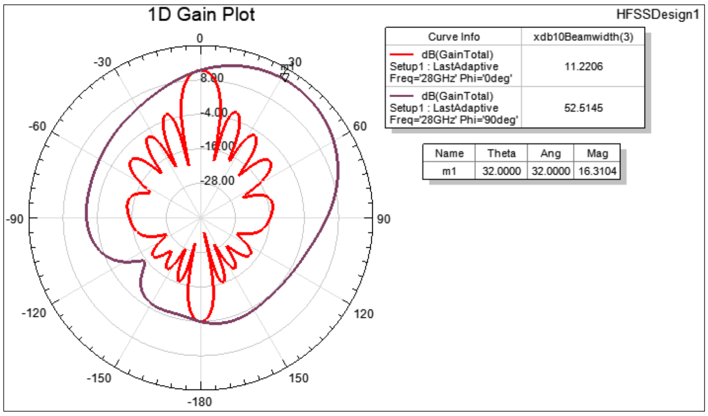

Figure 4.22 1D radiation distribution of the parasitic antenna array simulated in HFSS.

The beam steering performance in HFSS, shown in Figure 4.23, covers an angular range of –58° to +58° with phase shifts of ±180°, consistent with CST results. The parasitic array achieves its maximum gain at a 0° phase shift (Figure 4.21), identical to CST. During beam steering, HFSS gain varies between 16.3 dBi and 10 dBi, slightly higher than CST values, demonstrating overall good agreement between the two simulation tools.

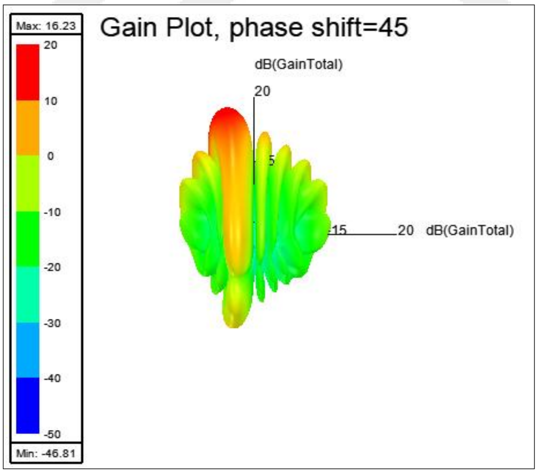

a) $\beta_0 = 45°$, $\theta_0 = 13°$

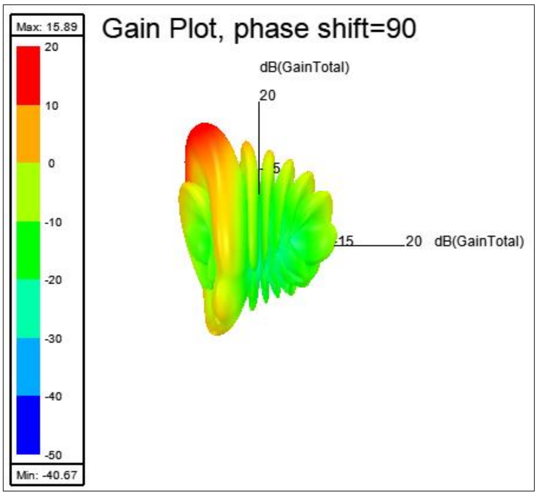

b) $\beta_0 = 90°$, $\theta_0 = 26°$

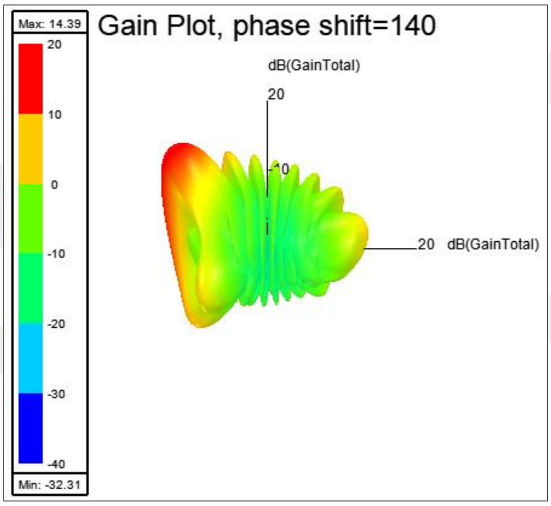

c) $\beta_0 = 140°$, $\theta_0 = 42°$

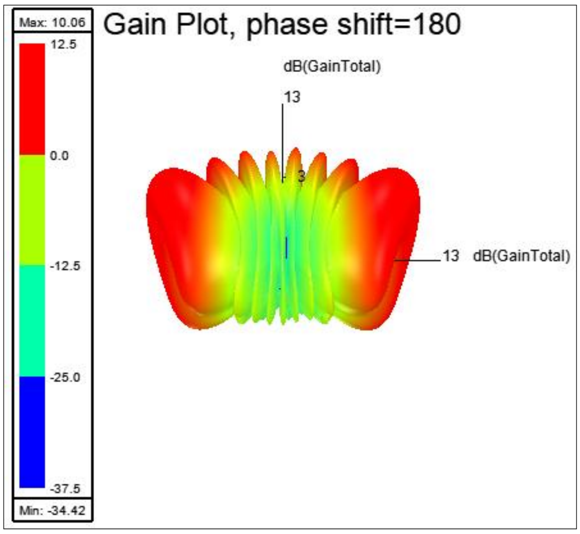

d) $\beta_0 = 180°$, $\theta_0 = 58°$

Figure 4.23 3D beam patterns of the parasitic antenna array at 28 GHz for various phase shifts, simulated in HFSS.

4.5 Comparison with Published Works

To characterize the performance of the proposed slotted antenna array, its key parameters are compared with recently reported 28 GHz linear array designs, as summarized in Table 4.8. The proposed array achieves a peak gain of 17.7 dBi, which is higher than that of most reported designs, including those employing a larger number of elements, demonstrating its superior radiation performance and efficient array configuration. Although the exponential tapering technique caused a minor gain reduction from 18.5 dBi, it effectively suppressed side-lobes, and the array still maintains a high overall gain. The antenna also exhibits a wide steering range of ±44° with a low peak side-lobe level (SLL) of –21.7 dB, achieved using an exponential tapering amplitude distribution, indicating effective beam steering and excellent pattern stability.

The mutual coupling between elements is minimized to –30 dB, confirming outstanding element isolation compared to previous works. In terms of bandwidth, the proposed design attains 3 GHz, which is broader than several of the compared studies, ensuring stable performance across the 28 GHz band. Furthermore, the antenna achieves a high radiation and total efficiency of 95%, outperforming most reported arrays.

Table 4.8 Comparative analysis between the proposed slotted array antenna and recent 28 GHz linear array designs

Ref.	Year	Elements No.	Freq. (GHz)	Freq. Bandwidth (GHz)	Isolation (dB)	Peak G (dBi)	Beam Steering-range	Peak SLL (dB)	G loss (dBi)	Rad. eff., tot. eff. (%)
[8]	2018	12	24–28	4	−21	16.5	±60°	NA	NA	NA,85
[9]	2019	8	28	5.1	−22	11.15	±45°	-13	1.15	NA
[10]	2020	8	28	1.79	−25.02	11.16	±48°	-13	NA	NA
[11]	2020	32	28,38	0.89, 0.99	−35	16.5, 15.35	±45°	NA	NA	NA
[12]	2021	8	28	1	−15	12.5	0°−70°	NA	4.5	90, 90
[14]	2023	8	26, 28, 32, and 36	11	−16	12.5	0°−80°	NA	1.5	95, 80
Proposed	2025	10	28	3	−30	**17.7**	±44°	-21.7	3.9	95,95

4.6 Fabrication

The slotted microstrip phased array antenna was selected for fabrication. The fabrication procedure is summarized as follows. First, a laminated sheet consisting of a copper ground plane, a ROGERS RT-5880 substrate (thickness 0.51 mm), and a copper patch layer was positioned on the LPKF ProtoMat E33 circuit board milling machine, as shown in Figure 4.24. The CircuitPro software was then connected to the LPKF ProtoMat E33 device, as illustrated in Figure 4.25. After the design was loaded and aligned within the software, the milling process was initiated to pattern the top copper layer, as depicted in Figure 4.26. A photograph of the fabricated slotted antenna array is presented in Figure 4.27.

Following milling, the antenna surface was cleaned to remove any remaining debris or imperfections before soldering the SMA connectors to the feed lines. Procuring suitable high-frequency SMA connectors was challenging, as 28 GHz connectors are not commonly available from standard electronic distributors. Therefore, female SMA socket connectors rated up to 26 GHz were used in the fabrication process, as displayed in Figure 4.28. The soldering process is shown in Figure 4.29.

For experimental validation, each port of the array was connected to a PNA-L network analyzer to measure the S-parameters, as shown in Figure 4.30. Due to the limited number of available measurement ports and to simplify calibration at millimeter-wave frequencies, only five elements of the ten-element array were tested. Since all elements are identical and symmetrically placed, the measured S_{11}–S_{55} responses are representative of the entire array. The comparison between the simulated and measured S-parameters (S_{11}–S_{55}) of the slotted array antenna is presented in Figure 4.31. The simulated S-parameters (S_{11}–S_{55}) were calculated using the default excitation settings, without applying amplitude or phase-normalization. The measured return losses are below –10 dB near 28 GHz, confirming good impedance matching and consistent element performance. The results exhibit similar responses across all tested elements, with resonances appearing around 30 GHz and covering the range from 29.5 GHz to 32.5 GHz (S_{11} < –10 dB) with return losses between –11.5 dB and –18 dB. When compared with the simulated results, which show a deeper resonance of approximately −21 to −22 dB at around 28.3–28.4 GHz, the overall return loss trends remain consistent, indicating stable matching and element uniformity in both simulation and measurement. The slight frequency shift between simulated and measured resonances is attributed to practical factors such as SMA connector losses, parasitic effects, milling and soldering tolerances, and measurement setup variations [66-68]. Overall, the fabricated array demonstrated a resonance frequency close to the simulated result, validating the proposed antenna performance despite practical fabrication limitations.

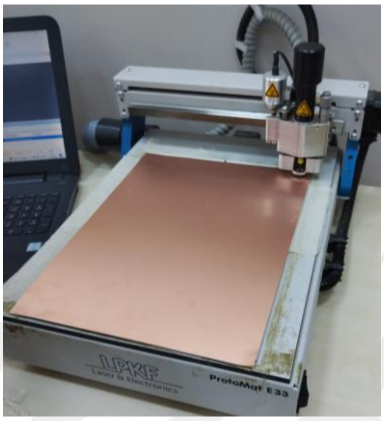

Figure 4.24 First step in the fabrication process, showing the laminated sheet positioned on the LPKF ProtoMat E33 milling machine.

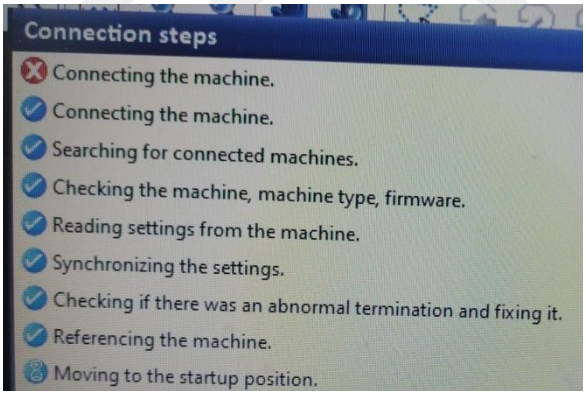

Figure 4.25 Second step in the fabrication process, showing the connection of the CircuitPro software to the LPKF ProtoMat E33 milling machine.

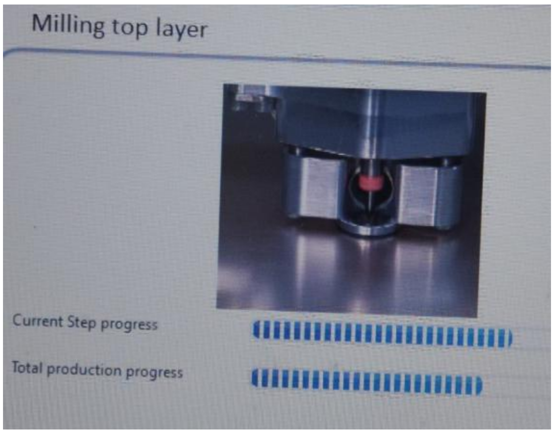

Figure 4.26 Third step in the fabrication process, where the milling order is executed using the LPKF ProtoMat E33 machine.

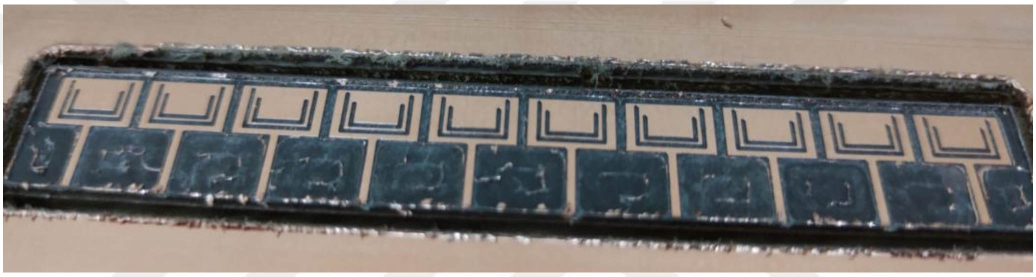

Figure 4.27 The fabricated slotted array antenna after the drilling process.

Figure 4.28 SMA female jack connector selected for the antenna fabrication.

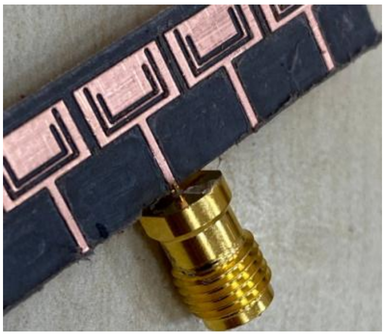

Figure 4.29 Fourth step in the fabrication process, showing the soldering of the SMA connector onto the antenna feed line.

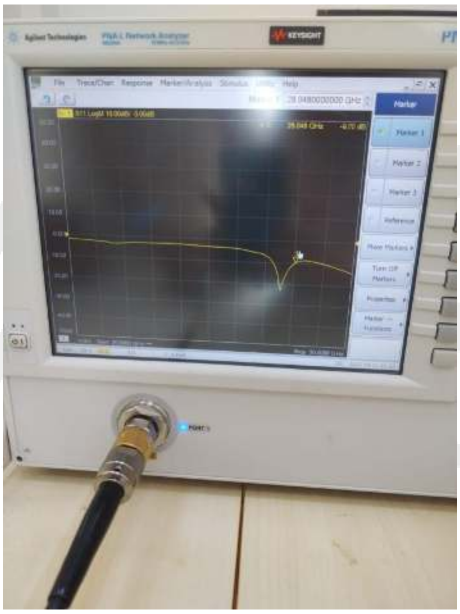

Figure 4.30 Fifth step in the fabrication and testing process, showing the SMA port connection to the PNA-L network analyzer.

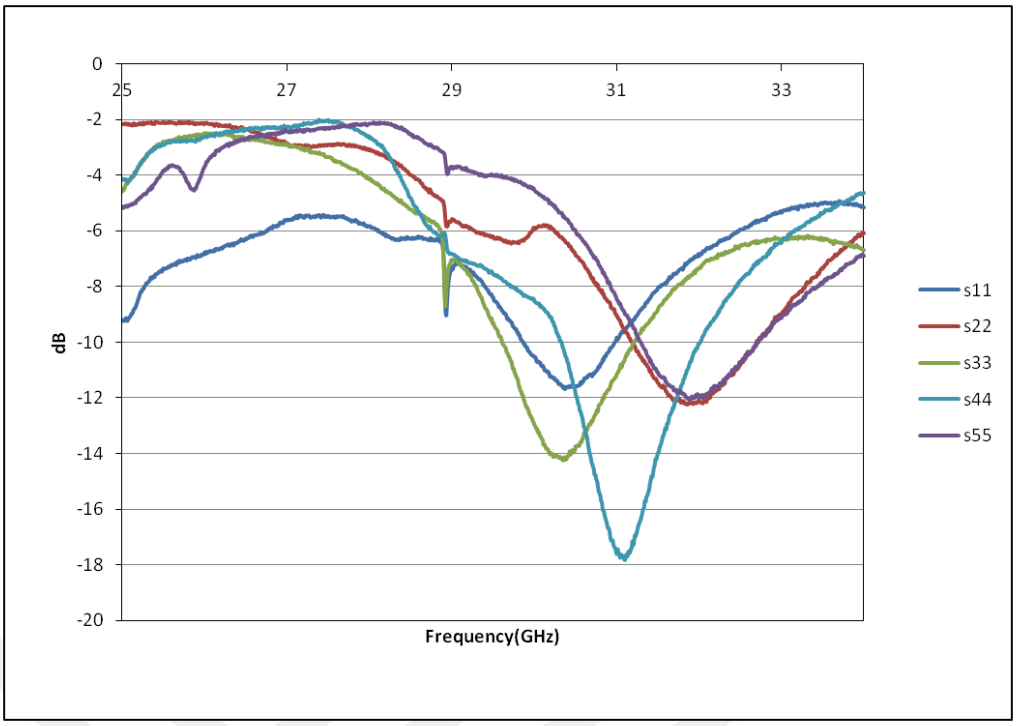

a) Measured

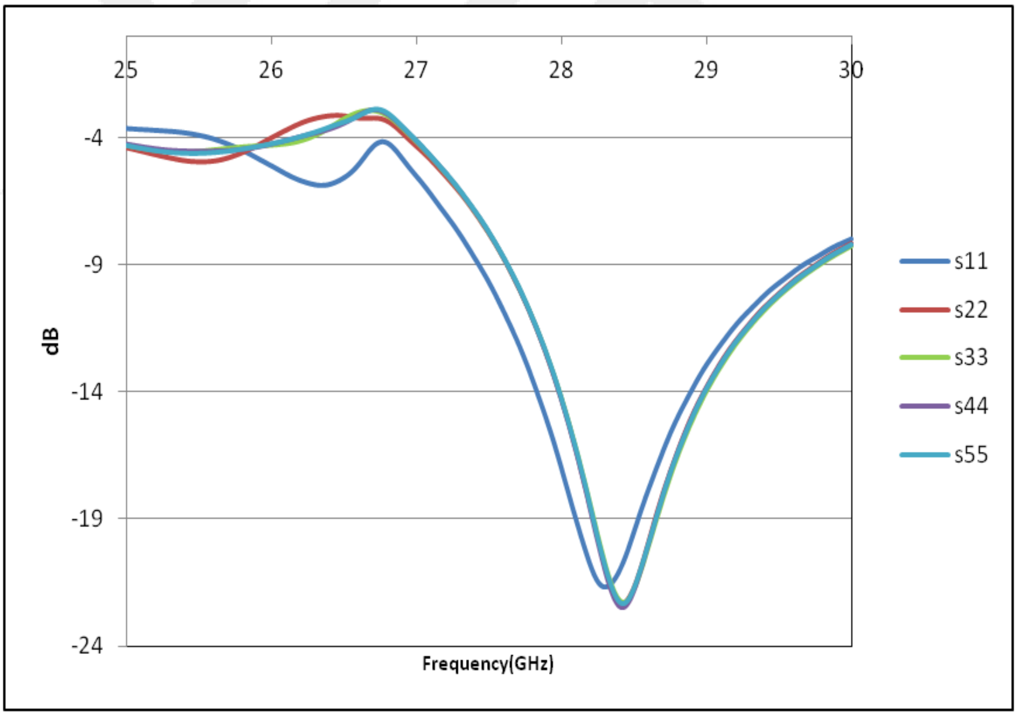

b) Simulated

Figure 4.31 Comparison between the simulated and measured S-parameters (S_{11}–S_{55}) of the slotted array antenna.

CHAPTER 5
SUMMARY OF KEY FINDINGS AND DIRECTIONS FOR FUTURE STUDIES

5.1 Summary of Research Results

The exponential growth of wireless data traffic has accelerated the transition toward the mmWave spectrum and the deployment of 5G communication systems. The mmWave band offers extensive bandwidth, enabling ultra-high data rates; however, it also introduces considerable propagation losses and limited transmission range. To overcome these challenges, high-gain antenna arrays are employed. Nevertheless, their inherently narrow beams restrict angular coverage, thereby reducing system flexibility. Phased array antennas address this limitation by enabling electronic beam steering toward desired directions, ensuring stable and adaptive communication links. Despite their advantages, phased arrays are often affected by high sidelobe levels, which can lead to interference and degraded radiation efficiency. Amplitude tapering techniques are commonly implemented to suppress these sidelobes and enhance the radiation performance. However, a trade-off exists between sidelobe level reduction and antenna gain, which must be carefully optimized according to the performance requirements of the intended application. Consequently, this research focuses on the development and simulation of a high-gain steerable array antenna suitable for 28 GHz 5G communication systems and includes a comparative analysis between two phased array antenna configurations to determine the most effective design for optimal performance. The principal findings and contributions of this work are summarized below:

- As presented in Chapter 3, two single-element patch antennas resonating at 28 GHz were designed and simulated using CST Microwave Studio. Simulation results demonstrated that both configurations achieved good radiation performance. However, the first design, a single slotted patch antenna implemented on an RT/Duroid 5880 substrate, exhibited slightly superior characteristics compared to the second parasitic patch antenna fabricated on an FR4 substrate. Furthermore, the CST simulation outcomes for both designs were validated using HFSS, and the results showed good agreement between the two simulation platforms.

- Chapter 4 presents the design and comparative analysis of two phased array antennas, a 1×10 slotted array and a 1×8 parasitic array, operating at 28 GHz for 5G wireless applications using CST Microwave Studio. Both arrays were subjected to beam steering, with the slotted array achieving a steering range of −44° to +44°, while the parasitic array demonstrated a wider scanning range of −58° to +58°. Despite the narrower beam steering range, the slotted array exhibited a higher peak gain of 18.5 dBi at 28 GHz, with a sidelobe level of −13.4 dB, making it the preferred candidate for further sidelobe reduction enhancement. Ten different windowing functions were evaluated, and since the thesis focuses on achieving high gain, the exponential window was selected as it produced the smallest gain reduction, resulting in 17.7 dBi with achieving a sidelobe level of −21.7 dB. CST simulation results were also compared with HFSS, showing acceptable agreement between the two tools. Additionally, the performance of the optimized slotted array was benchmarked against recently published arrays, demonstrating superior gain, even exceeding designs with more elements. Finally, the best-performing slotted array was fabricated, and measured S-parameters demonstrated a resonance frequency in acceptable agreement with simulation, validating the proposed design even with real-world manufacturing limitations.

5.2 Recommendations for Future Work

Although the proposed phased array antenna demonstrated excellent performance at 28 GHz with high gain, low sidelobe levels, and effective beam steering capability, there remain several potential areas for future improvement and exploration.

- Extended Frequency Band Operation: Future studies may focus on enhancing the bandwidth of the array to support multi-band or wideband operation, enabling compatibility with other 5G and beyond-5G frequency allocations.
- Array Expansion and Optimization: As demonstrated in this thesis, one-dimensional linear phased array configurations were proposed to satisfy the compactness and integration requirements of mobile applications, enabling

beam steering in a single plane. Future research could extend this concept to two-dimensional (planar) array configurations, which would allow 2D-beam steering, thereby enhancing spatial coverage, directivity, and overall system performance.

- Fabrication Enhancements: In this thesis, experimental validation was limited to measuring the return loss of the fabricated array. Future work could extend these measurements to include key performance parameters such as gain, radiation patterns, and beam-steering characteristics. This would provide a more comprehensive verification of the simulated results and further validate the antenna's suitability for practical 5G applications.
- AI-Based Optimization Techniques: The use of machine learning and optimization algorithms may be explored to automatically tune array parameters for optimal gain, sidelobe suppression, and beam-steering accuracy.

REFERENCES

[1] T. S. Rappaport, Y. Xing, G. R. MacCartney, A. F. Molisch, E. Mellios, and J. Zhang, "Overview of millimeter wave communications for fifth-generation (5G) wireless networks, with a focus on propagation models," IEEE Trans. Antennas Propag., vol. 65, no. 12, pp. 6213-6230, Dec. 2017. doi: 10.1109/TAP.2017.2734243.

[2] S. Rangan, T. S. Rappaport, and E. Erkip, "Millimeter-wave cellular wireless networks: Potentials and challenges," Proceedings of the IEEE, vol. 102, no. 3, pp. 366–385, Mar. 2014. doi: 10.1109/JPROC.2014.2299397.

[3] P. Aruna Kumari and I. Santi Prabha, "Signal propagation analysis at 28 GHz and 73 GHz millimeter wave bands for next generation networks," International Journal of Image, Graphics and Signal Processing, vol. 11, no. 8, pp. 19–27, Aug. 2019. https://www.mecs-press.org/ijigsp/ijigsp-v11-n8/IJIGSP-V11-N8-2.pdf.

[4] G. Federico, D. Caratelli, G. Theis, and A. B. Smolders, "A review of antenna array technologies for point-to-point and point-to-multipoint wireless communications at millimeter-wave frequencies," International Journal of Antennas and Propagation, vol. 2021, Article ID 5559765, 2021. doi: 10.1155/2021/5559765.

[5] O. Gassab, A. Azrar, A. Dahimene, S. Bouguerra, and C. He, "Efficient electronic beam steering method in time-modulated linear arrays," IET Microwaves, Antennas & Propagation, vol. 14, no. 5, pp. 402–408, May 2020. doi: 10.1049/iet-map.2019.0673.

[6] A. Bansal, C. Panagamuwa, and W. Whittow, "State-of-the-art millimeter-wave beam-steering antennas for beyond 5G and 6G networks: A comprehensive review," IEEE Antennas and Propagation Magazine, vol. 66, no. 5, pp. 40–51, Aug. 2024. doi: 10.1109/MAP.2024.3441378.

[7] J. Park, S. Y. Lee, Y. Kim, J. Lee, and W. Hong, "Hybrid antenna module concept for 28 GHz 5G beamsteering cellular devices," in 2018 IEEE MTT-S International Microwave Workshop Series on 5G Hardware and System Technologies (IMWS-5G), pp. 1–3, 2018.

[8] M. Stanley, Y. Huang, H. Wang, H. Zhou, A. Alieldin, and S. Joseph, “A capacitive coupled patch antenna array with high gain and wide coverage for 5G smartphone applications,” IEEE Access, vol. 6, pp. 41942-41954, 2018. doi:10.1109/ACCESS.2018.2866058.

[9] H. Lee, S. Kim, and J. Choi, “A 28 GHz 5G phased array antenna with air-hole slots for beam width enhancement,” Applied Sciences, vol. 9, no. 20, p. 4204, 2019. doi: 10.3390/app9204204.

[10] S. Kim and J. Choi, “Quasi-Yagi slotted array antenna with fan-beam characteristics for 28 GHz 5G mobile terminals,” Applied Sciences, vol. 10, no. 21, p. 7686, 2020. doi: 10.3390/app10217686.

[11] M. El Halaoui, L. Canale, A. Asselman, and G. Zissis, “Dual-Band 28/38 GHz Inverted-F array antenna for fifth generation mobile applications,” Proceedings, vol. 63, no. 1, p. 53, 2020. doi: 10.3390/proceedings2020063053.

[12] N. Ojaroudi Parchin, Y. I. A. Al-Yasir, and R. A. Abd-Alhameed, “Phased array 5G antenna design with petal-shaped beams and improved radiation coverage,” in Proc. European Conf. Antennas Propag. (EuCAP), 2021.

[13] N. Ojaroudiparchin, M. Shen, and G. F. Pedersen, “A 28 GHz FR-4 compatible phased array antenna for 5G mobile phone applications,” in Proc. 2015 Int. Symp. Antennas Propag. (ISAP), Hobart, Australia, Nov. 2015, pp. 1-4. doi: 10.1109/ISAP.2015.7447420.

[14] A. S. I. Amar, N. Ojaroudi Parchin, M. Alibakhshikenari, H. El-Hennawy, and M. Darwish, “Wide-scan phased array antenna design for broadband 5G cellular networks,” in Proc. IMAS 2023, Cairo, Egypt, Oct. 2023.

[15] K. N. Raju and A. Kavitha, “Linear phased metamaterial incorporated patch antenna array at 28 GHz for 5G base stations,” C. R. Acad. Bulg. Sci., vol. 77, no. 2, pp. 246–255, Feb. 2024. doi: 10.7546/CRABS.2024.02.10.

[16] L. Zhu, H. Wang, H. Jin, and G. Yang, “A novel high efficiency beam steering array for 5G millimeter-wave communication systems,” Proc. 2018 IEEE Int. Symp. Antennas Propag. (ISAP), Phuket, Thailand, Dec. 2018, pp. 1–3. doi: 10.1109/ISAP.2018.8669874.

[17] Y. Banday, G. M. Rather, and G. R. Begh, “Effect of atmospheric absorption on millimetre wave frequencies for 5G cellular networks,” IET Communications, vol. 13, no. 3, pp. 265–270, 2019. doi: 10.1049/iet-com.2018.5044.

[18] K. Arunruangsirilert, P. Wongprasert, and J. Katto, “Performance analysis of 5G FR2 (mmWave) downlink 256QAM on commercial 5G networks,” arXiv preprint arXiv: 2502.03416, Feb. 2025.

[19] O. Semiari, W. Saad, M. Bennis, and M. Debbah, “Integrated millimeter wave and sub-6 GHz wireless networks: A roadmap for joint mobile broadband and ultra-reliable low-latency communications,” IEEE Wireless Communications, vol. 26, no. 2, pp. 109–115, Apr. 2019. doi: 10.1109/MWC.2019.1800292.

[20] Y. Niu, Y. Li, D. Jin, L. Su, and A. V. Vasilakos, “A survey of millimeter wave (mmWave) communications for 5G: Opportunities and challenges,” Wireless Networks, vol. 21, no. 8, pp. 2657–2676, Nov. 2015. doi: 10.1007/s11276-015-0942-z.

[21] M. R. D. Kodnoeih, Development of Next-Generation 5G Directive Antennas at Millimeter Waves, Ph.D. dissertation, Univ. de Nantes, Nantes, France, 2018.

[22] Z. Zhang, J. Ryu, S. Subramanian, and A. Sampath, “Coverage and channel characteristics of millimeter wave band using ray tracing,” in Proc. IEEE Int. Conf. Commun. (ICC), SAC, Millimeter-Wave Communications, London, U.K., June 2015, pp. 1380–1385.

[23] H. Elmannai, U. Rafique, H. S. Savci, M. U. Tahir, M. Abdullah, A. D. Algarni, and M. Dalarsson, “Four-Element MIMO Patch Antenna With High Gain, High Isolation, and Polarization Diversity Characteristics for 28-GHz Applications,” International Journal of Antennas and Propagation, vol. 2025, Article ID 8878043, 12 pages, Aug. 2025. doi: 10.1155/ijap/8878043.

[24] C. K. Agubor, I. Akwukwuegbu, M. Olubiwe, C. O. Nosiri, A. Ehinomen, A. A. Olukunle, S. O. Okozi, L. Ezema, and B. C. Okeke, “A Comprehensive Review on the Feasibility and Challenges of Millimeter Wave in Emerging 5G Mobile Communication,” Advances in Science, Technology and Engineering Systems Journal, vol. 4, no. 3, pp. 138–144, 2019.

[25] C. E. O. Vargas and L. d. S. Mello, "Measurements of Reflection and Penetration Loss of Construction Materials at 28 GHz and 38 GHz," 2018 IEEE-APS Topical Conference on Antennas and Propagation in Wireless Communications (APWC), Cartagena, Colombia, 2018, pp. 897-900. doi: 10.1109/APWC.2018.8503669.

[26] T. S. Rappaport, S. Sun, R. Mayzus, H. Zhao, Y. Azar, K. Wang, G. N. Wong, J. K. Schulz, M. Samimi, and F. Gutierrez, "Millimeter Wave Mobile

Communications for 5G Cellular: It Will Work!," IEEE Access, vol. 1, pp. 335–349, May 2013. doi: 10.1109/ACCESS.2013.2260813.

[27] A. Morgado, K. M. S. Huq, S. Mumtaz, and J. Rodriguez, "A survey of 5G technologies: regulatory, standardization and industrial perspectives," Digital Communications and Networks, vol. 4, no. 2, pp. 87–97, Apr. 2018. doi: 10.1016/j.dcan.2017.09.010.

[28] D. Gupta, A. Duvey, and S. Agrawal, "A Review: Microstrip Antenna," International Research Journal of Engineering and Technology (IRJET), vol. 6, no. 7, pp. 1238–1241, Jul. 2019. https://www.irjet.net/archives/V6/i7/IRJET-V6I7133.pdf.

[29] M. R. Firaj and M. S. Hussain, "Designing a High Gain Rectangular Microstrip Patch Antenna Working at 3 GHz for RADAR," International Journal of Innovative Science and Research Technology, vol. 9, no. 4, pp. 1967–1971, Apr. 2024. doi: 10.38124/ijisrt/IJISRT24APR1771.

[30] M. B. Hossain, M. S. Hossain, M. M. Hossain, and M. D. Haque, "Optimization of the Feeding Point Location of Rectangular Microstrip Patch Antenna," Advances in Science, Technology and Engineering Systems Journal, vol. 5, no. 1, pp. 382–386, Feb. 2020. doi: 10.25046/aj050149.

[31] M. S. Rana, P. Chakrobortty, S. Pal, M. M. Rahman, A. Sarker, P. Saha, and S. Rahman, "A review on microstrip patch antenna for wireless communication systems at 3.5 GHz," Bulletin of Electrical Engineering and Informatics, vol. 13, no. 4, pp. 2397–2407, Aug. 2024. doi: 10.11591/eei.v13i4.5941.

[32] C. A. Balanis, Antenna Theory: Analysis and Design, 3rd ed. Hoboken, NJ, USA: Wiley, 2005.

[33] K. F. Ahmed, R. H. Abdullah, and D. S. Abdalla, "Design and Simulation of Microstrip Patch Antenna for Wireless Applications," Kurdistan Journal of Applied Research (KJAR), vol. 2, no. 3, pp. 96–104, Aug. 2017. doi: 10.24017/science.2017.3.27.

[34] V. Hanumante and S. Roy, "Comparative Study of Microstrip Patch Antenna Using Different Dielectric Materials," 9th International Conference on Microwaves, Antenna and Remote Sensing (ICMARS), Jodhpur, India, 2013, pp. 56–60. doi: 10.6084/M9.FIGSHARE.1235613.

[35] M. A. Matin and A. I. Sayeed, "A Design Rule for Inset-fed Rectangular Microstrip Patch Antenna," WSEAS Transactions on Communications, vol. 9, no. 1, pp. 63–72, Jan. 2010.

[36] A. S. B. Mohammed, A. R. Yauri, and A. M. Kabir, "Review of Feeding Techniques for Microstrip Patch Antenna," International Journal of Computer Applications, vol. 178, no. 27, pp. 39–43, Jun. 2019. doi: 10.5120/ijca2019919010.

[37] V. Midasala and P. Siddaiah, "Microstrip Patch Antenna Array Design to Improve Better Gains," Procedia Computer Science, vol. 85, pp. 401–409, 2016. doi: 10.1016/j.procs.2016.05.142.

[38] O. Nayat-Ali, O. El Mrabet, M. Aznabet, and F. Z. Khoutar, "Phased array antenna for millimeter-wave application," Proceedings of the Third International Conference on Computing and Wireless Communication Systems (ICCWCS), Kénitra, Morocco, Apr. 24–25, 2019, pp. 1–6. doi: 10.4108/eai.24-4-2019.2284237.

[39] A. Chepala, V. Fusco, U. Naeem, and A. McKernan, "Uniform Linear Antenna Array Beamsteering Based on Phase-Locked Loops," Electronics, vol. 12, no. 4, Art. no. 780, Feb. 2023. doi: 10.3390/electronics12040780.

[40] M. Ridwan, M. Abdo, and E. Jorswieck, "Design of Non-Uniform Antenna Arrays Using Genetic Algorithm," Journal of Wireless Networking and Communications, vol. 2, no. 2, pp. 7–10, 2012. doi: 10.5923/j.jwnc.20120202.02.

[41] P. Khanal and J. Yang, "On Embedded Element Radiation Function and Beam Direction of Wide-Scanning Array Antennas," IEEE Open Journal of Antennas and Propagation, vol. 5, no. 5, pp. 1377–1389, Jun. 28 2024. doi: 10.1109/OJAP.2024.3420764.

[42] W. Ahrens, "Antenna Parameters and Understanding Radiation Pattern," Int. J. Appl. Sci. Res. Rev., vol. 10, no. 3, pp. 26, Jun. 2023. doi: 10.36648/2394-9988-10.3.26.

[43] IEEE Standard for Definitions of Terms for Antennas, IEEE Std 145™-2013 (Revision of IEEE Std 145-1993), Dec. 11, 2013.

[44] C. Carobbi, D. Masiero, and R. Serra, "Measurement of Antenna Efficiency in Reverberation Chambers, Effect of Antenna Positioning and Chamber Loading," in Proc. 4th URSI Atlantic Radio Science Meeting (AT-RASC), Gran Canaria, Spain, 19–24 May 2024. doi: 10.46620/URSIATRASC24/BNNZ7253.

[45] B. Kamo, S. Cakaj, V. Koliçi, and E. Mulla, “Simulation and Measurements of VSWR for Microwave Communication Systems,” International Journal of Communications, Network and System Sciences, vol. 5, no. 11, pp. 767–773, Nov. 2012. doi: 10.4236/ijcns.2012.511080.

[46] T. S. Bird, “Definition and Misuse of Return Loss,” IEEE Antennas and Propagation Magazine, vol. 51, no. 2, pp. 166–167, Apr. 2009. doi: 10.1109/MAP.2009.5162049.

[47] M. Faisal, A. Gafur, S. Z. Rashid, M. O. Shawon, K. I. Hasan and M. B. Billah, "Return Loss and Gain Improvement for 5G Wireless Communication Based on Single Band Microstrip Square Patch Antenna," 2019 1st International Conference on Advances in Science, Engineering and Robotics Technology (ICASERT), Bangladesh, pp. 1-5, 2019. doi: 10.1109/ICASERT.2019.8934474.

[48] R. B. Waterhouse, Microstrip Patch Antennas: A Designer's Guide, 1st ed. New York, NY, USA: Springer Science+Business Media, LLC, 2003.

[49] A. Kumar, A. Kumar, P. J. Soh, and A. Kumar, "Design Consideration, Challenges and Measurement Aspects of 5G mm-Wave Antennas: A Review," Progress In Electromagnetics Research B, vol. 96, pp. 39–66, 2022. doi: 10.2528/PIERB22052002.

[50] D. Subitha, S. Velmurugan, M. V. Lakshmi, P. Poonkuzhali, T. Yuvaraja, and S. Alemayehu, "Development of Rogers RT/Duroid 5880 Substrate-Based MIMO Antenna Array for Automotive Radar Applications," Advances in Materials Science and Engineering, vol. 2022, Article ID 4319549, 11 pages, 2022. doi: 10.1155/2022/4319549.

[51] R. F. Mwang'amba and H. U. Iddi, "28 GHz Patch Antenna Array with Reduced Mutual Coupling for 5G Communications Systems," Tanzania Journal of Engineering and Technology, vol. 41, no. 2, pp. 1–15, 2022. doi: 10.52339/tjet.v41i2.775.

[52] M. Nabil and M. M. A. Faisal, "Design, Simulation and Analysis of a High Gain Small Size Array Antenna for 5G Wireless Communication," Wireless Personal Communications, vol. 116, no. 4, pp. 2761–2776, 2021. doi: 10.1007/s11277-020-07819-9.

[53] A. E. C. Redondi, C. Innamorati, S. Gallucci, S. Fiocchi, and F. Matera, "A Survey on Future Millimeter-Wave Communication Applications," IEEE Access, vol. 12, pp. 133165–133182, 2024. doi: 10.1109/ACCESS.2024.3438625.

[54] B. G. P. Shariff, T. Ali, P. R. Mane, and P. Kumar, "Array Antennas for mmWave Applications: A Comprehensive Review," IEEE Access, vol. 10, pp. 126728–126766, 2022. doi: 10.1109/ACCESS.2022.3226272.

[55] M. S. Yahya, S. Soeung, S. K. Abdul Rahim, U. Musa, S. S. Ba Hashwan, Z. Yunusa, and S. A. Hamzah, “LoRa Microstrip Patch Antenna: A Comprehensive Review,” Alexandria Engineering Journal, vol. 103, pp. 197-221, 2024. doi: 10.1016/j.aej.2024.06.017.

[56] P. Nandi and J. S. Roy, “Optimization of Sidelobe Level of Thinned Phased Array Antenna using Genetic Algorithm and Particle Swarm Optimization,” in Proc. IEEE International WIE Conference in Electrical and Computer Engineering (WIECONECE 2015), Bangladesh, 19-20 Dec. 2015, pp. 27-30.

[57] S. V. R. Rao, A. Mallikarjuna Prasad, and Ch. Santhi Rani, "Antenna Array Weight Synthesis for Low Side Lobe Levels using Window Functions," International Journal of Engineering and Advanced Technology (IJEAT), vol. 9, no. 1, pp. 3074–3080, Oct. 2019. doi: 10.35940/ijeat.A1664.109119.

[58] L. Sarika, P. Nandini, S. Bharathi, Y. D. Lakshmi, and S. Suresh, "Sidelobe Rejection in a Uniform Linear Array Antenna Using Windowing Techniques," International Journal of Research in Engineering and Technology (IJRET), vol. 3, no. 4, pp. 46–50, May 2014.

[59] H. A. Diawuo, S. J. Lee, and Y.-B. Jung, "Sidelobe-level reduction of a linear array using two amplitude tapering techniques," IET Microwaves, Antennas & Propagation, vol. 11, no. 10, pp. 1432–1437, 2017. doi: 10.1049/iet-map.2016.0883.

[60] N. M. Nor, M. H. Jamaluddin, M. R. Kamarudin, and M. Khalily, "Rectangular Dielectric Resonator Antenna Array for 28 GHz Applications," Progress In Electromagnetics Research C, vol. 63, pp. 53–61, 2016. doi: 10.2528/PIERC16022902.

[61] Y. Rahayu, L. Afif, M. R. Radhelan, I. Yasri, and F. Candra, "Design of 28 GHz Microstrip MIMO Antennas for Future 5G Applications," SINERGI, vol. 22, no. 3, pp. 149–154, Oct. 2018. doi: 10.22441/sinergi.2018.3.002.

[62] Y. Rahayu, M. R. Asrul, and T. Rahayu, "Design MIMO 1×8 Antenna for Future 5G Applications," TELKOMNIKA, vol. 16, no. 2, pp. 600–605, Apr. 2018. doi: 10.12928/TELKOMNIKA.v16i2.8383.

[63] P. D. Welch, "The Use of Fast Fourier Transform for the Estimation of Power Spectra: A Method Based on Time Averaging Over Short, Modified Periodograms," IEEE Transactions on Audio and Electroacoustics, vol. AU-15, no. 2, pp. 70–73, Jun. 1967.

[64] F. J. Harris, "On the Use of Windows for Harmonic Analysis with the Discrete Fourier Transform," Proceedings of the IEEE, vol. 66, no. 1, pp. 51–83, Jan. 1978.

[65] Z. Shaterian, A. K. Horestani, and J. Rashed-Mohassel, "Design of slot array antenna in groove gap waveguide technology," IET Microwaves, Antennas & Propagation, vol. 13, no. 8, pp. 1235–1239, 2019. doi: 10.1049/iet-map.2018.5861.

[66] N. A. Wahab, Z. B. Maslan, W. N. W. Muhamad, and N. Hamzah, "Microstrip Rectangular 4×1 Patch Array Antenna at 2.5GHz for WiMax Application," in Proc. Computational Intelligence, Communication Systems and Networks (CICSyN), Liverpool, UK, 2010, pp. 164–168. doi: 10.1109/CICSyN.2010.73.

[67] M. A. Haque et al., "Dual Band Antenna Design and Prediction of Resonance Frequency Using Machine Learning Approaches," Applied Sciences, vol. 12, no. 20, p. 10505, Oct. 2022. doi: 10.3390/app122010505.

[68] G. Xu, H.-L. Peng, Z. Shao, L. Zhou, Y. Zhang, and W.-Y. Yin, "Dual-Band Differential Shifted-Feed Microstrip Grid Array Antenna with Two Parasitic Patches," IEEE Transactions on Antennas and Propagation, vol. 68, no. 3, pp. 2434–2439, Mar. 2020. doi: 10.1109/TAP.2019.2943409.

CURRICULUM VITAE

PERSONAL INFORMATION

Name and Surname: Thura Ali Khalaf Al mohammedawi

EDUCATION

Degree	Graduate College/University	Year
B.Sc.(Internet Engineering)	College of information engineering/Al-Nahrain University	2013
M.Sc.(Information & communication Engineering)	College of information engineering/Al-Nahrain University	2016
Telecommunication Training Course	Korek Telecommunication Company	2012

WORKING EXPERIENCE

Year	Place	Enrollment
2016	Alabshar for Marketing and Media	Programmer, IT Engineer
2017	Earthlink Telecommunication Company	Quality Assurance Auditor Engineer
2018	Al-Shuaa for travel and tourism	software developer and graphic designer
2019	Bee Cable Company	Quality Auditor

PUBLICATIONS

1. T. A. Khalaf and G. Ö. Yetkin, “A 28-GHz High-Gain Slotted Array Antenna with Beam Steering Capability for 5G Millimeter-Wave Applications,” Defence Science Journal, vol. 75, no. 2, pp. 215–223, Mar. 2025, doi: 10.14429/dsj.20405.
2. T. A. Khalaf and G. Ö. Yetkin, “Parasitic Antenna Array with Wide Scanning Coverage for 5G Applications,” in Proc. 17th Int. Conf. on Engineering & Natural Sciences, Prague, Czechia, May 3–7, 2025.
3. T. A. Khalaf and G. Ö. Yetkin, “Design and Analysis of Microstrip Patch Antenna Using Two Feeding Methods for 5G Applications,” in Proc. 17th Int. Conf. on Engineering & Natural Sciences, Prague, Czechia, May 3–7, 2025.

LANGUAGES

Arabic, English.